SEISMIC STUDIES OF THE NORTHERN CASCADIA ACCRETIONARY PRISM: SEDIMENT CONSOLIDATION AND GAS HYDRATES

by
TIANSON YUAN
B.Sc. (Geophysics), Tongji University, China, 1982
M.Sc. (Geophysics), University of Victoria, B.C., Canada, 1990

A DISSERTATION SUBMITTED IN PARTIAL FULFILMENT OF THE REQUIREMENTS FOR THE DEGREE OF

DOCTOR OF PHILOSOPHY
in
the School of Earth and Ocean Sciences

We accept this thesis as conforming
to the required standard

Dr. G. D. Spence, Supervisor (School of Earth & Ocean Sciences)

Dr. M. J. Whiticar, Departmental Member (School of Earth & Ocean Sciences)

Dr. R. D. Hyndman, Member (Pacific Geoscience Centre and School of Earth & Ocean Sciences)

Dr. H. W. Dosso, Outside Member (Department of Physics & Astronomy)

Dr. E. E. Davis, Outside Member (Pacific Geoscience Centre)

Dr. G. F. Moore, External Examiner (University of Hawaii)

Supervisor: Dr. G. D. Spence

ABSTRACT

This thesis work was directed at aspects of two related problems: (1) sediment compaction and fluid expulsion processes in a subduction margin accretionary prism, and (2) the nature and concentration of gas hydrates that form bottom-simulating reflectors (BSRs) observed in the accretionary prism sediments of the northern Cascadia margin. The formation of the gas hydrate and the occurrence of BSRs in the study area are believed to be mainly a consequence of upward fluid expulsion in the accretionary prism. Therefore, the two study objectives are closely correlated. Most of this thesis work was carried out analyzing multichannel seismic data and incorporating available information including downhole and other geophysical measurements. Seismic techniques, such as velocity analysis, forward modelling, and waveform velocity inversion, were used in analyzing the data to advance our understanding of the tectonic and geophysical processes in a dynamic accretionary prism environment.

The velocity structure and the inferred porosity variations across the frontal region of the accretionary prism have been quantitatively assessed by a detailed seismic velocity analysis. Within the Cascadia basin sediments approaching the deformation front, and within the frontal thrust zone of the accretionary prism, seismic velocities increase landward as a result of sediment consolidation. An important conclusion is that more than one third of the pore fluid content of the incoming sediment is lost by the time they are incorporated into the accretionary prism. In the lower slope region of the deformation front, a pronounced velocity

decrease is evident. This low-velocity zone is explained by underconsolidation resulting from rapid horizontal shortening and vertical thickening of the sediment column, accommodated by displacements along thrust faults or by distributed deformation.

A prominent BSR becomes visible immediately landward of the deformation front in the accreted sediment, and is developed over much of the low-to-mid continental slope. The upward pore-fluid migration is believed to play an important role in the formation of a gas hydrate BSR. From the estimated fluid loss of 35% over the 3-km-thick Cascadia Basin sediments with an average sediment porosity of 30%, the quantity of the expelled fluid reaches 315 m^3/m^2 over a distance of 12 km before the basin sediments are incorporated into the accretionary prism. Assuming that 100 mmol/L of methane is removed from the expelled fluid as it moves into the hydrate stability field, a 90-m-thick layer with an average hydrate saturation of 10% of the pore space can be formed by the rising fluids.

A velocity-depth function in the lower slope region, representing a no-hydrate/no-gas reference profile, has been established from the detailed semblance velocity analyses and the ODP log data. The observed and measured sediment velocities near the ODP drill sites increase downward more rapidly than the reference profile above the BSR. Based on the reference profile, the velocity inversion results imply that the velocity increase due to hydrate above the BSR accounts for ~2/3 of the impedance contrast required to produce the BSR reflection amplitudes. The remainder of the impedance contrast appears to come from the velocity decrease associated with small concentrations of free gas below the BSR.

The integrated analysis of the multichannel seismic and ODP downhole velocity data has allowed the velocity enhancement associated with the formation and concentration of gas

hydrate to be estimated. If the BSR is overlain by a 100 m zone of sediment with a mean porosity of 50% in which the hydrate saturation increases linearly from zero at the top of the zone to 20% at the BSR, the estimated hydrate concentration-depth profiles indicate a total hydrate amount of about 5 m^3/m^2 of ocean floor or methane amount of 820 m^3/m^2 at STP. Throughout the Vancouver Island continental margin, where the clear BSR have been observed in an area of 30x200 km, the total methane gas estimated can amount to about 175 Tcf (trillion cubic feet) or 2.6 Gt of carbon.

Examiners:

Dr. G. D. Spence, Supervisor (School of Earth and Ocean Sciences)

Dr. M. J. Whiticar, Department Member (School of Earth and Ocean Sciences)

Dr. R. D. Hyndman, Member (Pacific Geoscience Centre, Geological Survey of Canada, and School of Earth & Ocean Sciences)

Dr. H. W. Dosso, Outside member (Department of Physics and Astronomy)

Dr. E. E. Davis, Outside member (Pacific Geoscience Centre, Geological Survey of Canada)

Dr. G. F. Moore, External Examiner (Dept. of Geology & Geophysics, University of Hawaii)

TABLE OF CONTENTS

LIST OF TABLES

LIST OF FIGURES

ACKNOWLEDGEMENTS

I first want to extend sincere thanks to my supervisors, Dr. Spence and Dr. Hyndman, for their support, guidance, and encouragement throughout the period of this thesis work. Many of their suggestions and comments have kept me on track in exploring a fascinating frontier of the earth sciences at our door steps. Additional thanks are owed to my committee members, Dr. M. Whiticar, Dr. H. Dosso, and Dr. E. Davis, and to my External Examiner, Dr. G. Moore, who provided useful discussions for, and revisions to the thesis.

I also wish to acknowledge the high quality seismic data collected by Digicon Geophysical Corp., and the original data processing by Geophoto Ltd. (Haliburton geophysical Services). Dr. K. Vasudevan and Mr. R. Maier of the Lithoprobe Seismic Processing Facility provided technical assistance in the data re-processing. I wish to thank Dr. M. MacKay for providing me with her VSP data, and Dr. R. Jarrard for his revised ODP logging data. I am especially grateful to Dr. T. Minshull and Dr. S. Singh for their generous assistance in applying their inversion routines, particularly during the period when I worked at Bullard Laboratory at the University of Cambridge. Discussions with Dr. E. Davis and Dr. K. Wang were very much appreciated.

The research was funded by NSERC through Operating Grants URF0043000, OGPIN008, 0GP0156159, 0GP0038327, and Geological Survey of Canada NSERC Grant OGP0038327-88. I am also thankful to Amoco Canada for the scholarship support during my graduate studies.

CHAPTER 1 INTRODUCTION

This thesis work included detailed seismic analyses of regional velocity variations and integrated velocity studies of the gas hydrate bottom-simulating reflector (BSR) velocity structure on the northern Cascadia accretionary prism off Vancouver Island. Much of the thesis work has been presented in scientific journal and Ocean Drilling Program (ODP) report [*Hyndman et al.*, 1993; *Hyndman et al.*, 1994; *Yuan et al.*, 1994; *Yuan et al.*, 1996]. As an introduction to the study area, one of the most extensively studied subduction zones in the world, and the study objectives, a brief summary of geological and geophysical investigations, regional plate tectonic setting, and previous studies on the subjects of fluid expulsion and gas hydrates on the Vancouver Island margin is presented below.

1.1 Summary of Geological and Geophysical Investigations in the Region of Northern Cascadia Subduction Margin off Vancouver Island

The tectonic history and structure of the northern Cascadia subduction margin off Vancouver Island (Figure 1.1), where the oceanic Juan de Fuca plate subducts beneath the continental North America plate, have been extensively investigated by a wide range of geophysical measurements and geological work. In the late 1960s, exploration was initiated by Shell Canada Ltd. in Tofino Basin on the continental margin. A regional seismic survey and a program of seven wells were carried out exploring the hydrocarbon potential of the basin [*Shouldice*, 1971]. In 1980 the Vancouver Island Seismic Project, which consisted of

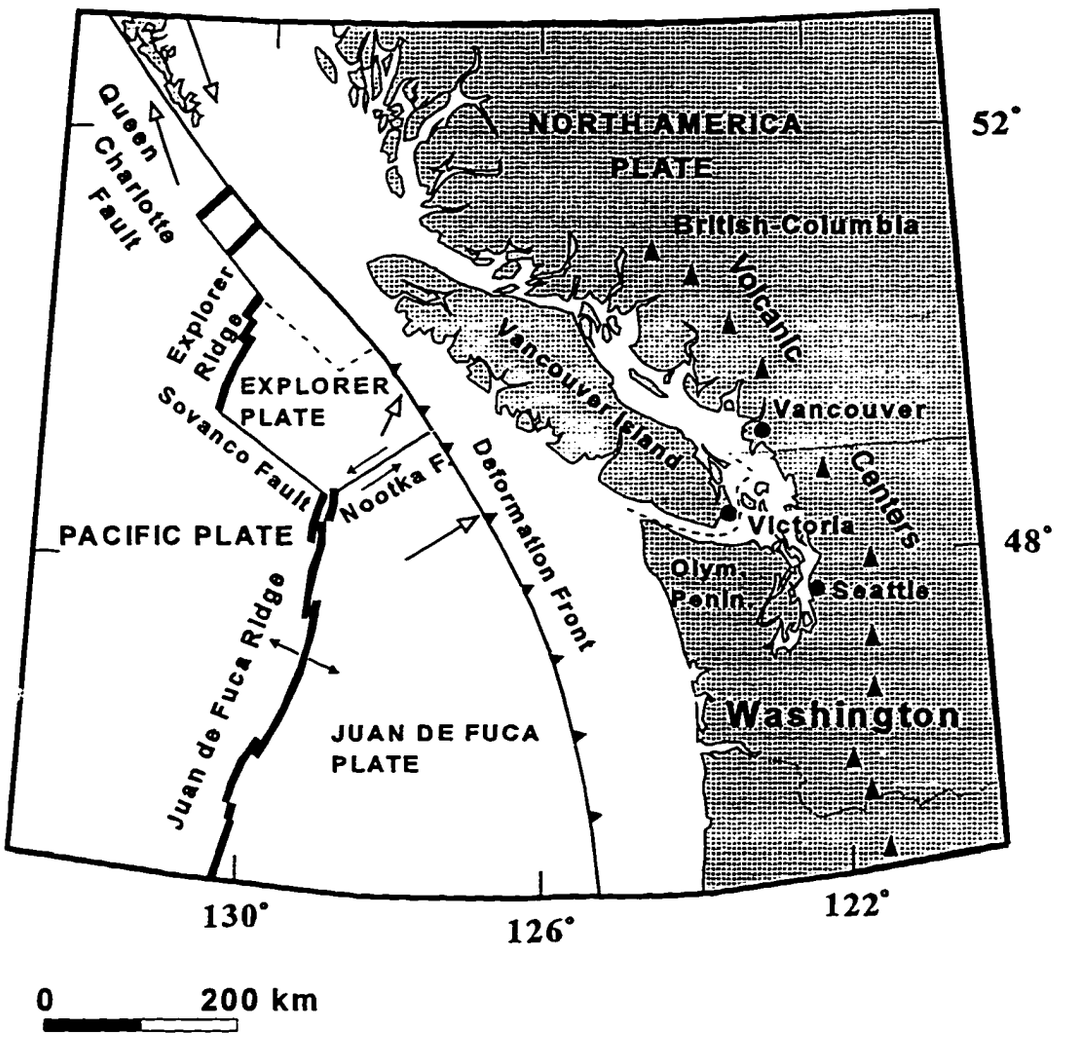

Figure 1.1 The continental margin in the vicinity of the northern Cascadia subduction zone, showing the plate-tectonic regime and major tectonic elements. The spreading ridge segments are shown with heavy lines, and the boundary between the oceanic plates and the continental plate is shown with fault line.

a 350-km onshore-offshore refraction profile perpendicular to the continental margin, was recorded by the Consortium for Crustal Reconnaissance Using Seismic Techniques (COCRUST) [*Ellis et al.*, 1983]. The major objective of the project was to obtain a seismic structure section to upper mantle depths from the oceanic Juan de Fuca plate to the inland volcanic arc [*Waldron*, 1982; *Spence et al.*, 1985; *Waldron et al.*, 1990]. In 1984, phase I of the Canadian Lithoprobe multidisciplinary geoscience program brought detailed geophysical and geological studies to south-central Vancouver Island, with high-quality land multichannel seismic reflection lines forming the primary data set [*Yorath et al.*, 1985a, 1985b; *Sutherland Brown and Yorath*, 1985; *Rogers*, 1985; *Green et al.*, 1986; *Kurtz et al.*, 1986; *Clowes et al.*, 1987a; 1987b; *Yorath et al.*, 1987; *Hyndman*, 1988; *Lewis et al.*, 1988]. In 1985, these results were supplemented by widely spaced marine multichannel seismic lines [*Yorath et al.*, 1987] and a number of additional studies across the continental shelf and slope of northern Cascadia continental margin that were part of the Frontier Geoscience Program of the Geological Survey of Canada [e.g. *Davis and Hyndman*, 1989; *Davis et al.*, 1990]. *Hyndman et al.* [1990] presented a summary of the regional offshore-onshore geophysical work, which included multichannel seismic reflection, shallow single-channel seismic profiling, gravity and magnetic surveys, plus geothermal, seismicity and magnetotelluric measurements.

Most recently, as part of site surveys for the international Ocean Drilling Program (ODP), new marine multichannel seismic reflection lines were acquired in 1989 across the northern Cascadia convergent margin and adjacent Juan de Fuca Ridge [*Spence et al.*, 1991a; 1991b]. Some of the reflection lines were also recorded at land sites to obtain important deep velocity information [*Wang and Clowes*, 1995]. Of particular interest to the survey were the

detailed three-dimensional geometry of the accretionary wedge and the accreted terranes, the variations in thrust and fold structures at the deformation front, and the characteristics of the gas hydrate BSR.

In the fall of 1992, ODP Leg 146 penetrated accretionary prism sediments and investigated the relationship between fluid expulsion and tectonics in the development of the subduction zone accretionary prism, the first ODP drilling directed primarily at the nature of the widely distributed BSR associated with the base of a zone permeated by methane hydrate [*Westbrook et al.*, 1994; *Carson et al.*, 1995]. At all drill sites off the Vancouver Island and Oregon margins, detailed measurements were made of core and in situ physical and chemical conditions to relate fluid chemistry, the composition and state of deformation of the sediments, and measured or inferred rates of fluid flow and methane content. Downhole sonic logging and vertical seismic profile (VSP) measurements were made to provide formation velocity information. Subsequent to the ODP drilling, a seismic program was conducted in the vicinity of ODP Leg 146 Hole 889 with a collection of wide-angle ocean bottom seismometer (OBS) data and fine-grided single-channel seismic reflection data which provided detailed aerial distribution information on the hydrate BSR [*Spence et al.*, 1995]. A two-ship Expanding Spread Profile (ESP) survey near the ODP drillsites was carried out in 1993 by the Defence Research Establishment Pacific (DREP) to examine seafloor reflection characters and to constrain the seismic velocity structure of the hydrate zone [*Hannay*, 1995].

The unusual wealth of geophysical and geological information obtained in the northern Cascadia margin has therefore made the region one of the most extensively studied subduction zones in the world [e.g., *Hyndman et al.*, 1994; *Hyndman*, 1995], and a laboratory

to study the effects of fluid flow and the nature of gas hydrate in an accretionary environment. Over the past 20 years or so, the knowledge of the regional tectonic processes on the northern Cascadia margin has evolved from recognition of subducting oceanic plate to a more thorough understanding of geophysical and geological phenomena from the near surface to the deep crust and mantle.

1.2 Regional Plate Tectonic Setting of the Northern Cascadia Subduction Margin

The modern plate-tectonic regime of the Cascadia margin is dominated by the motions of three main lithospheric plates: the large Pacific and North America plates and the intervening Juan de Fuca plate system. The northern Cascadia subduction zone lies along the right-lateral transform boundary between the oceanic Pacific and continental North America plates. In the north along the margin of Vancouver Island (Figure 1.1), the small and recently isolated Explorer plate moves at very low rates in a hot-spot reference frame or simply is being overridden by North America plate at rates of 10-25 mm a^{-1} [*Hyndman et al.*, 1979; *Davis and Riddihough*, 1982; *Riddihough*, 1984]. It may be breaking up with recent convergence slowing or stopping [*Rohr and Furlong*, 1995]. South of the Nootka transform plate boundary, subduction of the Juan de Fuca Plate takes place in a direction approximately orthogonal to the southern Vancouver Island margin at a rate of about 45 mm a^{-1} [*Riddihough*, 1984]. The difference in convergence rate between the Explorer and Juan de Fuca plates is being taken up along the Nootka Fault zone [*Hyndman et al.*, 1979; *Davis and Hyndman*, 1989]. Constrained by offshore magnetic anomalies [*Riddihough*, 1985], the ages

of the oceanic plate are young in the vicinity of the Nootka fault, ~ 5 M, and increase to the southeast along the margin. Off southern Vancouver Island in the main study area, the age of the oceanic crust at the deformation front is about 6 m.y. [*Riddihough*, 1984]. In the northern Cascadia subduction zone, the young and buoyant Juan de Fuca oceanic plate combined with the advance of the overriding North America plate at a rate of about 22 mm a^{-1} [*Riddihough*, 1984] provides conditions for efficient sediment off-scraping at or near the top of oceanic crust. The shallow subduction angles of 3-4° just seaward of the deformation front [*Hyndman et al.*, 1994; *Hyndman*, 1995] and complete offscraping, combined with the abundant terrigenous sediment supply, have caused a large accretionary prism about 60 km in width to develop along the Cascadia margin offshore Vancouver Island in the past 43 Ma [*Davis and Hyndman*, 1989; *Hyndman et al.*, 1990].

1.3 Structure of the Continental Shelf and Terrane Accretion

Most of Vancouver Island is underlain by Wrangellia (Figure 1.2), an allochthonous terrane which outcrops as Palaeozoic and Mesozoic submarine complexes [*Coney et al.*, 1980; *Gabrielse and Yorath*, 1991; *Yorath*, 1995]. No pre-Tertiary rocks are preserved in place along the northern Cascadia margin. It is postulated that any sediments accumulated on the margin of Wrangellia have been transformed northward by Late Cretaceous transform-fault motion [e.g., *Johnson*, 1984; *Wells et al.*, 1984; *Massey*, 1986]. Two small terranes, the Mesozoic mainly sedimentary Pacific Rim Terrane and the Eocene volcanic Crescent Terrane, were emplaced against and beneath Wrangellia after the initiation of subduction in the Early Eocene. The Crescent Terrane may be a sliver of marginal basin or oceanic crust

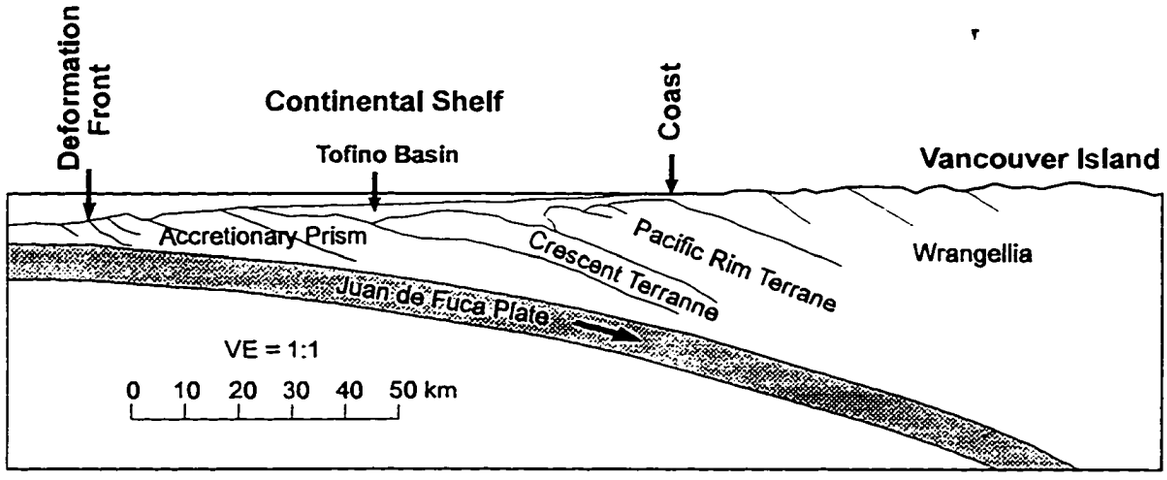

Figure 1.2 Summary of cross section for the northern Cascadia continental margin off Vancouver Island (after *Hyndman et al.* [1990]).

that first underthrust the continent and in turn was underthrust by the Juan de Fuca plate [*Hyndman et al.*, 1990; *Spence et al.*, 1991a, 1991b]. The Tofino forearc basin, containing up to 4 km of Eocene to Holocene sediments, overlies the accretionary prism and the two accreted terranes beneath the continental shelf.

The modern accretionary prism has formed by scraping off the incoming sediments on the subducting Juan de Fuca plate [*Davis and Hyndman*, 1989]. The accretionary prism is bounded at its base by the oceanic plate and on its landward side by the landward-dipping Crescent Terrane [*Hyndman et al.*, 1990]. As the plate convergence rate since the Late Eocene remained nearly constant, estimates of the accretionary prism sediment budget can be made [*Davis and Hyndman*, 1989; *Hyndman et al.*, 1990]. The mass balance calculation indicated that the volume of the accretionary prism sediments is approximately equal to the

estimated volume of sediments brought in on the Juan de Fuca plate. This is also consistent with the observation that the basal decollement landward of the deformation front appears to lie at or near the sediment-crust boundary and that much if not most of the incoming sediments have been accreted to the margin rather than subducted [*Spence et al.*, 1991a; 1991b].

The cross-sectional geometry of the northern Cascadia accretionary prism is well defined from beneath Cascadia Basin to a depth of 40 km beneath Vancouver Island by seismic reflection lines and other geophysical data [e.g., *Hyndman et al.*, 1990]. The dip of the oceanic crust increases continuously from 3° to 4° in Cascadia Basin to 10° under the edge of the continental shelf (Figure 1.2). Based on a model for critically tapered accretionary prism developed by *Davis et al.* [1983], sediment mechanical properties, such as pore pressure, can be inferred from the average geometry of the wedge. Applying the critical taper theory, *Davis and Hyndman* [1989] concluded that there is little doubt that the observed accretionary prism geometry, particularly of the lower continental slope, requires elevated pore pressure, close to lithostatic, in the wedge sediments.

1.4 Previous Studies of Fluid Expulsion and Sediment Consolidation in Accretionary Prism Sediments and Gas Hydrates in Saturated Porous Sediments

Numerous studies have addressed the relationship between fluid flow and tectonics in accretionary prisms at plate boundaries. In the past ten years or so, there has also been a resurgence of interest in investigating methane gas hydrate in marine sediments and associated

BSRs widely observed on seismic records. As these two are the main subjects of this study, a brief introduction and some controversial findings are presented below.

1.4.1 Studies of Fluid Expulsion and Sediment Consolidation

Sediments entering subduction zones have high porosities, up to 70% at the seafloor in some cases. Stacking of thrust packages of the sediment sequences within the accretionary prism results in rapid compaction and partial expulsion of the interstitial water. Because of the low permeabilities of the sediments and rocks where the fluids are released, a very high fluid pressure and consequently a very low effective grain-to-grain contact pressure confining the sediment grain matrix tend to prevail. Deformation structural features are affected at all scales by fluid flow and fluid pressure as the energy necessary for motion to occur along decollements and thrusts as well as bulk grain-to-grain deformation are greatly reduced. Fluid flow from accretionary prisms causes geothermal and geochemical effects, precipitates and dissolves minerals, and feeds the surface biological communities. The fluid flow in accretionary prisms thus has important tectonic implications.

A primary constraint on and a direct measurement of pore fluid expulsion associated with sediment accretion is derived from landward change in porosity-depth relationship inferred from velocity data, assuming that velocities are primarily controlled by porosities [e.g., *Bray and Karig*, 1985; *Bangs et al.*, 1990; *Westbrook*, 1991; *Moore and Vrolijk*, 1992; *Yuan et al.*, 1994]. In many accretionary wedges it has been documented that, in addition to vertical loading, the horizontal tectonic stress consolidates sediment sections, expelling pore fluids and resulting in an increased seismic velocity [*Fowler et al.*, 1985; *Moore et al.*, 1988;

Minshull and White, 1989; *Moore and Vrolijk*, 1992]. Horizontal tectonic stresses in accretionary wedges are often observed to reduce sediment porosities to values less than those produced in normal consolidation from the load of thickening overburden, i.e., they cause overconsolidation [*Bray and Karig*, 1985]. However, in areas where the matrix permeability is low or the sediment thickening rate is high, pore fluid expulsion and sediment consolidation are inhibited when sediments are moved to greater depths [*Bangs et al.*, 1990; *Lewis*, 1990]. The thickening sediment section then becomes underconsolidated and overpressured [*von Huene and Lee*, 1982; *Shi and Wang*, 1988]. Thus, there exist the opposing processes of sediment overcompaction due to horizontal tectonic stresses and sediment undercompaction due to tectonic thickening.

Davis et al. [1990] used heat-flow data to constrain the nature of pore fluid expulsion from the northern Cascadia accretionary prism. The lack of strong local thermal anomalies in the area of the deformation front suggested that only minor amounts of fluid flow were moving up along faults and other hydrologic channels. Most of the pore fluid from the consolidating accretionary prism must be expelled pervasively.

Hyndman et al. [1993a] and *Wang et al.* [1993] used the depth to the thermally controlled methane hydrate BSR to study the thermal effects of the sediment thickening and fluid expulsion in the northern Cascadia accretionary prism. The numerical thermal models constrained by porosities determined from the seismic velocity data require that high pore pressure and sediment underconsolidation exist in the rapidly thickening zone of the prism.

1.4.2 Studies of Bottom-Simulating Reflector Associated with Gas Hydrates

Bottom-simulating reflectors (BSRs), associated with the base of the hydrate stability field [e.g., *Kvenvolden and McDonald*, 1985], are observed in the upper few hundred meters of ocean floor sediments on many continental margins. BSRs are common in subduction zone accretionary prisms. They are especially apparent where sediment stratigraphy is not parallel to the seafloor.

Hydrates are solid ice-like substances consisting of water molecule cages stabilized by enclosed gas molecules [e.g., *Sloan*, 1990]. The interest in submarine gas hydrate has resulted from the realization that they may represent a major energy resource [e.g., *Kvenvolden*, 1988a], and that they could play an important role in global climate change [e.g., *Kvenvolden*, 1988b; *Nisbet*, 1990; *Kvenvolden*, 1993]. Unfortunately, in situ information from deep-sea drilling is very limited; much of the available information as to the origin of BSRs has come from seismic reflection data [e.g., *Shipley and Didyk*, 1981; *Minshull and White*, 1989; *Miller et al.*, 1991; *Hyndman and Davis*, 1992; *Hyndman and Spence*, 1992; *Yuan et al.*, 1996]. Numerous studies involving forward modelling and inversion of seismic reflection data have been carried out [*Miller et al.*, 1991; *Hyndman and Spence*, 1992; *Singh et al.*, 1993; *Minshull et al.*, 1994; *Katzman et al.*, 1994; *Wood et al.*, 1994; *Singh and Minshull*, 1994; *Andreassen et al.*, 1995; *Korenaga et al.*, 1996]. These studies used BSR reflection coefficients, reflection waveform modelling, and amplitude-versus-offset (AVO) characteristics to constrain seismic velocity variations above the BSR and the presence of low velocities associated with free gas in the sediment pore space beneath it.

In the area of the Ocean Drilling Program (ODP) Sites 889/890 on the lower slope of the Cascadia margin off Vancouver Island (Figure 2.1), *Hyndman and Spence* [1992]

concluded that a high-velocity layer existed above the BSR, having a sharp base and a transitional top, as determined from high-resolution velocity analysis, synthetic seismogram modelling, and AVO studies. They also concluded that about 30% of the pore spaces were required to be filled with hydrate if the BSR impedance contrast was the sole result of high-velocity sediments containing hydrate over water-saturated sediments. No velocity or AVO effects of free gas below the BSR could be detected. A thin layer containing gas was allowed by the data, provided that (1) it had a transitional base such as not to give a reflection from the bottom of the gas layer and (2) the concentrations of gas were sufficiently low (less than a few percent) such as not to strongly affect Poisson's ratio and thus AVO. Subsequent downhole logging and VSP data at ODP Sites 889 and 892 showed that there were low velocities immediately below the BSR that implied the presence of free gas [*MacKay et al.*, 1994]. *MacKay et al.* [1994] also suggested that there was only a very small velocity enhancement from the presence of hydrate above the BSR and that the BSR is generated primarily from the top of the free gas layer. *Singh and Minshull* [1994] came to a similar conclusion of a low-velocity gas layer beneath the BSR and little velocity enhancement above it, based on a full waveform inversion of the multichannel data of *Hyndman and Spence* [1992]. Seismic velocities in hydrate-bearing sediments overlying the BSR should be much higher than in hydrate-free sediments [e.g., *Whalley*, 1980; *Pearson et al.*, 1986; *Sloan*, 1990]. If there is free gas beneath the BSR, a sharp reduction in compressional velocity will result. It should be noted, however, that in previous velocity determinations, there has been little direct constraint on the normal no-hydrate/no-gas velocity-depth profile and thus little constraint on whether the BSR contrast is from high velocity over normal velocity or normal

velocity over low velocity. A reference sediment velocity-depth profile unaffected by either high-velocity hydrate or low-velocity free gas is thus important in establishing velocity structure of the BSR and estimating methane hydrate concentration.

CHAPTER 2 SEISMIC VELOCITY STUDIES OF THE ACCRETIONARY PRISM

Large offset multichannel seismic reflection data from the subduction zone margin off Vancouver Island define the geometry, internal structure and deformation style of the northern Cascadia accretionary prism. A very detailed seismic velocity analysis has been performed to quantitatively assess the velocity structure and thus to infer porosity variations and pore fluid expulsion across the deformation front from within the sediments of Cascadia basin to the accreted sediments of the lower slope region. Results of the detailed velocity analysis have been summarized in *Hyndman et al.* [1994] and *Yuan et al.* [1994].

2.1 Multichannel Reflection Data

As part of the site surveys of the international Ocean Drilling Program along the northern Cascadia convergent margin, seismic reflection data were collected in 1989 offshore Vancouver Island (Figure 2.1), to define the geometry, internal structure and deformation style of the accretionary wedge. The air gun source for the 1989 acquisition was a tuned array with a total volume of 125 L (7820 $inch^3$). A 144-channel streamer recorded 36-fold data to a maximum offset of 3760 m. Description of the seismic data set and its interpretation has been presented by *Spence et al.* [1991a, 1991b].

The new and previous multichannel seismic lines provide clear definition of the Cascadia Basin sediment section entering the subduction zone. Overlying the oceanic crust,

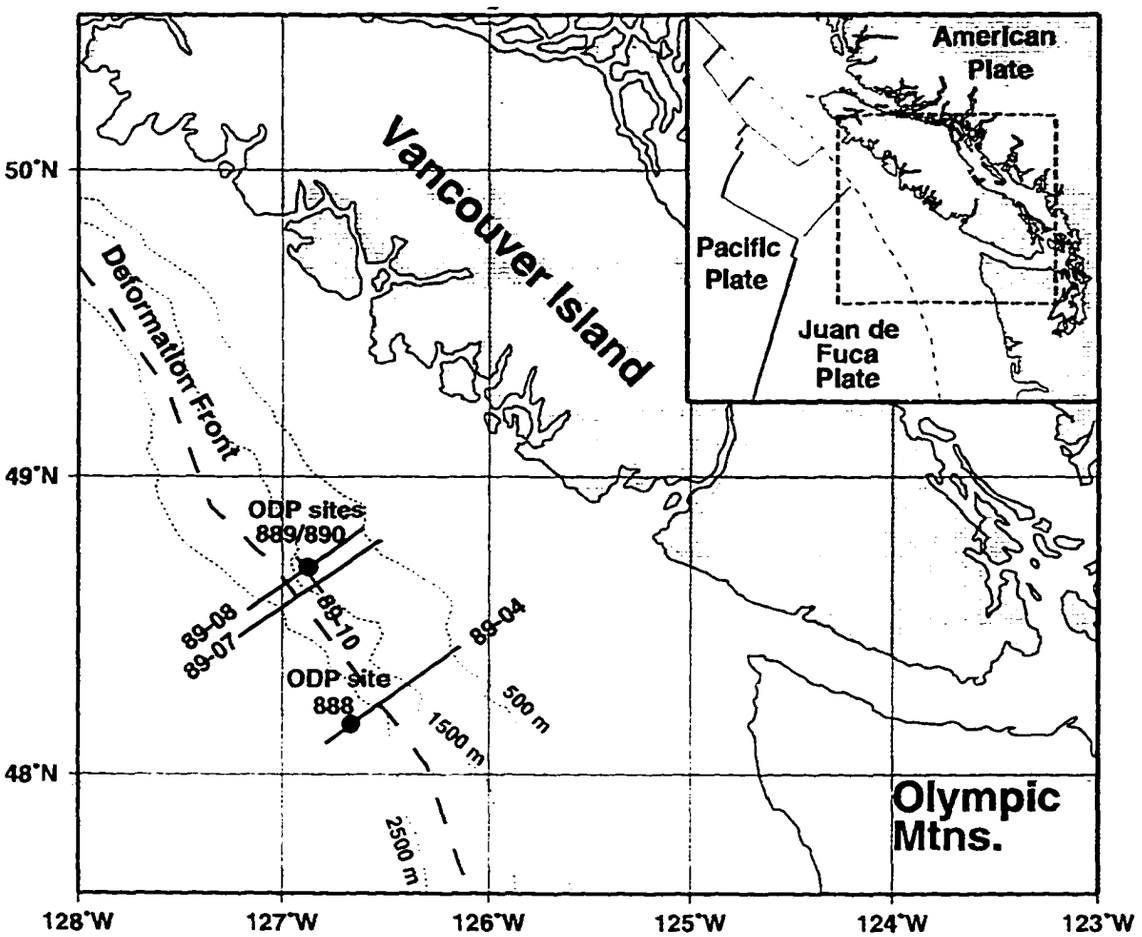

Figure 2.1 Locations of the 1989 Cascadia margin reflection lines analyzed in this study. The 500-m bathymetry lines of the study area and ODP sites 888 and 889/890 drilled in 1992 are also shown.

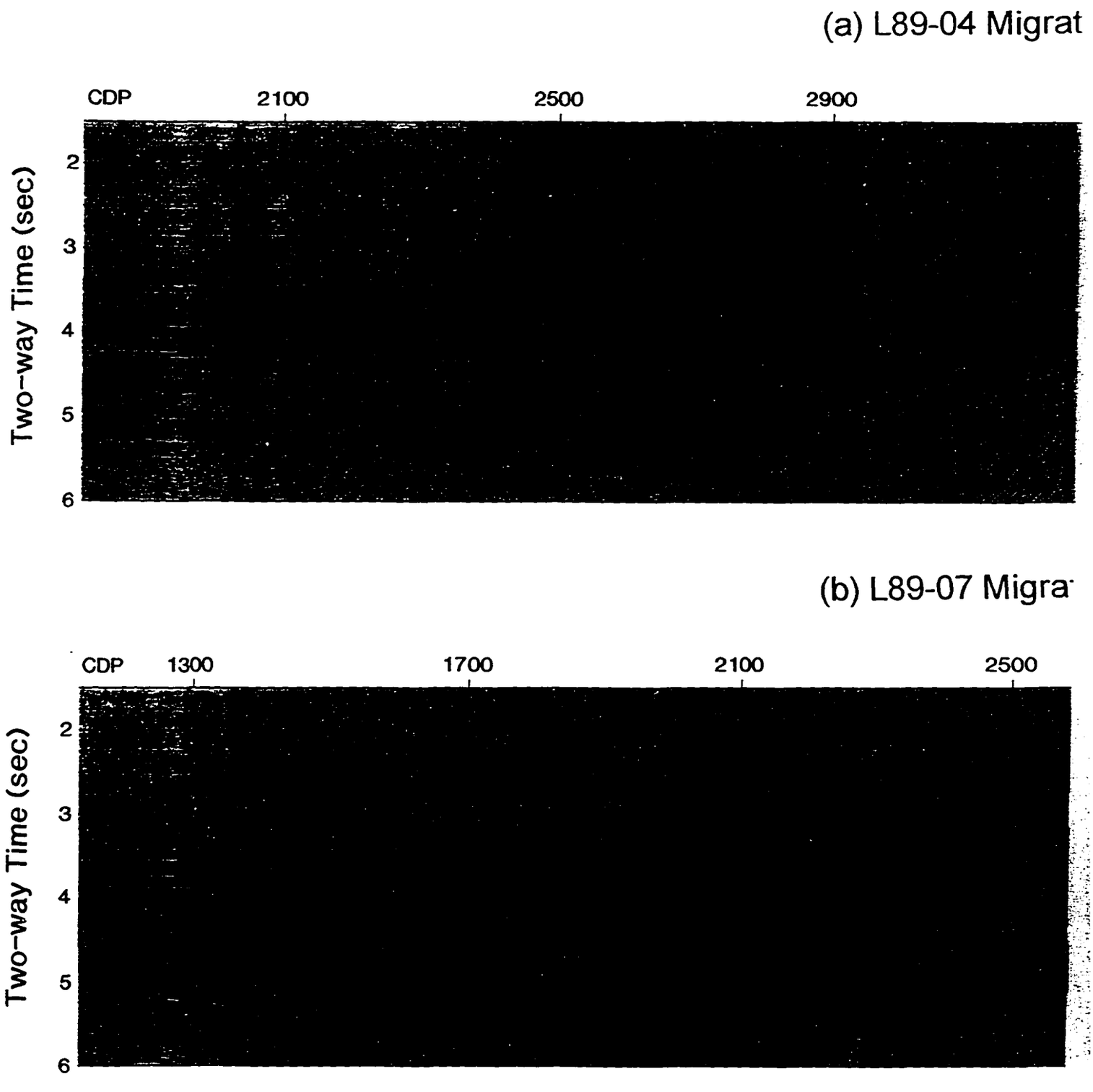

Figure 2.2 Migrated multichannel seismic sections of (a) L89-04, and (b) L89-07 characte

) L89-04 Migration

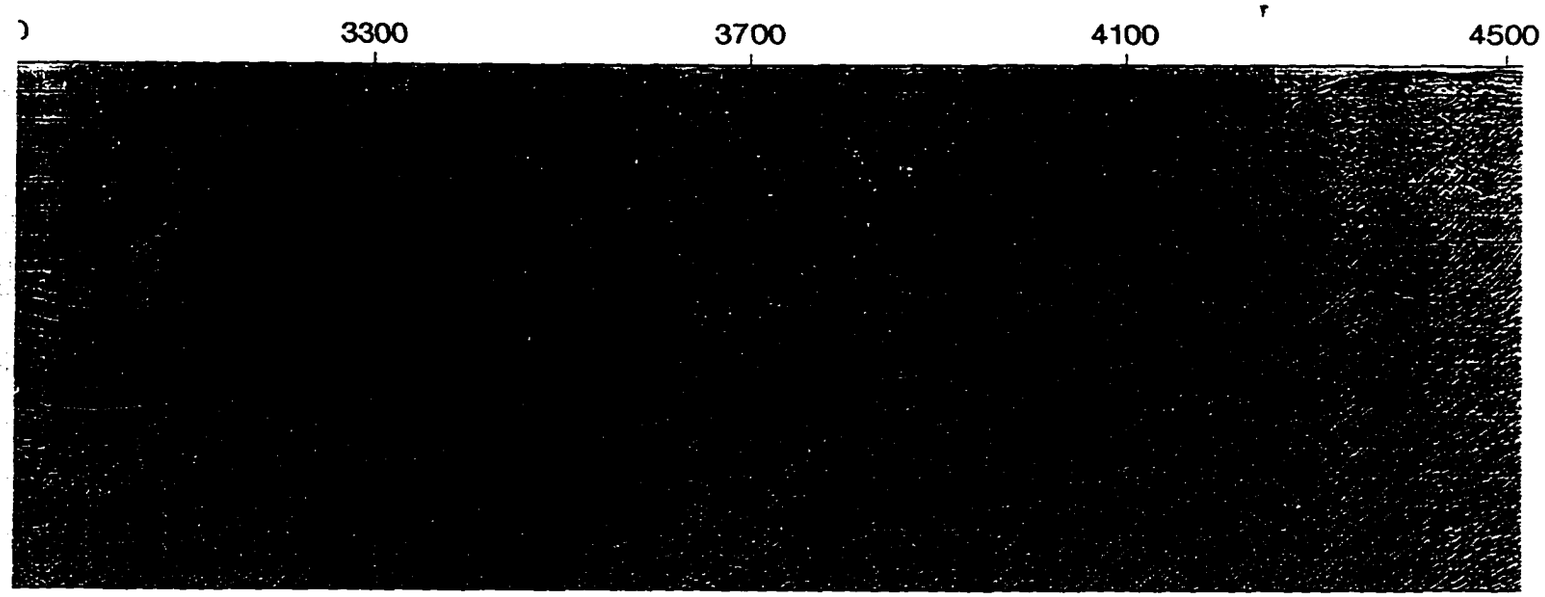

) L89-07 Migration

5 km

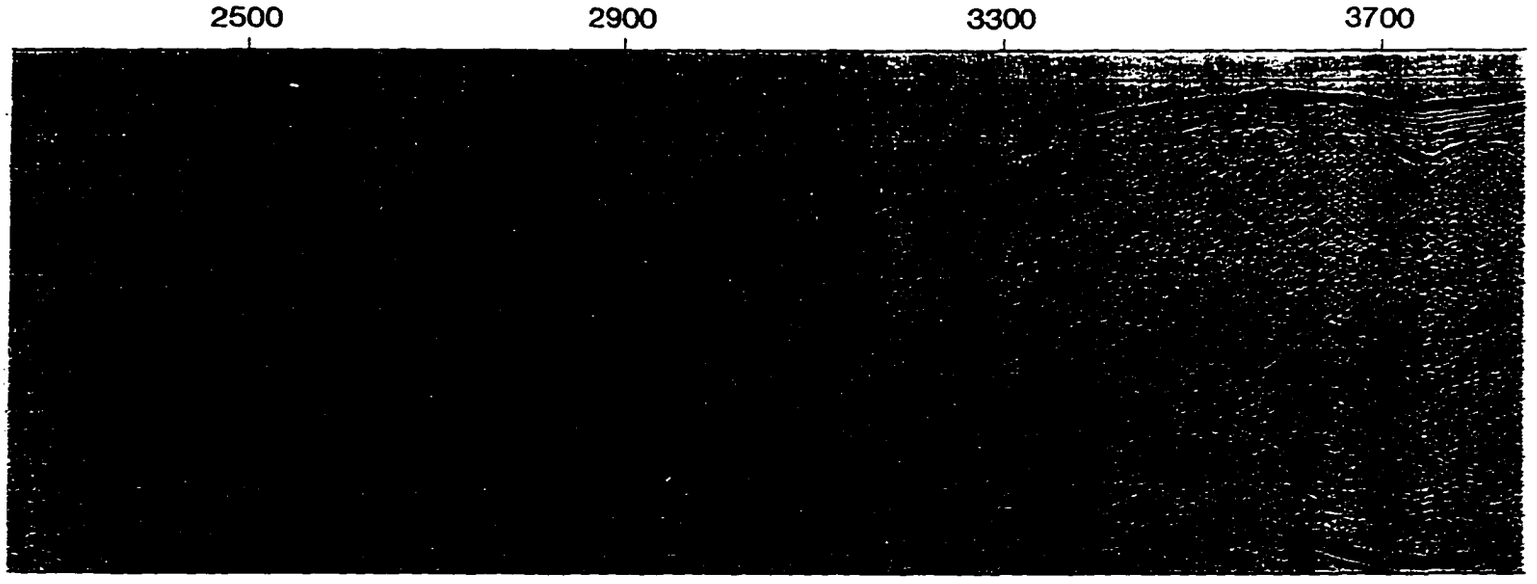

, and (b) L89-07 characterizing two different deformation styles, thrusting and folding of the sediment section.

the sediment sequence consists of 2.0 to 2.5 km of rapidly deposited probably Pleistocene turbidites that are very seismically reflective, overlying 0.3 to 1.2 km of fine-grained pre-Pleistocene hemipelagic deposits. Almost all of the sediments are scraped off the subducting oceanic plate and accreted to the margin. At the frontal region of the wedge, margin-parallel thrust faults and folds are developed. On seismic line L89-04 (Figure 2.2a) at the deformation front, a series of three major landward-dipping thrust faults and associated anticlinal ridges occurs at a spacing of ~5 km. These faults penetrate close to the top of the igneous oceanic crust, probably within 200-300 ms; thus little sediment is currently available for underplating at greater depths or subduction beneath the margin [*Hyndman et al.*, 1990; *Spence et al*, 1991a, 1991b]. The vertical offsets along the faults vary but can be as much as 500 m, and the fault plane reflections have a reverse-polarity character almost everywhere. Figure 2.3 clearly shows the reverse polarity of the seawardmost fault plane reflection. The fault cutting the seafloor near SP 560 (Figure 2.2a and 2.6a) is well developed; it over-thrusts the hanging-wall section ~800 m above the foot-wall resulting in a sediment slump seaward of the fault. Within the

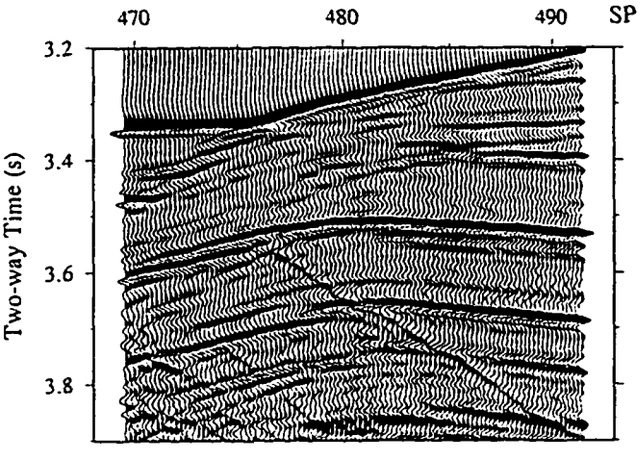

Figure 2.3 A close-up section of the seawardmost thrust fault near SP 470 on L89-04. The fault plane reflections show reversed polarity as compared with the seafloor reflections, which may indicate reduced velocities due to high-pressure fluid flow within the fault zone.

landwardmost fault block, proto-thrusts in the turbidite section can be seen with visible reflector offsets between SP 640 and 690 (Fig. 2.5a and 2.6a).

A different deformation style is observed on L89-07 (Figure 2.2b). At the toe of the wedge an anticlinal ridge rises over 750 m above the abyssal ocean floor, marking the deformation front. The initial deformation is accomplished mainly by folding, but there is evidence for a thrust fault ramp beneath the fold. Landward of this frontal ridge, there is a zone where sediments are less deformed and hence coherent reflectors associated with the Cascadia Basin depositional bedding is still preserved. Farther landward on both lines where the sediment section grows rapidly in thickness, tectonic thickening is associated with incoherent distributed deformation and the seismic stratigraphy is generally lost. A low taper angle is maintained on the lower-to-middle slope which is indicative of relatively weak wedge material or elevated pore pressures within and near the base of the wedge [*Davis and Hyndman*, 1989].

2.2 Velocity Analysis of the Basin and Wedge Sediments

2.2.1 Procedure of the Velocity Analysis

The new multichannel data collected on Vancouver Island margin are of excellent quality, and with maximum offset up to 3760 m they provide sufficient moveout over common-depth-point (CDP) gathers for accurate velocity analysis. As a consequence of the young age (5-7 Ma) of the incoming oceanic crust and the thick sediment section, water depths in the area are relatively shallow, ~1200 m on the lower continental slope region and ~2500 m on the Cascadia abyssal basin, about half of that for most other accretionary wedge

complexes. In addition, vertical resolution of the velocity is enhanced by the abundance of strong, laterally continuous reflectors. These favourable conditions made it possible to carry out a very detailed and systematic investigation of seismic velocity variations across the sediment accretion zone based on conventional semblance velocity analysis.

Full-fold CDP gathers were used to determine velocity-depth functions at a close separation of 125-250 m on the two profiles, L89-04 and L89-07 (Figures 2.5a and 2.7a). Margin parallel line L89-10 (Figure 3.4b) was also examined to acquire accurate velocities with negligible dipping effects at a fixed landward distance on the lower slope region. Dip moveout processing (DMO) in the f-k domain was applied on common-offset-gathers prior to the semblance velocity calculation [*Hale*, 1984; *Liner*, 1990]. Systematic velocity errors caused by reflection dips, especially in regions where there are conflicting dips between stratigraphic interfaces and more steeply dipping fault plane interfaces, are thus reduced. Following semblance analysis, interactive adjustments of moveout velocities were performed to flatten accurately individual reflection events on CDP gathers, and to obtain the final RMS velocities. Interval velocities of the sediment section were then calculated using the Dix equation [1955].

2.2.2 Estimate of Velocity Errors

The hyperbolic traveltime calculation generally used in the semblance velocity analysis is only an approximation in a multilayer sub-surface model. *Al-Chalabi* [1974] and *Stoffa* [1982] evaluated the deviation of the true traveltime curve from the best hyperbolas with increasing offset in velocity determination from wide aperture data. The effects are velocity

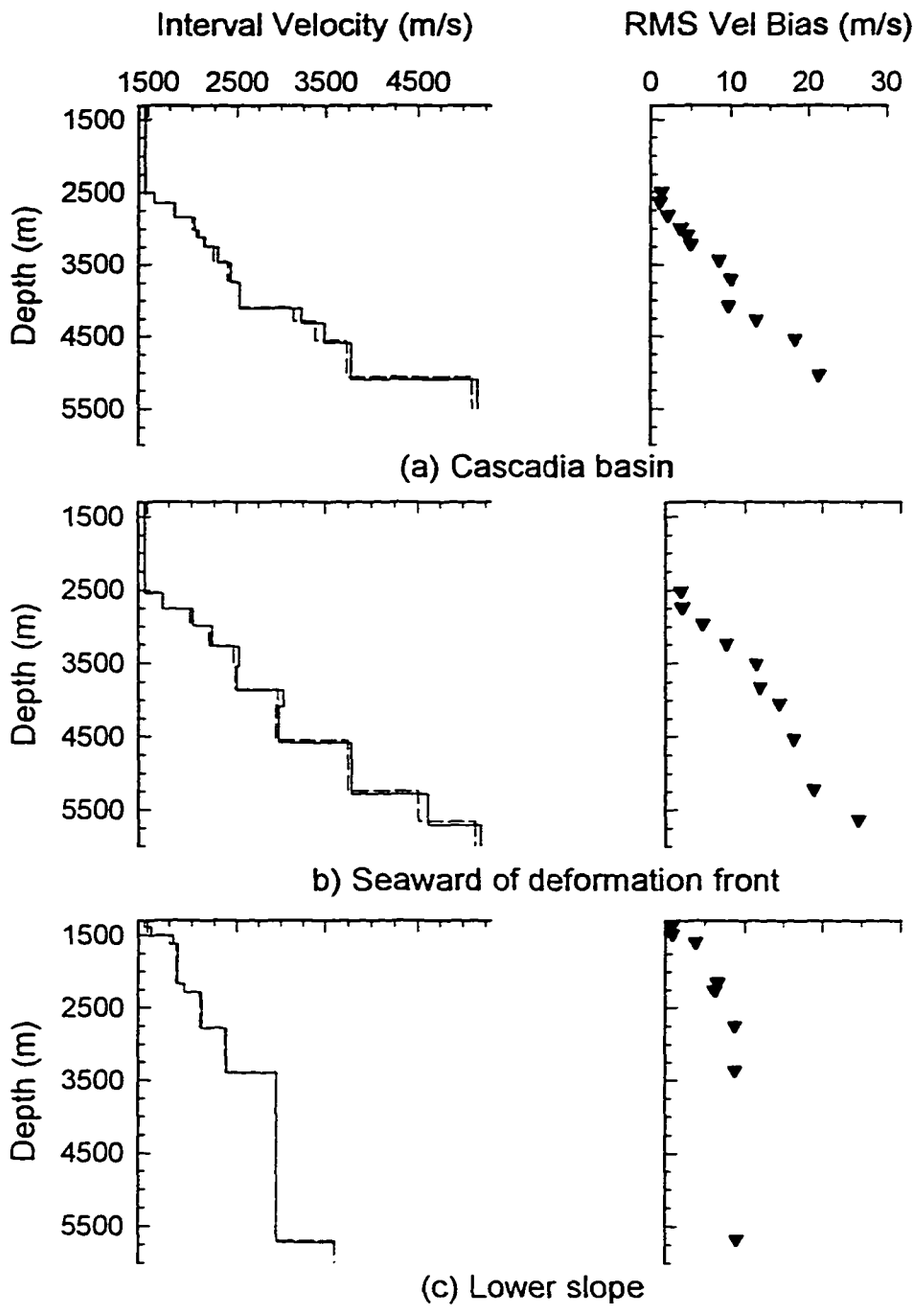

Figure 2.4 Examples of interval velocity models for ray tracing are shown as solid lines, and interval velocities from the two-term hyperbolic approximation are plotted with dashed lines. Differences between model RMS velocities and stacking velocities obtained from least squares fit through traveltimes at each interface are marked by triangles on the right. (a) Cascadia Basin 6.5 km seaward of the deformation front; (b) 2 km seaward of the deformation front in the high velocity zone; and (c) on the lower slope region 16 km landward of the deformation front in the low velocity zone.

structure and acquisition geometry dependent, and can be assessed by comparing an exact model RMS velocity-depth function with the velocity function obtained from a least-squares-fit of a T^2-X^2 plot in which traveltimes are given by raytrace modelling. This consideration is illustrated in Figure 2.4, where the ray-tracing velocity models are based on the semblance velocity results along L89-07. The velocity deviation from the exact model value increases with depth, reaching a maximum of 30 m/s. That this deviation is small is believed largely due to the modest increase in sediment velocity with depth, and an optimized combination of spread length and water depth. Since the systematic errors in stacking velocities increase monotonously with depth, the interval velocity of each layer is not affected significantly because of the cancellation of velocity increases at the top and bottom of each layer. This systematic error in semblance analysis is small compared to random errors and may be neglected.

The precision associated with measurement of RMS velocity in the presence of random noise is related to the relative error of stacking velocity, the depth to the target of interest, the fold of coverage and the moveout at maximum offset [*Al-Chalabi,* 1974]. *Hajnal and Sereda* [1981] provided a simple form to evaluate interval velocity errors,

$$\Delta V_{I,n} = \frac{2T_{n-1}}{T_n - T_{n-1}} \Delta V_{RMS,n-1}, \qquad (2.1)$$

where ΔV_I and ΔV_{RMS} are interval and RMS velocity errors, and T_{n-1} and T_n are two-way traveltimes to the top and bottom of the layer where interval velocity is evaluated. Since the velocity error in the water column is insignificant, the traveltime in the above equation is measured from the seafloor. At a sub-bottom depth of 1 s and with a depth interval of 0.2

s, an RMS velocity error of 20 m/s causes an interval velocity error of ±10%. The estimated interval velocity error does not increase significantly with depth, since thicker layers are generally used at greater depths. Largely due to the relatively shallow water depths and large offset coverage, the interval velocity errors are thus estimated to be less than ±10% (also see Figures 2.6b and 2.8). The random errors are further reduced by the smoothing in the velocity contouring process to an estimated ±5% over most of the profiles. The velocity errors are larger in areas where there is poor reflector coherence, such as in the slope region, but the accuracy of the interval velocity calculation may not deteriorate since layer thicknesses have been increased in these areas.

2.2.3 Seismic Velocity Structure on L89-04

Two main processes affect the landward variation of seismic velocities; (1) horizontal compaction without thickening which increases the sediment velocities, and (2) landward tectonic thickening which displaces sediment elements to greater depths and alters the porosity versus depth profile. The first process is best illustrated in the thrust fault zone of L89-04 (Figure 2.2a), and the second on the lower slope region of L89-07 (Figure 2.2b).

The velocity results of the thrust zone on L89-04 are shown in Figures 2.5b, 2.5c, and 2.12. Interval velocities are plotted in time for ease of comparison with the migrated section, and in depth for evaluating velocity variations relative to overburden thickness. As the deformation front is approached from the seaward side (within 10-12 km), the velocities within the basin strata increase rapidly. Farther landward in the region of the frontal thrusts, velocities follow a similar progressive landward increase within each fault block. In contrast

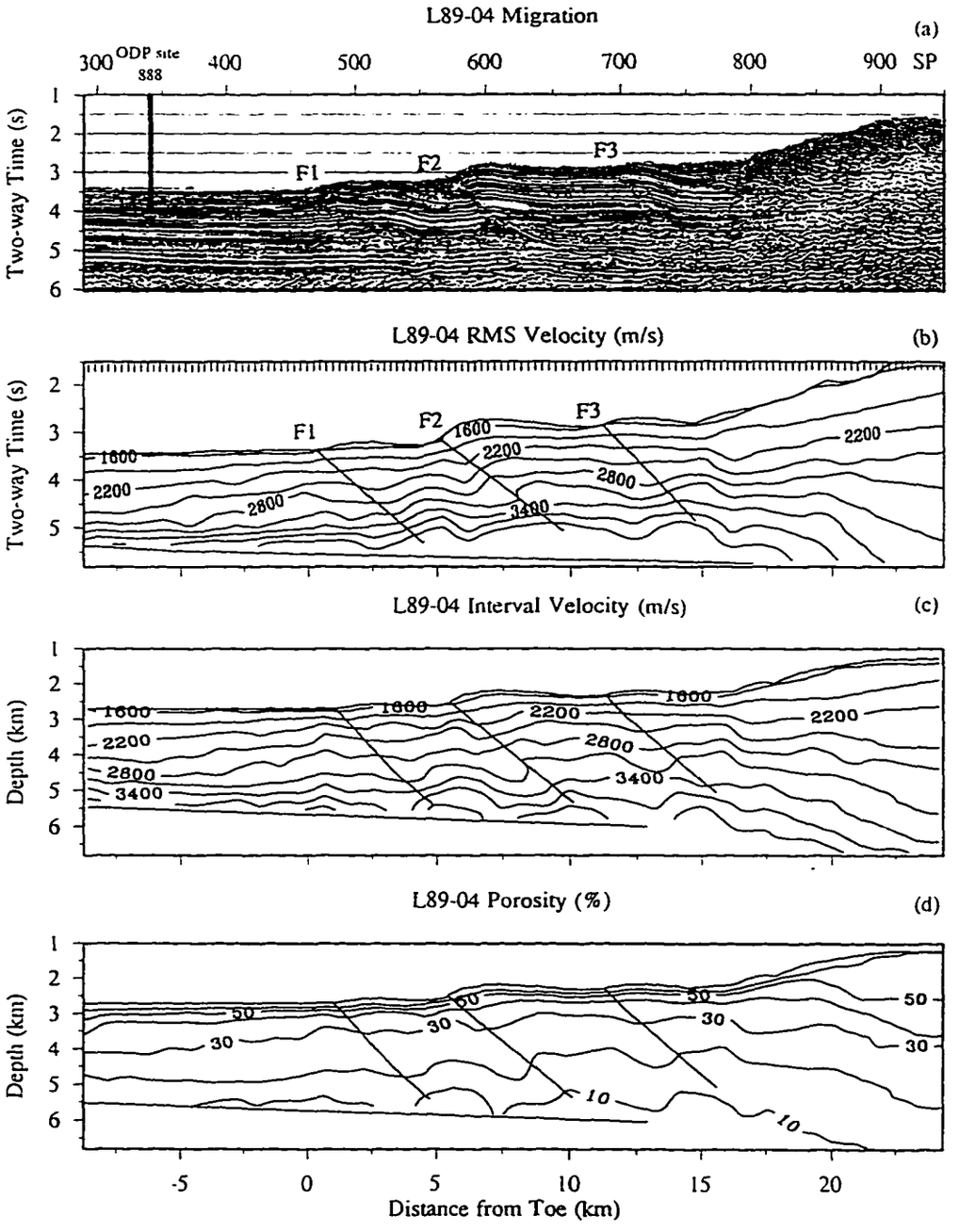

Figure 2.5 (a) Migrated L89-04 section where landward dipping faults are well developed. The thrust faults F1, F2, and F3 and their approximate locations are marked in the figures. ODP site 888 penetrated the top 600 m of the Cascadia Basin sediments on this line. (b) Interval velocity section plotted in time along L89-04 from Cascadia Basin to the lower continental slope. Locations of velocity analyses are shown by the small ticks along the top axis. (c) Interval velocity section plotted in depth. (d) Inferred porosity cross section of L89-04. The top of the oceanic crust is marked by the thin straight lines in (b)-(d).

to the high velocity of the footwall sediments, velocity values of the hanging-wall sediments near the faults and within the fault zones are relatively low, comparable to the deep sea basin velocities. Farther landward of the fault zone region and especially on the lower slope region, the trend is reversed and remarkably low velocities are observed.

To examine the compaction history of the sediment elements as they are carried landward through the frontal thrust region and incorporated into the wedge, interval velocities

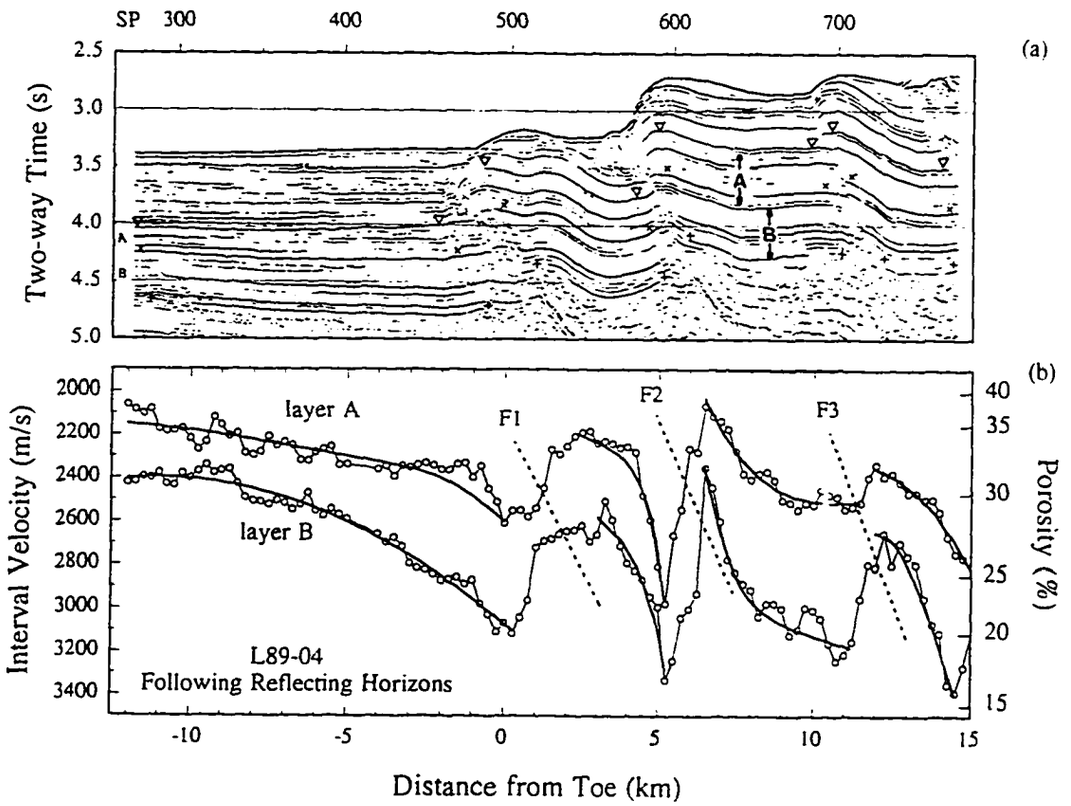

Figure 2.6 (a) L89-04 migrated section for which velocities in the two stratigraphic layers A and B are measured from Cascadia Basin across the landward dipping thrust fault zone. The horizons defining the two layers for which the velocities are determined are marked symbols (b) Interval velocities within two turbidite layers A and B as shown in Figure 2.6(a). Locations of the landward dipping faults (F1, F2, and F3) are also shown. The non-linear scale on the right shows the porosity values inferred from the velocity data as discussed in the text.

within two stratigraphic layers of the turbidite section, layer A and B (marked in Figure 2.6a), were determined along L89-04. Strong coherent reflections at the top and bottom of these two layers can be followed from the abyssal basin across the thrust faults to the lower slope (Figure 2.6a). The unsmoothed velocity data shown in Figure 2.6b probably reflect the scatter in the velocity measurements, with a maximum deviation of $\pm$5% around smooth trend values. The long wavelength smoothed curves was taken to represent the true lateral velocity variations, which are strongly influenced by the initial accretion and thrust faulting deformation. The increased compressional stress from plate convergence near the deformation front raises the sediment velocities within the two layers by 25% and 29% respectively in a distance of ~10 km before the sediments are finally accreted to the thickening wedge.

2.2.4 Seismic Velocity Structure on L89-07

From Cascadia Basin to the frontal ridge along L89-07, velocities increase steadily towards the deformation front (Fig. 2.7b and 2.7c), similar to that approaching the thrusts on L89-04. The velocity increase occurs mostly in the turbidite section. Velocities of the lower hemipelagic section show a small decrease near the deformation front, which possibly causes a pull-down effect on the oceanic crust near SP 350 in Figure 2.7a. Lower velocities are first seen within the large frontal ridge as sediments start to be incoherently deformed and thickened. Landward of the ridge in the undeformed trough, velocities similar to those in the basin are again found.

Continuous reflecting horizons cannot be easily followed landward of the thrust zone

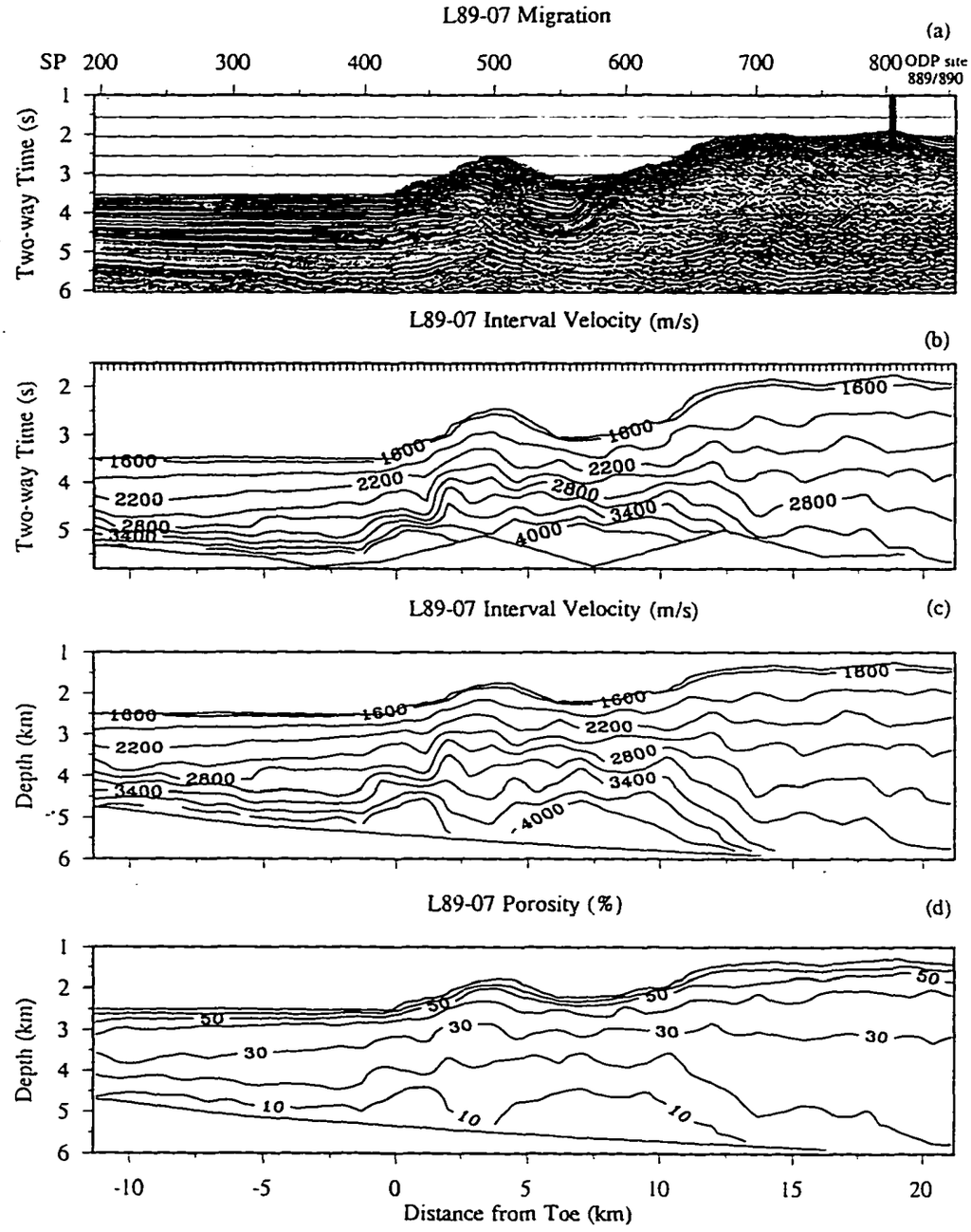

Figure 2.7 (a) L89-07 migration section where the deformation front is marked by a frontal anticlinal ridge. Location of ODP sites 889/890 drilled on the nearby L89-08 are projected onto this line. The ocean crust beneath the slope at 5.5 s is indicated by three triangles. (b) Interval velocity section plotted in time along L89-07 from Cascadia Basin to the lower continental slope. Locations of velocity analyses are shown by the small tick marks at the top. (c) Interval velocity section plotted in depth. (d) inferred porosity section of L89-07. The approximate location of the ocean crust is indicated by the thin lines in 2.7(c)-2.7(d).

as deformation produces discontinuous and incoherent reflectors. Thus, interval velocities are shown in Figure 2.8 at constant depths, 500 and 1000 m below the seafloor. In a distance of 12 km from Cascadia Basin to the deformation front, velocities increase by about 16 and 24% at the two depths. Over the same distance, a given stratigraphic horizon can be followed from the basin to near the deformation front. Velocities along two horizons are indicated by the dotted lines in Figure 2.8; these horizons are nearly equivalent to the bases of layers A and B on L89-04 (Fig. 2.6), although stratigraphy does change over the 40 km separating the two lines. Along the upper horizon, velocities increase landward from ~2000 m s^{-1} at a subbottom depth of ~500 m to ~2500 m s^{-1} at a depth of ~750 m near the deformation front. Following the lower horizon, velocities increase from ~2250 m s^{-1} at 1000 m depth in the basin to ~2900

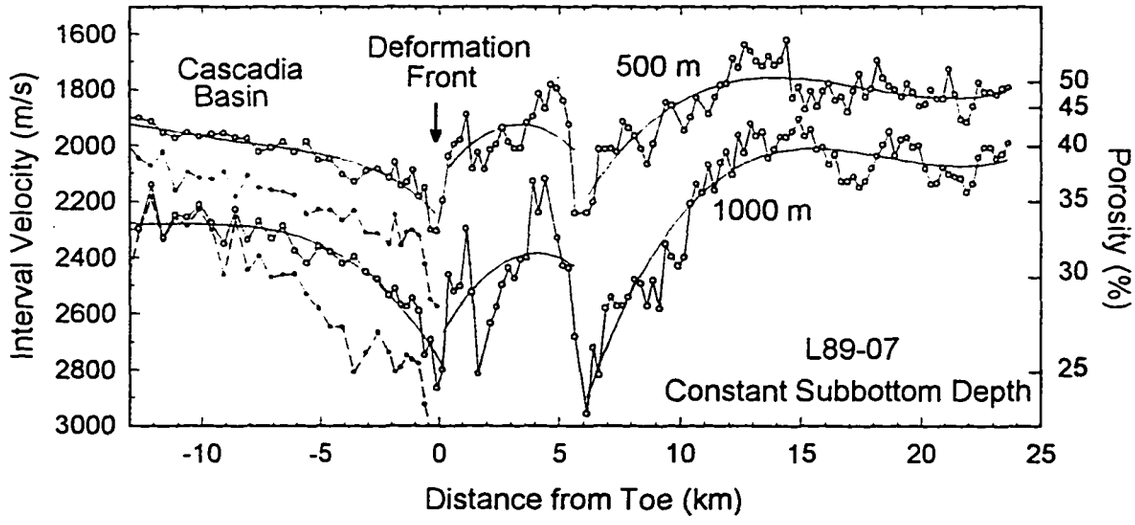

Figure 2.8 L89-07 interval velocities at constant depths, 500 and 1000 m below the seafloor, from Cascadia Basin to the lower slope region. The interval velocities seaward of the wedge toe within two reflection horizons, approximately corresponding to the base of layer A and B on L89-04 (Figure 2.6) are shown with dotted lines. The non-linear scale on the right shows the porosity values inferred from the velocity data as discussed in the text.

m s^{-1} at 1250 m depth just seaward of the deformation front. This is an increase of 29% over a distance of ~12 km, the same increase as seen on L89-04 from the basin to the toe of the wedge.

Farther landward on the lower slope of the wedge, the sediment section thickens tectonically and the sediments are strongly deformed. Velocities at particular depths drop very rapidly to values lower than those of undeformed sediments in Cascadia Basin at the same depths. The velocity variation and the wedge geometry from the deformation front to the slope region clearly indicate a correlation between the low velocity anomalies and the rapidly thickened regions of the wedge. Lower velocities on the frontal ridge and the lower slope region correlate well with the thickening due to sediment accretion. Where sediment section nearly doubles in thickness 10 km landward of the deformation front, the velocities at 500 and 1000 m are actually slightly lower (5% and 9%) than those in Cascadia Basin at the same depths. Following a sediment flow path from the abyssal basin into the accretionary wedge by assuming self-similar thickening, the sediment velocity at a depth of 500 m first increases by about 29% approaching the frontal fold, and then remains almost unchanged to a depth of 1000 m on the slope region where the section has thickened (Figure 2.8). Thus, there is no significant increase in velocity of the sediment elements being moved from the deformation front landward and deeper.

2.2.5 Constraints on the Velocities in the Slope Region

In the lower slope region, reflection coherency is partly destroyed and interference from multiples and diffractions is prominent. Thus, the velocities are less well resolved.

However, additional confirmation of the low semblance and moveout velocities in this region is provided by the depth to the subducting oceanic plate, clearly seen beneath the wedge sediments in the migrated section of L89-07 (Figure 2.7a). The vertical position of the crustal reflector on this time section is strongly affected by the laterally varying velocities, particularly beneath the lower slope region where the sediment section is much thicker than that in the basin. A true depth section obtained from the migrated time section depends on the correct velocity-depth functions. The top of the subducting Juan de Fuca oceanic crust is unusually smooth with very few seamounts [*Davis and Karsten*, 1986] and the oceanic crust is not expected to have abrupt relief in short distances. Thus, a smooth landward surface for the oceanic crust on a depth section can serve as a relative constraint on the velocities beneath the lower slope region.

The oceanic crust beneath the wedge can be traced to about 19 km landward of the deformation front along L89-07 through discontinuous but clear reflections. At a distance of 12 to 19 km from the deformation front (Figure 2.7a), the reflection at 5.5 s has an amplitude well above the background noise. It is believed to be the reflection from the oceanic crust and not a multiple because of its traveltime, moveout velocity and frequency content. Partial stacks at different offset ranges also distinguish this event from both water bottom and diffraction multiples.

Two depth sections have been obtained using velocity functions which differ only in the slope region. The locality of the oceanic crust beneath the slope region has been correctly imaged on Figure 2.9a using the low velocities on the slope region from the detailed velocity analysis. Figure 2.9b illustrates the depth section where velocities beneath the lower slope

(landward of SP 680) were the same as in the undeformed basin sediments seaward of SP 200, i.e., extrapolated from the seafloor with a velocity gradient of ~670 m s^{-1} km^{-1}. In the latter section the oceanic crust has an abrupt downward step of more than 1.5 km in a distance of less than 2 km. This atypical relief is obviously an artifact from the use of incorrect velocities in the slope region for the depth conversion. This result confirms that velocities beneath the lower slope must be lower than those at the comparable depths in Cascadia Basin.

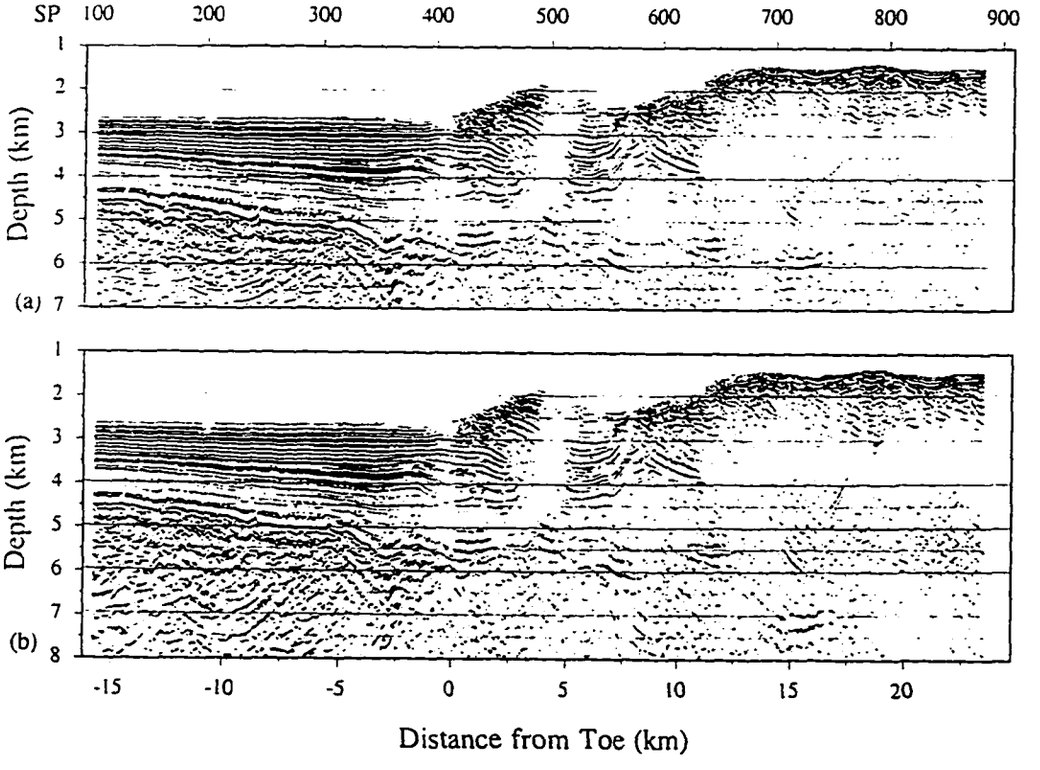

Figure 2.9 L89-07 depth sections converted from migration time sections using different velocities in the slope region. (a) Oceanic crust is imaged correctly using lower velocities in the slope region compared to those in Cascadia Basin. (b) Velocities in the slope region increase with the same gradient as in the basin, which causes variations in the depth of the oceanic crust.

Other confirmation of the velocity variation is provided by a refraction line parallel to L89-04 recorded during the 1980 Vancouver Island Seismic Project [*Ellis et al.*, 1983]. The arrivals from large air-gun shots and explosions were recorded on ocean bottom seismographs, OBS #1, #3, and #5 (Figure 2.10), deployed at 45 km seaward, 20 km landward, and 55 km landward of the deformation front, respectively. Although refraction velocity can be inaccurate due to the effect of stratigraphic dips and there is less reduction of random error through stacking, the analysis of refraction data usually provide more precisely determined functions of velocity with depth than those obtained from reflection data. This is because the refracted phase can yield velocity structure to greater depths and in regions where there are no distinct reflectors. These advantages are most valuable on the slope region where reflection coherency is generally poor.

The refraction velocity-depth functions of *Waldron et al.* [1990] are displayed in Figure 2.10. The velocity functions for Cascadia Basin and the continental slope derived from the 1989 reflection data are also shown for comparison. In Cascadia Basin below the upper turbidite sediments, the lower hemipelagic section is distinguished by its higher velocity gradient as seen from OBS #1. On the lower slope region 20 km from the deformation front where the reflection velocities are low, the refraction data require a corresponding significantly lower velocity gradient. This leads to a much lower average velocity compared to the velocities in the basin at the same depths (OBS #3 in Figure 2.10). The low refraction velocities are similar to the values obtained from the semblance velocity analysis and maintained for nearly the entire sediment section of the wedge in the lower slope. Farther landward on the mid to upper slope region, no reliable velocity information was obtained from

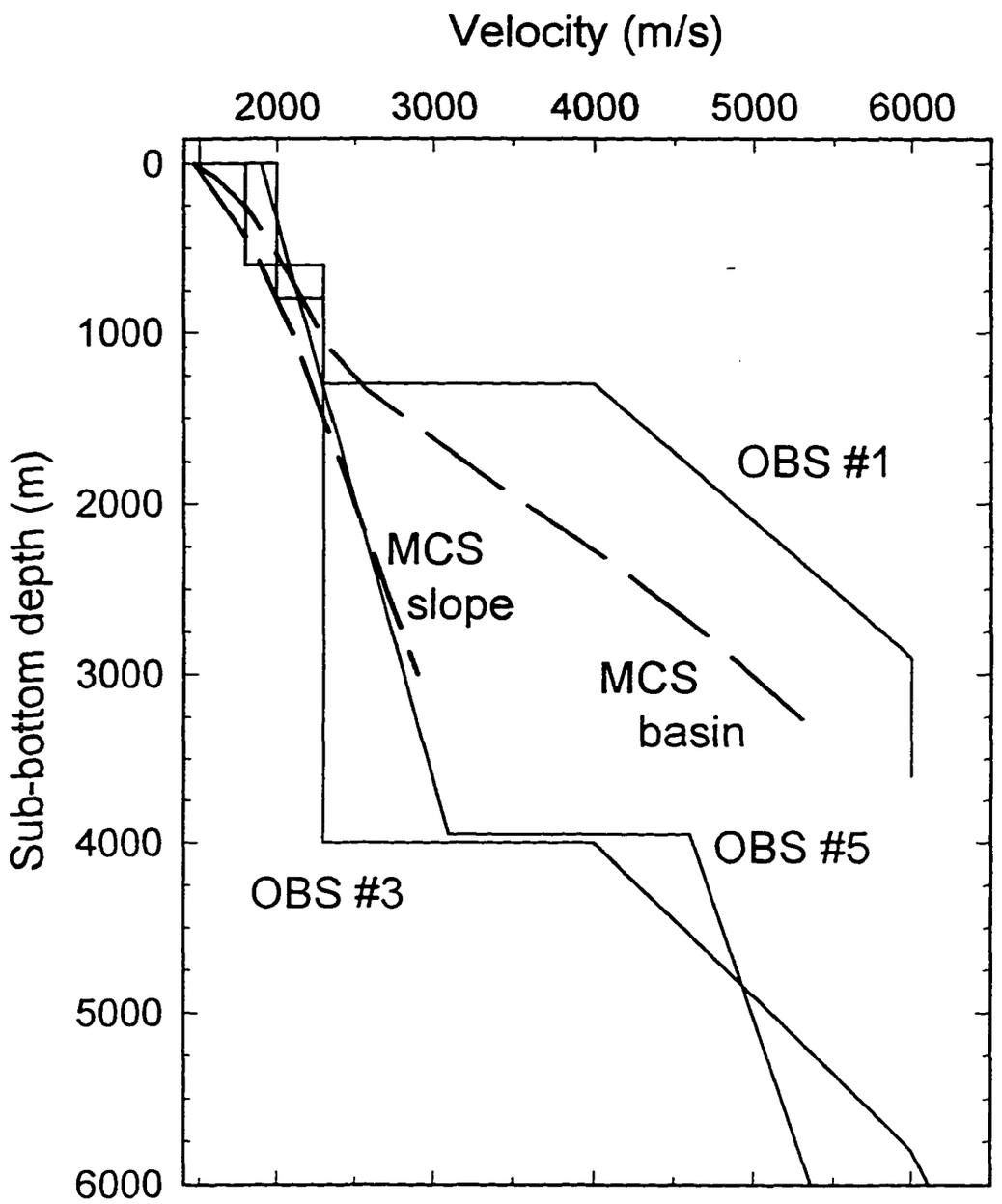

Figure 2.10 Velocity-depth profiles from a 1980 OBS survey along the Cascadia margin [*Waldron et al.*, 1990]. Three OBSs were deployed along a line approximately coincident with L89-04. OBS locations were 45 km seaward of the deformation front in Cascadia Basin (OBS #1), 20 km landward of the deformation front on the lower slope (OBS #3), and 55 km landward of the deformation front on the upper slope (OBS #5), respectively. Velocity-depth interpretations from the refraction data are shown in solid lines [from *Waldron et al.*, 1990]. The velocity functions determined from the velocity analyses using the 1989 multichannel seismic data are also shown in thick dashed lines (see Figure 2.12).

the reflection semblance analysis. However, the refraction data of OBS #5 suggest low velocities, but a small increase compared to the lower slope region.

2.3 Sediment Porosity Variations of the Accretionary Prism

The most important application of the sediment velocity data is to estimate porosity variations across the accretion zone, and thus the pattern of fluid loss. Empirical relationships between velocity and porosity have been established from velocity, bulk density and porosity measured in recovered drill cores and from in situ well logs in numerous investigations of accretionary wedges [e.g., *Bray and Karig*, 1985; *Fowler et al.*, 1985; *Bangs, et al.*, 1990; *Westbrook*, 1991; *Davis and Villinger*, 1992; *Hyndman et al.*, 1993b]. Lithology is an important factor in velocity/porosity relationships, including grain mineralogy, sediment cementation and diagenesis. The effect of fracturing may also be important. On the seismic reflection profiles, the character of the incoming basin sediment sequences does not vary laterally to any great extent [*Davis and Hyndman*, 1989], which suggests that the bulk sediment composition does not vary significantly. Thus, the main factors that might change the velocity/porosity relationship laterally are cementation (i.e., matrix frame strength) and fracturing (i.e., change in "pore" geometry).

ODP Leg 146 focused on the role of sediment consolidation and fluid expulsion in the development of the Cascadia accretionary prism. Sites 888 and 889/890 penetrated sediment sections down to a depth of 556 in Cascadia Basin and 386 m in the lower slope region (Figures 2.1, 2.5a and 2.7a). The physical properties of the sediments measured from cored samples and downhole logging do not indicate significant effects of sediment cementation and

diagenesis at sites in the basin compared to the slope sites, and the velocity/porosity relations from the basin and slope sites are very similar [*Westbrook at el.*, 1994].

The margin sites of Leg 146 were shallow (penetration up to 386 m below seafloor on the slope), but ODP Leg 139 drilled the Cascadia Basin sediments to a maximum depth of 936 m in the Middle Valley area of the Juan de Fuca Ridge ~180 km west of the deformation front. The sediments drilled were terrigenous turbidites probably of similar composition to those being incorporated in the accretionary wedge, but they were deposited at the ridge region subject to hydrothermal alteration. One might expect that the sediments deposited in high-temperature conditions or heated post-depositionally would have a different velocity-porosity relationship relative to those at comparatively cooler locations, as might have be suggested by very different velocity-depth profiles between normally compacted and hydrothermally altered materials [*Davis and Fisher*, 1994]. However, comparisons of porosities from the core measurements in different sites where hydrothermal conditions differ considerably, show remarkably similar velocity-porosity relationship regardless of the high degrees of hydrothermal alteration [*Davis and Fisher*, 1994]. Compaction is believed to be the dominant mechanism by which the pore space is reduced even in the ridge region, and sediments accreted to the wedge are not expected to behave much differently. Therefore, a single velocity/porosity relationship was used to infer semiquantitatively sediment porosities from our measured velocities both for Cascadia Basin and for the frontal region of the wedge.

For a particular lithology, porosity is close to a single valued function of velocity, with velocity changes dependent primarily on porosity differences. An empirical relationship was initially established by *Davis and Villinger* [1992] based on the data from *Han et al.* [1986]

and *Jarrard et al.* [1989] for shales containing 50% clay. *Hyndman et al.* [1993b] re-examined this velocity-porosity relationship based on measurements of seismic velocities and porosities from recovered drill cores and down hole logging in Nakai Trough southeast of Japan where sediments are similar to those of the Cascadia margin. The derived velocity-porosity relationship was used in this study to infer porosity values:

$$\phi = -1.18 + \frac{8.607}{V} - \frac{17.89}{V^2} + \frac{13.94}{V^3}, \tag{2.2}$$

where interval velocity V is in km/s. This relationship is supported by comparison with the

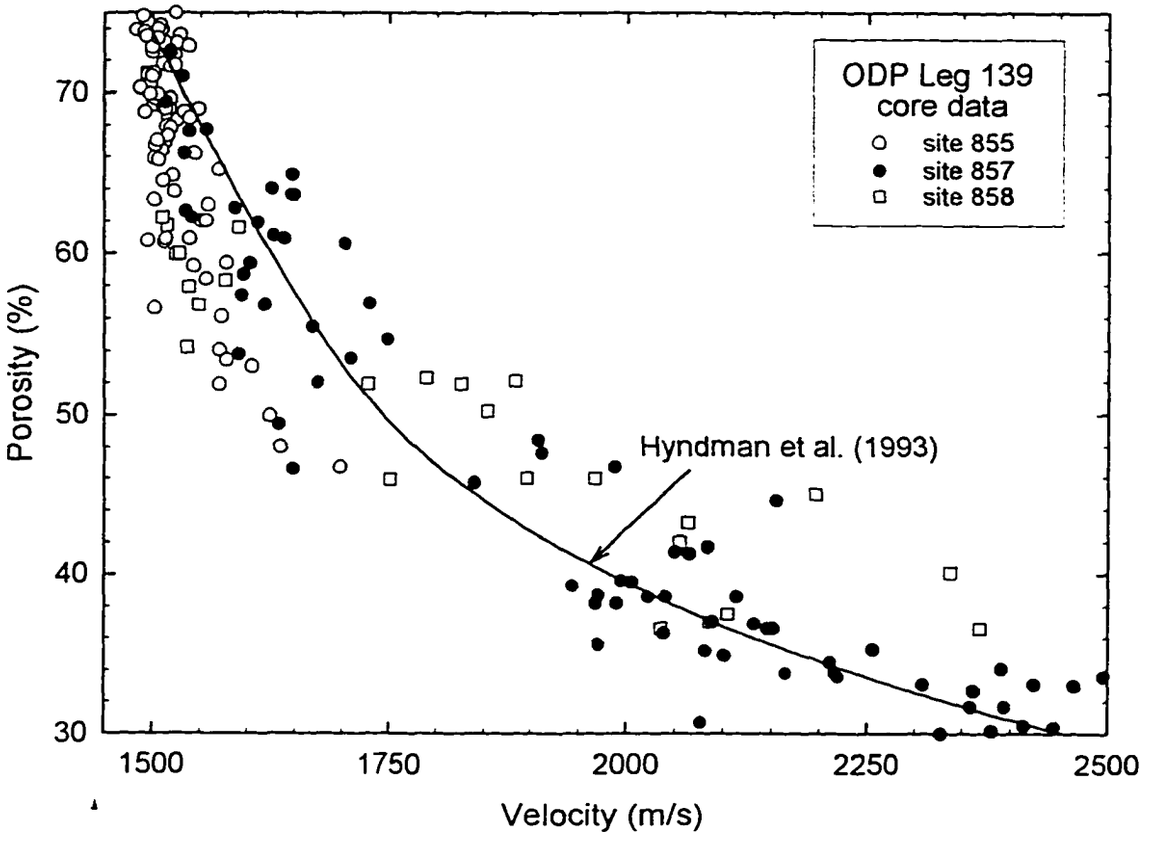

Figure 2.11 Velocity and porosity measurements from ODP sites 855, 857, and 858 of Leg 139, on the landward side of the Juan de Fuca Ridge [from *Davis et al., 1992].* The heavy line is the velocity/porosity relationship used in this study [from *Hyndman et al.*, 1993b].

core measurements from three sites of ODP Leg 139 (Figure 2.11). Site 857 penetrated is a thick and locally continuous sediment section outside the centre of rifting in Middle Valley [*Davis et al.* 1992; *Davis and Fisher*, 1994]. The measured porosity and velocity values at this site match very well with the porosity-velocity relationship of *Davis and Villinger* [1992] and *Hyndman et al.* [1993b] (Figure 2.11).

The above velocity/porosity relationship was applied in constructing the porosity sections shown in Figures 2.5d and 2.7d. The inferred porosities are used to indicate first relative porosity differences, and second, semi-quantitatively, pore pressure differences. Figures 2.12a and 2.12b show a compilation of RMS and interval velocities and Figure 2.13 the derived porosities from three different regions: (1) in Cascadia Basin where sediments are little influenced by the stress regime of the wedge, (2) just seaward of the deformation front and of each thrust fault, and (3) ~20 km landward of the deformation front on the lower slope where the prism has approximately doubled in thickness. The RMS and interval velocities of the slope region (Figure 2.12) are taken from both L89-07 and 89-10; only porosities from L89-10, where the low velocity region is especially clearly defined, are displayed in Figure 2.13. The velocities and porosities in the basin illustrate a contrast between the turbidite and hemipelagic sections with a gradient change near the sub-bottom depth of 1400 m, but substantially different velocity and porosity profiles are evident for the fault and slope region sediments.

Studies of sediment consolidation and cementation generally indicate gradual decrease in porosity with depth under gravitational stress. The solid line in Figure 2.13, determined using all coverage of the survey in Cascadia Basin as well as from the results of the detailed

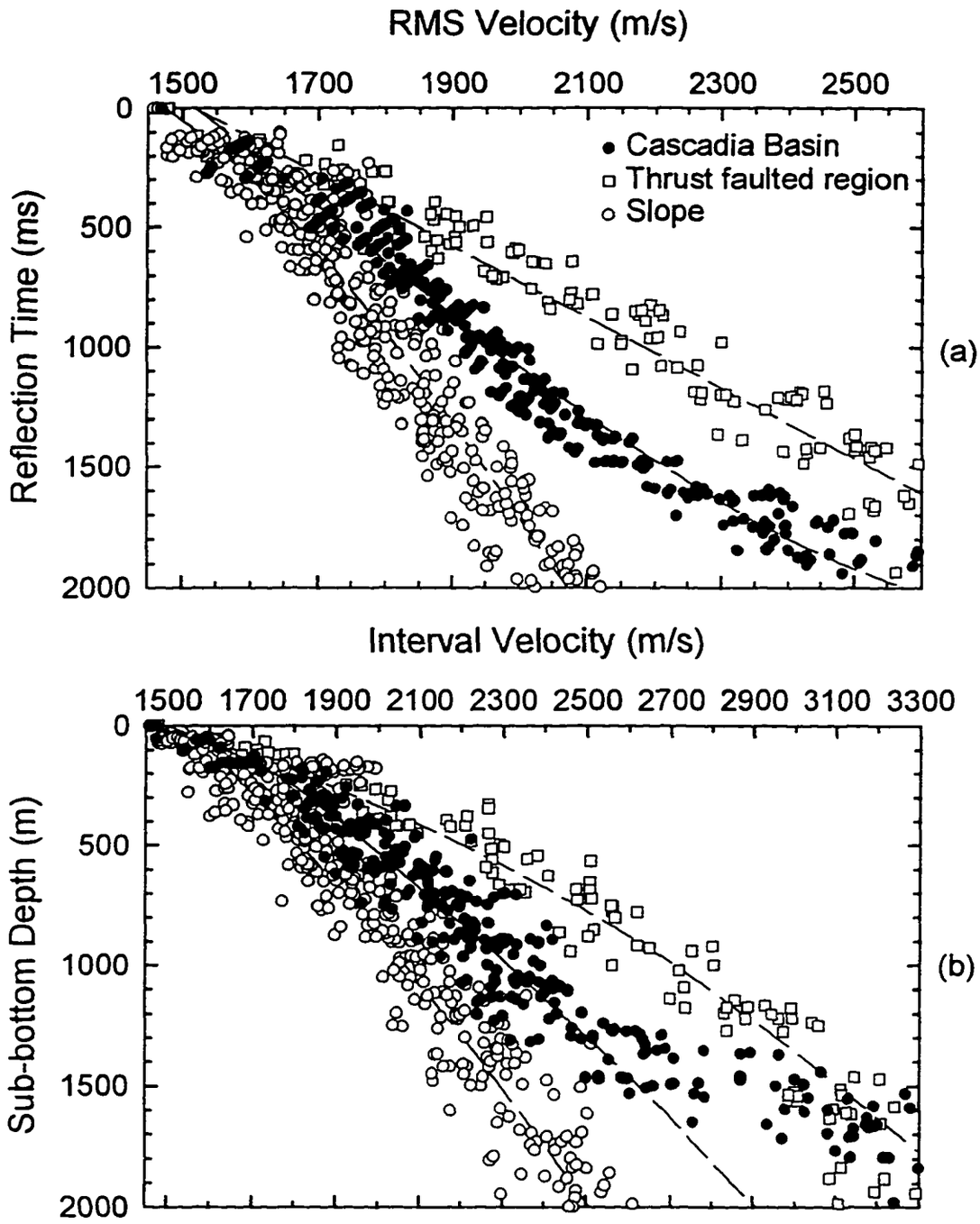

Figure 2.12 (a) RMS velocity/traveltime data for three regions: in Cascadia Basin, near the deformation front and seaward of each thrust, and on the lower slope where sediment section is thickened by about a factor of 2. (b) Interval velocity/subbottom depth data for the three regions. A change in the velocity gradient at 1400 m corresponds to a change from turbidite to hemipelagic sediment sections.

velocity analyses on L89-04 and 89-07 where sediments are believed to be least influenced by the horizontal compressional stress, has been used as a reference function to represent the near normal sediment consolidation. The gross variations in sediment consolidation, overconsolidation or underconsolidation, can then be estimated by deviations from the reference. The quantitative estimates however should be viewed with caution as: (1) sediments in the basin were deposited very rapidly and thus may be somewhat underconsolidated, (2) sediments in the basin area may not be totally free of influence of the

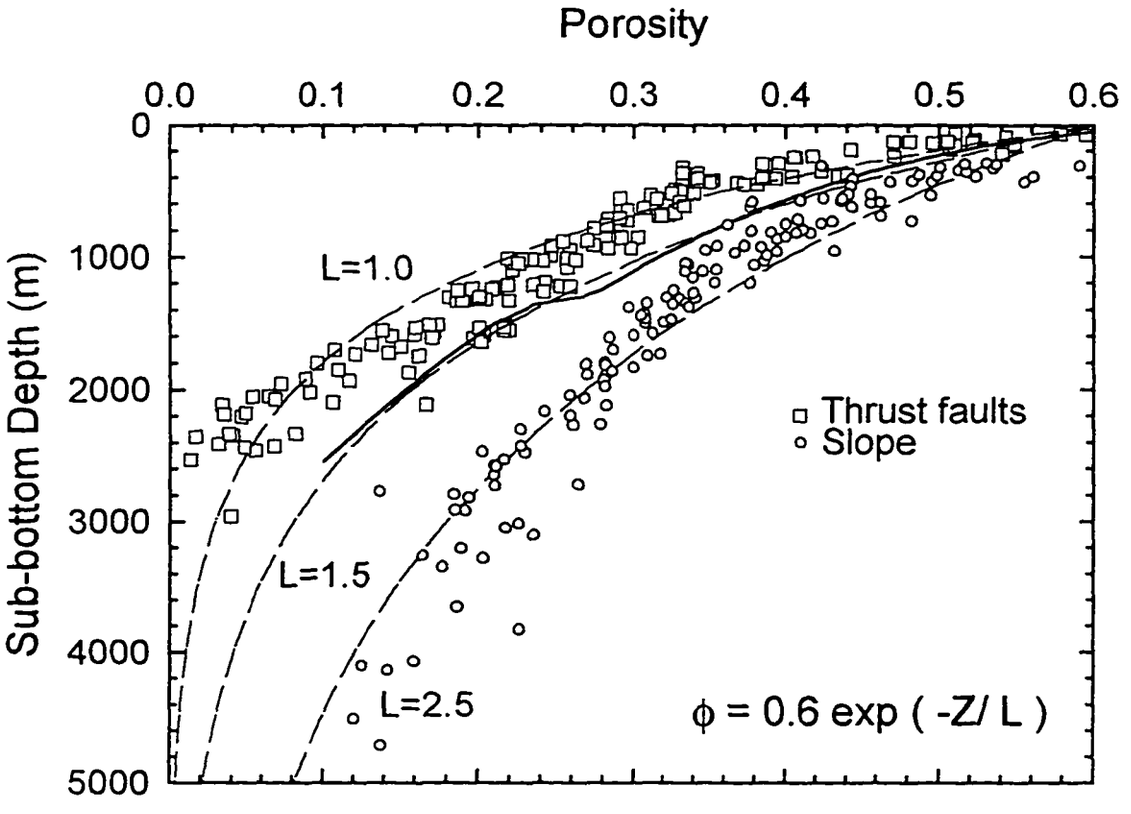

Figure 2.13 Sediment porosity/depth data from the velocities in Figure 2.12. The porosities have been obtained using the velocity/porosity relation of equation 2.2 assuming 50% clay content. Porosity at the seafloor is taken as 0.6 [*Westbrook et al.*, 1994].

horizontal tectonic stress, (3) lateral variations in the velocity/porosity relation may occur in the deeper portion of the accretionary wedge that are not detected by the relatively shallow drilling data, and (4) fracturing of sediments and overpressuring of pore fluids reduce sediment velocities but may not change porosity proportionately so as to keep the velocity/porosity relation unchanged.

2.3.1 Sediment Overcompaction and Fluid Expulsion Seaward of the Deformation Front

Approaching the deformation front at a fixed depth or following particular stratigraphic horizons, sediment velocities are observed to increase and the inferred porosities decrease substantially landward as shown in Figures 2.6b and 2.8. Porosity reductions from 35 and 30% in Cascadia Basin to 28 and 20% just seaward of the deformation front in two stratigraphic layers (layer A and B in Figure 2.6b) occur over a distance of ~10 km. Similar porosity change is also observed in Figure 2.8 on the seaward portion of L89-07. The depths to these layers increase only a small amount within the measured distance, so that the velocity increase must be mainly due to an increase in horizontal tectonic stress that consolidates the sediments in the initial stage of accretion. Assuming that they are close to normal consolidation in Cascadia Basin, the sediment in this region must be substantially overconsolidated and pore fluids be lost rapidly seaward of the wedge toe before they are accreted to the wedge.

The volume of sediment mass is unchanged during the consolidation process, and the proportional volume loss of pore fluid from initial fluid content can be estimated from $(\phi_o - \phi)/[\phi_o(1-\phi)]$, where ϕ_o and ϕ are the initial and final porosities respectively. Within the two

stratigraphic layers noted above, 28 and 42% of the original content of pore water is lost as a result of increasing horizontal compaction stress. Using a subduction rate of 45 km ma^{-1} [*Riddihough*, 1984], an initial sediment thickness of 3 km and an average sediment porosity of 30% in the basin, fluid loss of 35% on average in the sediment column over a distance of 12 km indicates a fluid expulsion rate of 0.0012 $m^3 m^{-2} a^{-1}$ in a diffusive flow over the surface area landward of the prism toe, or an average fluid discharge rate of about $1.2x10^{-3}$ m a^{-1}. Most of the fluid expulsion must occur near the wedge toe, as indicated by the rapid increase of velocities, so the maximum fluid expulsion rate is probably several times greater. Off Oregon margin, evaluation of fluid inventory, as defined by P-wave velocity distribution, indicates that sediment pore fluid is lost at a nearly constant discharge rate of up to $1.3x10^{-3}$ m a^{-1} across the lowermost 18 km of the accretionary prism [*Carson and Westbrook*, 1995]. This estimate is very similar to the average discharge rate on the northern Cascadia margin obtained in this study.

Within each fault block, porosities are high in the hanging wall near the uplifted anticlines and low in the footwall section (Figure 2.6b). The high velocities and the corresponding low porosities of the footwall sediments near thrusts are apparently due to the progressive compaction landwards. The hanging wall sediments, on the other hand, are thickened and uplifted with little velocity change and fluid loss. This phenomenon has also been observed by *Westbrook* [1991] based on porosity variation in a thrust slice at the toe of the Barbados Ridge accretionary wedge. Within the thrust, decrease of sediment volume reached a maximum of 30% in the foot wall part and almost no volume loss occurred in the hanging wall part of the same stratigraphic layer. Undercompaction associated with rapid

thickening and uplift retains pore fluids in the hanging wall section with little change in sediment velocity. This effect of tectonic underconsolidation resulting from the sediment thickening is more evident on the lower slope region.

2.3.2 Sediment Undercompaction and Delayed Dewatering Landward of the Deformation Front

The generation of an underconsolidated sediment section is best seen on L89-07. Velocities of the slope sediments are significantly lower relative to those in the undeformed sequence of Cascadia Basin at comparable sub-bottom depths (Figures 2.7, 2.8, and 2.12b). The landward porosity deviation from the basin reference in Figure 2.13 represents underconsolidation of the wedge sediments 10 km landward of the deformation front. The rapid thickening of the wedge results in sediment elements being moved to greater depths landwards with little velocity change and inferred porosity loss. This is illustrated in Figure 2.8 where the slope velocities at a depth of 1000 m are similar to the velocities seaward of the deformation front at a depth of 500 m. The slow consolidation response of the sediments to the thickening is mostly responsible for the low velocities in the slope section.

The porosity-depth profile derived from the velocity data was used in constructing a numeric model that explains the discrepancy between heat flow determined from the depth of the hydrate BSR and that predicted by a regional model [*Hyndman et al.*, 1993a; *Wang et al.*, 1993]. The heat flow from the depth of the BSR is 20% less than the prediction of model without sediment thickening and fluid expulsion. The reduction of the heat flow was attributed to horizontal shortening and thickening of the sediment section that vertically

stretches the isotherms faster than thermal reequilibration can occur. This is the same process which vertically stretches the porosity-depth profile resulting in low sediment velocities in the slope region.

Similar low velocity and high porosity anomalies within the frontal part of accretionary complexes were reported at the Cascadia margin to the south of the Vancouver Island margin [*Lewis*, 1990; *Cochrane et al.*, 1994] and the Barbados accretionary margin [*Bangs et al.*, 1990]. Seismic refraction and reflection data were recorded off Washington/Oregon margin at similar structural locations on the southern Cascadia accretionary wedge. A region of low velocity sediments, comparable to those found off Vancouver margin, was reported at the wedge toe along an uplifted ridge [*Lewis*, 1992; *Cochrane et al.*, 1994], and the velocity anomaly was interpreted as the result of tectonically induced folding causing a reduction of rigidity and increase in porosity of the sediments. The low velocities of the Barbados region were interpreted to result from sediments with high porosity that have not fully consolidated following rapid tectonic thickening due to slow fluid expulsion. *Bangs et al.* [1990] further suggested the possibility of a dilatational process in which fluids were transmitted at high pressures seaward from the prism into the basin sediments producing abnormally high porosity even before the sediments entered the accretionary wedge. However, the seismic data for the Vancouver Island margin show high rather than low velocities in the frontal thrust area that indicate pore fluid loss and overconsolidation seaward of the deformation front. On the northern Cascadia margin, the low velocities landward of the deformation front are interpreted to be mainly the result of sediment underconsolidation associated with the rapid tectonic thickening. The slightly lower average velocity of the slope region compared with

that of the abyssal basin, as illustrated by both refraction and reflection data, may imply a similar landward increase in porosity of sediment elements, such as that caused by tectonically induced folding and fracturing seen within the fault block between SP 640 and 690 on L89-04 (Figure 2.6). High pore pressure resulting from rapid sediment thickening and loading may also contribute to the low slope velocities. However, the average velocity decrease probably does not represent a sediment element porosity increase.

One alternative explanation for the low average velocity on the slope is that in the past only the upper high porosity portion of the incoming sediments was involved in the accretion. The deeper high velocity, low porosity sediments were underthrusted to greater depths, in contrast to the offscraping of the entire incoming section at present. In most other accretionary prisms in the world, including parts of the Oregon margin [*Cochrane et al.*, 1994], decollements develop in the sediment section some distance above the subducting plate. However, there is little definite supporting evidence that such differentiation occurred previously on the northern Cascadia margin. A second explanation for the apparent landward average porosity increase of the total sediment column is that there is a small landward change in the velocity/porosity relation because of the pervasive fracturing, or there is a general decrease in the effective stress and hence bulk frame modulus due to increasing pore-fluid pressure, and thus a true and substantial change in the velocity-porosity relationship.

The low-velocity slope section is developed from a mixture of overconsolidated sediments, such as those near the deformation front, and normally consolidated sediments farther seaward. This configuration can be readily seen within each fault block. Therefore, the sediment porosities near the deformation front cannot be simply compared with those in

the slope region. A more direct way is to measure the porosity change from the basin to the slope, which gives an approximation of the total fluid loss during the accretion process.

Under normal consolidation, sediment porosity change can usually be approximated as decreasing exponentially with depth (Athy's law) [*Einsele*, 1997], $\phi = \phi_o \exp(-Z/L)$, where ϕ_o is porosity value at the surface, Z is sub-surface depth and L is a depth constant controlled by the sediment lithology and depositional regime. Figure 2.13 compares the derived sediment porosities of different regions with exponential approximations. Porosities of the basin sediments closely fit an exponential profile where L=1.5 km. Near the deformation front and thrust faults, porosities can be approximated by a profile with L=1.0 km. If the basin sediment section were thickened with no porosity loss, from 2.5-3.0 km to 5.0-6.0 km as observed on the reflection sections, the porosities should be approximated by a profile with L=3 km. The slope sediment porosities are however approximated with an exponential curve where L=2.5 km. The fact that the slope porosities are lower than the L=3 km prediction allows a measure for the total amount of fluid expelled from the sediment section as it travels from the basin to the slope region. This estimate, obtained by integrating the porosity-depth function, is equivalent to about 30% of the total fluid content that have been expelled during accretion process. The estimate agrees with the value of fluid loss from the velocity increase near the prism toe as discussed above. This further suggests that no large amount of pore fluid loss and velocity change on the lower slope region is required, since the derived amount of fluid loss has already occurred seaward of the deformation front before the sediments are accreted to the wedge. It should also be pointed out that a large amount of fluid expulsion from the deep part of the slope sediment section can still occur if the rate of sediment

thickening is comparable to the rate of fluid expulsion. As compaction proceeds farther landward, the remaining pore fluids in the slope sediments may be released and the porosity profile restored to an L of 1.5 km or smaller value to re-establish the equilibrium of consolidation. No adequate velocity information from the multichannel reflection data have been obtained to define this recovery well. However, a small velocity increase is observed in the OBS refraction data on the upper slope [*Waldron*, 1990] and a full recovery to normal consolidation is seen clearly in the Barbados data of *Bangs et al.* [1990].

The horizontal shortening and vertical stretching of the sediment column results in much higher porosities in the slope region compared with those in the basin at the same depths. The seismic velocity and the derived porosity data indicate a correlation between tectonic accretion and sediment underconsolidation on the Cascadia margin. Thickening of the wedge sediments, at the anticlinal deformed ridge and the lower slope, is at a rate greater than the ability of the sediments to expel their fluids and maintain a normal consolidation porosity profile. The time lag between sediment thickening when they enter the accretionary wedge and the porosity reduction due to pore fluid expulsion is estimated as at least 0.2-0.4 Ma. The lower-slope sediment porosity greater than for normal consolidation must be supported by increased fluid pressures, which could also contribute to the low seismic velocities of the region. These high pore pressures have an important influence on the wedge structure geometry and sediment properties.

2.4 Sediment Pore Pressures Estimated from Velocity Data

Pore fluid pressure may be semiquantitatively estimated from the differences between

actual porosity and porosity in a normal sedimentary section at the same depth, given two important assumptions [*Westbrook*, 1991]: (1) the porosity-depth function in Cascadia Basin represents the equilibrium normal consolidation profile with nearly hydrostatic pore pressure, and (2) the effective pressure at any point in the accretionary prism is equal to that beneath Cascadia Basin at a depth where the porosity is the same. As the porosity/velocity relationship is defined [*Davis and Villinger*, 1992; *Hyndman et al.*, 1993b], the effective or differential pressure (overlying load pressure minus pore pressure) can be directly related to velocity. Using velocity to indicate effective pressure, and calculating lithostatic pressure by integrating the density of the overlying sediments over their thickness, the ratio of pore fluid pressure to lithostatic pressure, λ, is defined as:

$$\lambda = \frac{P_{pore}}{P_{lith}} = \frac{P_{lith} - P_{eff}}{P_{lith}}, \qquad (3.3)$$

where P_{pore}, P_{eff}, and P_{lith} are the pore pressure, effective pressure and lithostatic pressure.

The above calculation was applied across seismic section L89-07 to infer pore pressure from velocities. The effective pressure in Cascadia Basin, taken to be a reference representing hydrostatic pressure, was computed using a grain density of 2.65 [*Westbrook et al.*, 1994] and water density of 1.05 g cm $^{-3}$. The effective pressure from interval velocity in the accretion zone was inferred from the relation between effective pressure and velocity determined using an average interval velocity-depth function from seaward portion of the line in Cascadia Basin.

The resulting cross section of λ is given in Figure 2.14. On the seaward side of the

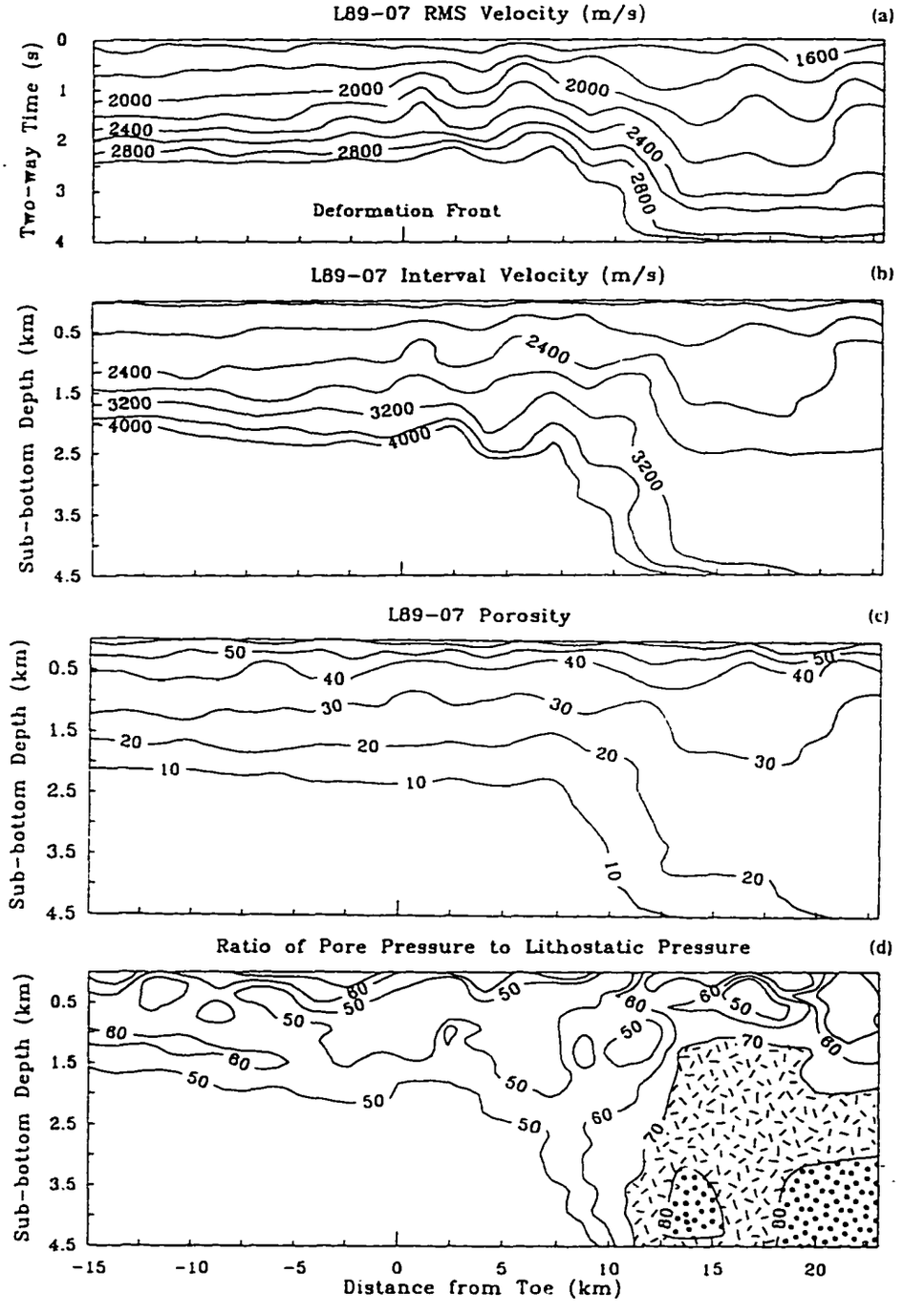

Figure 2.14 Cross-sections across the accretionary prism of (a) RMS velocity, (b) interval velocity, (c) porosity (contours in percent), and (d) pore pressure parameter λ (ratio of pore pressure to lithostatic pressure, in percent), estimated from velocity data from L89-07. Depths are in kilometre below seafloor. The top of the oceanic crust is approximately at the deepest contour; the abrupt steepening near 7.5 km from the wedge toe is an artifact resulting from flattening the seafloor.

deformation front, the value of λ is about 0.5 for hydrostatic pressure. There is a region of very high pore pressure 20 km from the deformation front, where λ reaches 0.8. The same pattern for the high pore pressure was also found in the Barbados accretionary prism using the same technique [*Westbrook*, 1991], where the zones of high pore pressure correspond to regions of undercompaction.

The pore pressure for the accretionary prism sediments is slightly less than but similar to that estimated by *Davis and Hyndman* [1989] using the critical taper theory. Values of pore pressure inferred by this method are likely underestimated, because the assumption that the reference velocity-effective pressure function derived in Cascadia Basin may not represent a hydrostatic condition. Any overpressuring in the Cascadia Basin, which is not unlikely, will mean that the effective pressure derived from the reference on the basis that they are hydrostatic will be overestimated and pore pressure be underestimated.

Hyndman et al. [1993a] and *Wang et al.* [1994] have applied the self-similar kinematic thickening model of *Wang* [1994] to the northern Cascadia accretionary prism, with constraints provided by the pattern of surface heat flow and porosity variation estimated from the velocities presented in

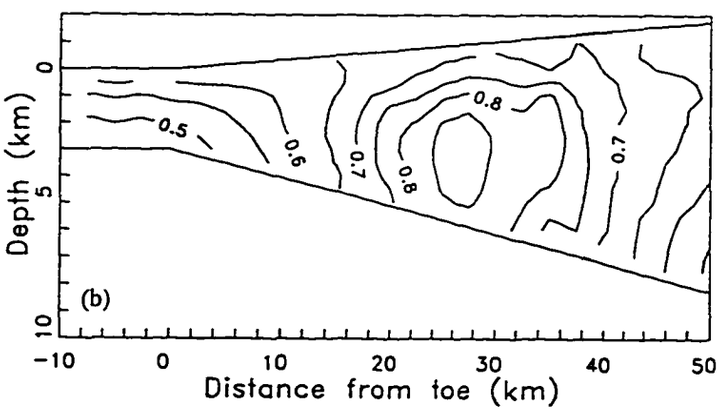

Figure 2.15 Pore pressure distribution (ratio to lithostatic pressure) across the frontal portion of the accretionary prism from the numerical model of *Wang et al.* [1993] that corresponds well with that estimated from the velocity data shown in Figure 2.14.

Figure 2.12. An important inference from the numerical modelling is that the sediments in the 30 km wide frontal portion of the accretionary prism are underconsolidated and therefore high pore pressure must exist in the accretion zone (Figure 2.15). The excess pore pressure is close to lithostatic, λ=0.8, which corresponds well with that estimated from the velocity data shown in Figure 2.14 within a region 10-20 km landward of the deformation front.

2.5 Conclusions

Within the sediments of Cascadia Basin approaching the deformation front, and within the frontal thrust zone of the accretionary prism, velocities increase landwards indicating initial sediment overconsolidation associated with horizontal compression. A remarkable conclusion is that more than one-third of the initial pore fluid content of the incoming sediments is lost by the time they are incorporated into the wedge, probably as a consequence of compressive tectonic stress. The implied large amount of fluid discharge seaward of the deformation front may provide explanation for both diffusive and focused fluid expulsion in the sediment section just seaward of accretionary complexes, e.g., mud volcanoes in the Barbados margin [*Le Pichon et al.*, 1990] and the high heat flow in Nankai Trough [*Yamano et al.*, 1992].

In the main accretion zone 15-20 km landward of the deformation front where the wedge thickens rapidly and sediments within the wedge are strongly deformed, much lower seismic velocities are observed in comparison with the sediment velocities in Cascadia basin at the same depths. The lower velocities indicate much higher porosities at given depths and thus underconsolidation with respect to the Cascadia Basin section. Sediment thickening by

overthrusting, folding and internal deformation increase the overburden stress in the wedge faster than the sediments can respond by fluid expulsion. Increased fluid pressures must result; substantial porosity loss and fluid expulsion are delayed to 15-20 km farther inland. The sediments will continue to lose pore fluids and exhibit pervasive fluid flow as they are incorporated further into the accretionary wedge.

CHAPTER 3 SEISMIC VELOCITY STUDIES OF GAS HYDRATE BOTTOM-SIMULATING REFLECTORS OF THE ACCRETIONARY PRISM

Information on marine gas hydrates and underlying free gas comes from several main sources, including seismic studies and deep sea drilling. As drilling of hydrates has only recently been approved by the Ocean Drilling Program, in situ information from drill cores and downhole geophysical measurements is very limited. Much of the available information as to the origin of BSRs and the distribution of gas hydrates has come from seismic data, and previous inferences of hydrate occurrences have been based on the presence of BSRs. The few borehole data, including downhole logging and vertical seismic profile (VSP) data, obtained at ODP Sites 889/890 on the northern Cascadia margin provide essential calibration and reference information for interpreting the seismic results. Seismic velocities in hydrate-bearing sediments are increased by the presence of hydrate overlying the BSR. If there is free gas beneath the BSR, it should result in a sharp reduction in compressional velocity. In this section, seismic velocity structure above and below the BSR on the Cascadia margin offshore Vancouver Island is examined using data from an integration of previously published ODP Leg 146 downhole logging and VSP velocities with detailed multichannel seismic (MCS) velocity analysis results. The critical reference velocity-depth profile for the accretionary prism sediments has been established using the MCS velocities to provide a starting velocity

model for full waveform inversion and to estimate hydrate concentration in sediment pore spaces later in this study. This reference profile is also constrained by analyses of the ODP downhole density and other logging data. Much of the work in this chapter is summarized in *Yuan et al.* [1996].

3.1 Gas Hydrate Formation in Accretionary Wedge Sediments

Research on the hydrate formation and dissociation in marine sediments is currently in its infancy stage. The origin of the methane, although clearly biogenic, is not well understand. Nor is the process by which the methane is concentrated in the hydrate. The stability pressure-temperature conditions for methane hydrate is now quite well know from laboratory data, and there is a general agreement with the in situ P-T conditions. However, preliminary results at recent ODP Leg 164 on the Blake Ridge showed that there were 40-100 m differences between the predicted base of hydrate stability, determined from in situ temperature measurements, and the observed BSR depth [*Matsumoto*, 1996]. This discrepancy may indicate that the experimentally determined P-T conditions for the stability of methane hydrate are not entirely applicable for the prediction of the natural gas hydrate stability field in marine sediments. Both laboratory experiments and field measurements are needed to further our understanding of the processes involved in the marine hydrate formation and dissociation.

3.1.1 Structure and Stability Conditions of Gas Hydrates

Gas hydrates, also called gas clathrates, are a special type of inclusion compound. On

freezing, water ordinary forms ice in a hexagonal crystal structure. In the presence of sufficient methane and other gases, water crystallizes in a cubic lattice that traps the gas molecules. Water molecules of gas hydrates are linked through rigid hydrogen bonding and create cavities (host lattice or cage) that can enclose a large variety of nature gas molecules (guests). The majority of naturally occurring gas hydrates contain methane [*MacDonald*, 1990; *Kvenvolden*, 1993]. Analyses of continental margin hydrates recovered in Deep Sea Drilling Project (DSDP) cores also indicate that the deep sea hydrates are almost entirely methane, with small amounts of carbon dioxide and higher hydrocarbons [e.g., *Mclver*, 1974; *Shipley and Didyk*, 1981; *Kvenvolden and MacDonald*, 1983; *Kvenvolden and MacDonald*, 1985]. Although solid gas hydrate was not recovered during ODP Leg 146 at the Cascadia margin, the -1.4 °C temperature measured in a core ~8 m above the BSR depth at Site 889, and the observed coincidence of very low pore fluid chlorinity and very high headspace methane concentrations near the depth of BSR, strongly imply the presence of gas hydrate in situ with methane as the dominant gas within the hydrate cage [*Kastner et al.*, 1995; *Whiticar et al.*, 1995; *Whiticar and Hovland*, 1995]. The maximum amount of methane that can occur in a methane hydrate depends on the clathrate geometry. In theory, 1 m^3 of fully saturated structure I methane hydrate, in which each cage is arranged in body-centred packing and large enough to include a methane molecule, can contain up to 164 m^3 of methane gas at standard condition [*Kvenvolden*, 1993]. In this sense, gas hydrate is a storage of natural gas in a very condensed state. This fact explains the increasing interest in gas hydrates as a potential of (1) future energy source [e.g., *MacDonald*, 1990a; *Appenzeller*, 1991], (2) submarine geohazard [e.g., *Kvenvolden*, 1993], such as marine landslide caused by hydrate

dissociation due to temperature and/or pressure changes, and (3) factor in global climate change [e.g., *Nisbet*, 1989; *Watson et al.*, 1990; *MacDonald*, 1990b; *Whiticar*, 1990].

Temperature and pressure, sufficient methane concentration, salinity of pore water, and type of gas enclosed, are the main factors which determine either formation or decomposition of solid hydrates. The phase diagram in Figure 3.1 for methane in pure water and in seawater from the *Englezos and Bishnoi* [1988] and *Dickens and Quinby-Hunt* [1994] equation-of-state estimates is shown in comparison with laboratory data and in situ P-T measurements at DSDP/ODP sites. The upper limit of the gas hydrate zone in continental margin sediments is ordinarily the sea floor where water depths exceed 250-300 m. In fact, gas hydrates have been recovered within 6.5 m of the sea floor in sediment from the deeper part of the Black Sea [*Yefremova and Zhizhchenko*, 1975] and off Oregon [E. Suess, pers. comm., 1996]. The lower limit for the hydrate stability zone is a function of geothermal gradient and seafloor temperature and depends on local conditions.

An increase in temperature or a decrease in pressure will migrate the hydrate stability field upwards and destabilize gas hydrates causing them to decompose. The subbottom depth to the base of the stability field is more strongly a function of temperature than of pressure. Two important processes affecting the hydrate stability field in accretionary prism environment are the upward fluid flow and tectonic uplift of the sediment section. On the southern Cascadia margin off Oregon, the BSR representing the base of hydrate stability field has been measured at a subbottom depth of ~70 m where temperature is increased by channelized fluid flow discharge along a major fault [*Davis et al.*, 1995]. Off the Vancouver Island margin, the seawardmost BSR has been recognized at a subbottom depth of ~400 m

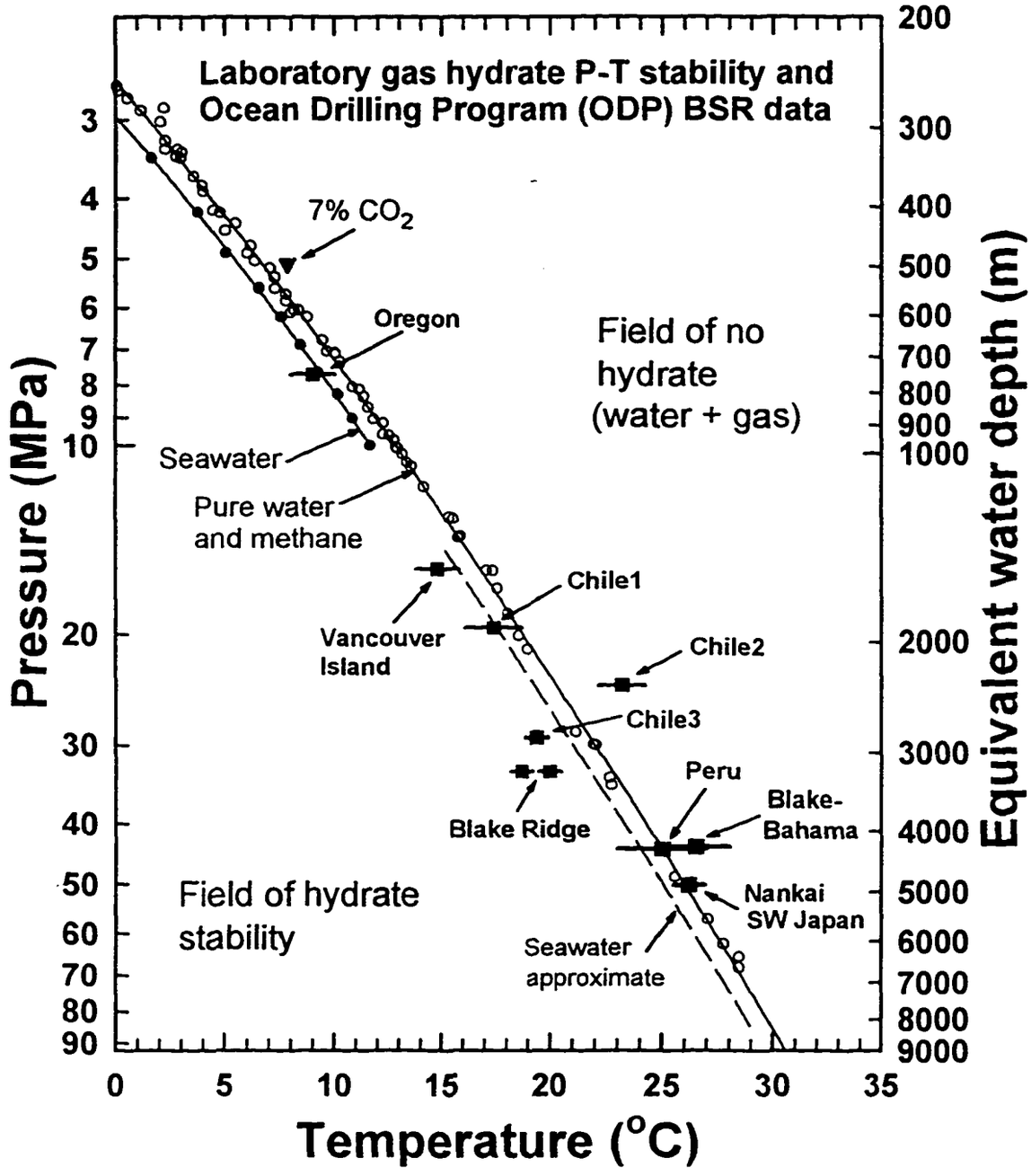

Figure 3.1 The pressure/temperature phase diagram for methane hydrate stability field. The solid line seawater curve is from the equation-of-state computation for artificial seawater by *Englezos and Bishnoi* [1988] and *Dickens and Quinby-Hunt* [1994]. Extensive laboratory data for pure water/methane and limited data on the influence of CO_2 are also illustrated. Estimates of in situ P-T conditions at the base of hydrate stability field measured at DSDP/ODP sites agree well with the laboratory data (from *Hyndman et al.*, 1994).

where water depth is abut 2300 m. The landwardmost BSR on the mid-continental slope occurs at a depth of less than 250 m below the seafloor where water depth is only 1100 m (Figure 3.3). As a consequence of the young age (5-7 Ma) of the subducted oceanic crust, the heat flow is high and the subbottom depth to the BSR at ODP Sites 889/890 on the mid-slope (water depth of 1300 m) is only 224 m (Figure 3.7) and the temperature measured in the drillhole is 14.8 °C [*Westbrook et al.*, 1994], about 2 °C lower than the predicted temperature for the base of a pure H_2O-pure CH_4 hydrate stability field at the corresponding pressure. The measured temperature, however, is within the uncertainties of the base of the stability field of a seawater-CH_4 hydrate [*Kastner et al.*, 1995].

3.1.2 Formation of Gas Hydrates in Accretionary Wedge Sediments

One feature of marine gas hydrates that is not apparent from the phase diagram in Figure 3.1 is the amount of methane that is required for gas hydrate formation. Gas hydrates will form with about 90% of the cages of the clathrate filled [*Sloan*, 1990]. However, methane solubility in seawater is very low, about 0.045 volumes of methane per volume of water at standard conditions [*Yamamoto et al.*, 1976]. Thus the amount of methane necessary for gas hydrates formation greatly exceeds the solubility of methane in water. This requirement for a source of enormous amounts of methane for gas hydrate formation limits the regions where gas hydrates can be expected and found. Because of the temperature-pressure and methane volume requirements, marine gas hydrates are generally restricted to two regions: continental slopes and rises of active and passive continental margins, and on continental shelves of polar regions associated with relic permafrost [*Kvenvolden*, 1988a,

1988b; *Kvenvolden et al.*, 1993]. The detailed compilation of gas hydrate occurrences by *Kvenvolden et al.* [1993] has identified 47 locations worldwide where marine gas hydrates are known or inferred to be present. The evidence for gas hydrates at these location is provided by geophysical data (appearance of a BSR), DSDP/ODP core sampling, drillhole geochemical measurements (low chloride pore fluids, high methane concentration and degassing), and geologic investigations (submarine slides and slumps). The majority of the marine gas hydrate occurrences worldwide are in the upper few hundred meters of ocean floor sediments on continental margins and are especially common in subduction zone accretionary prisms where upward fluid expulsion through thick clastic sedimentary sequences is known to occur [e.g., *Shipley and Didyk*, 1981; *Minshull and White*, 1989; *Miller et al.*, 1991; *Hyndman and Davis*, 1992; *Hyndman and Spence*, 1992; *Katzman et al.*, 1994; *Andreassen et al.*, 1995].

Two basic models have been proposed for the formation of gas hydrates in continental margin sedimentary sections. The first one, in situ formation model, suggests that the methane is generated bacterially from organic compounds in the sediments at the depths where the hydrates occur. This model requires that methane concentration be in excess of pore fluid saturation and large amount of free gas be present below the zone of hydrate stability. *Paull et al.* [1994] estimated the maximum amount of hydrate produced through in situ microbial gas production under ideal conditions, i.e., total organic carbon concentration exceeds 1% of sediment dry weight and half of the organic carbon is available to microorganism. In a passive margin of the Black Ridge area, ~6% of the pore space could be filled by the hydrate produced locally with the available organic carbon [Paull et., 1994].

The above calculation suggests that there could be a large amount of organic carbon available for in situ hydrate production, however, there are unanswered questions with this model: (1) neither the original amount nor the quality of sedimentary organic carbon can actually be determined for buried sediment, (2) large quantities of methane that hydrates contain may not be produced locally from common concentration of organic carbon in a closed system (i.e., no gas migration), (2) free gas over a large depth range below the hydrate stability zone, in an equivalent amount of methane to the hydrate concentration above the stability zone, is not detected seismically or measured in drillholes, and (3) hydrates and corresponding BSRs are not seen in normal marine sediment settings where methane production is expected but no mechanism of methane concentration or migration exists.

The second formation model, the fluid expulsion model proposed by *Hyndman and Davis* [1992] and *Paull et al.* [1994], involves methane migration into the hydrate stability zone by upward fluid flow originated at greater depth (Figure 3.2). In this model, most of the methane is generated biogenically below the level of hydrate stability field. Upward fluid expulsion, which is resulted from tectonic thickening and sediment loading and is common in subduction zone accretionary prisms and in areas where rapid sediment deposition results in initial underconsolidation but generally not elsewhere, provides a mechanism to remove methane or free gas from the rising pore fluid. As the methane-rich, but probably unsaturated, fluids pass into the hydrate stability field, the hydrate zone builds upward from the base of the stability, thus forming a sharp base and a gradational top. This model satisfactorily explains the source of large amount of methane required to form hydrate which appears to be concentrated in a layer at the base of the stability field. Free gas below the stability is neither

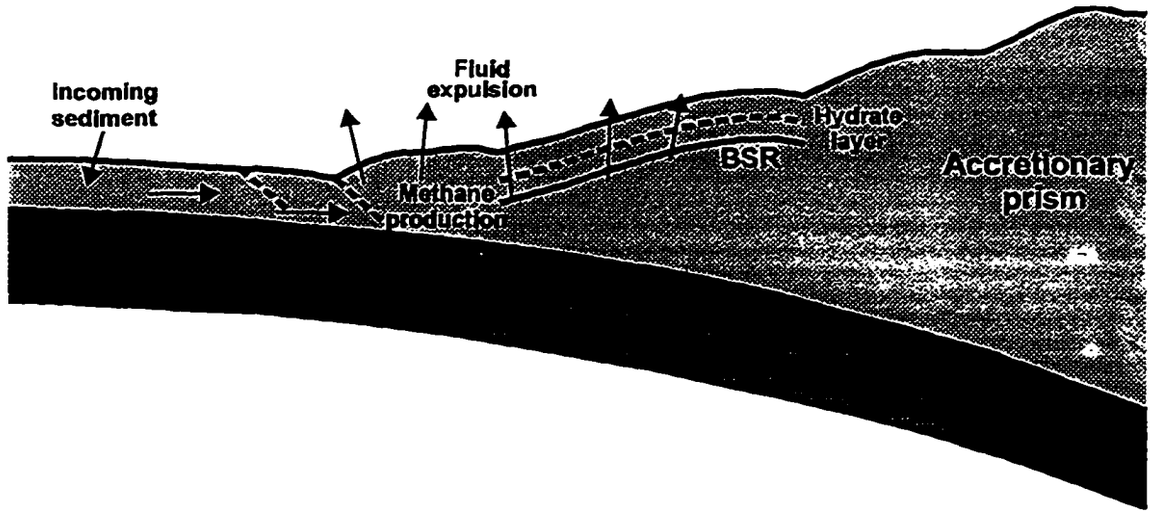

Figure 3.2 Illustration of the fluid expulsion model of hydrate BSR formation through methane removal from rising fluids that are tectonically expelled from an accretionary prism (modified from *Hyndman and Davis* [1992]).

specifically required nor excluded in this model. The most unconstrained aspect of the model is the efficiency with which methane is removed and hydrate formed as pore fluids pass into the hydrate stability field. Figure 3.2 illustrates the methane production and hydrate formation processes in an accretionary prism where upward fluid expulsion carries dissolved methane into the stability field. In the normal depositional regime seaward of the deformation front, there is no upward fluid flow into the hydrate stability field [*Hyndman and Davis*, 1992]. The maximum fluid expulsion takes place near the deformation front from the discussion above in the case of northern Cascadia accretionary prism [*Yuan et al.*, 1994], and the methane hydrate formation is expected to occur near the deformation front and the BSR to appear landward of the deformation front.

Other mechanisms in the accretionary prism environments affecting hydrate

concentration near the base of the stability field include temperature change through tectonic processes and pressure change from sediment deposition and tectonic uplift. An increase in temperature or a decrease in pressure will cause the base of hydrate stability field to move upwards through the sediment section. Free gas will initially be formed as the hydrate dissociates when being moved out of the stability field. This gas will then migrate upward and be reintroduced to the hydrate form and be thus concentrated near the base of the hydrate stability. Sediment deposition on accretionary prism is normally small and temperature changes in the accretionary sediments can be quite substantial, but the pressure changes will have a significant effect on migrating the stability field if uplift or sediment thickening rate is very high.

3.1.3 Effect of Methane Hydrate Formation on Sediment Velocity

The most readily observable change in sediment physical properties resulting from the formation of gas hydrate is an increase in seismic velocity. A generally accepted value for pure methane hydrate is 3730 m/s [*Pearson et al.*, 1983; *Sloan*, 1990], which is much higher than the velocities of 1600-1700 m/s for the unconsolidated and hydrate-free sediment at subbottom depths of a few hundred meters. The distribution of hydrate in the sediment is not well known. The simplest model is for the water in the sediment pore spaces to be partially replaced by evenly dispersed high-velocity gas hydrate "ice" that cements the sediment matrix. The recovered ODP drill cores at Sites 889/890 suggest that the hydrate is generally disseminated. Massive hydrate has been recovered in DSDP/ODP drill cores [e.g. *Mathews and von Huene*, 1985] but it is probably rare [*ODP Leg 164 Shipboard Scientific Party*,

personal communication, 1996]. Unless pervasive and horizontally layered, such massive hydrate should not produce a BSR. There are few laboratory determinations of seismic velocities for porous media saturated with gas hydrate and they are for sediments of much lower porosity and higher velocity than most continental slope sediments. Measured P-wave velocities at the maximum hydrate saturation vary from 2700 to 6000 m/s depending on the method of preparation and the type of hydrate [e.g., *Stoll et al.*, 1971; *Stoll*, 1974; *Pearson et al.*, 1986]. As will be discussed below, if hydrate occupies 15% of pore space, about 10% increase of sediment velocity is expected.

A small quantity, 1-2%, of free gas in the pore space of sediment has a significant effect in reducing sediment P-wave velocity, while further increases in gas saturation causes little change [*Domenico*, 1976; *Gregory*, 1976; *Murphy*, 1984]. Therefore, the combination of hydrate above the BSR and free gas below can result in a dramatic impedance contrast which produces a seismically detectable BSR.

3.2 Seismic Observations of Gas Hydrate Bottom-Simulation Reflectors

The coarse-clastic accretionary wedge on the northern Cascadia margin and widespread BSRs within the wedge sediment beneath the continental slope are well imaged by the 1989 multichannel data [*Spence et al.*, 1991a, 1991b; *Hyndman et al.*, 1994]. Immediately landward of the deformation front, where the sediment section starts to undergo intense tectonic compaction and thickening and sediment fluid expulsion rate has reached its maximum, development of a prominent BSR commences in the deformed sediment (Figure 3.3). The readily recognizable seawardmost BSR on L89-08 is near CDP 4600 where

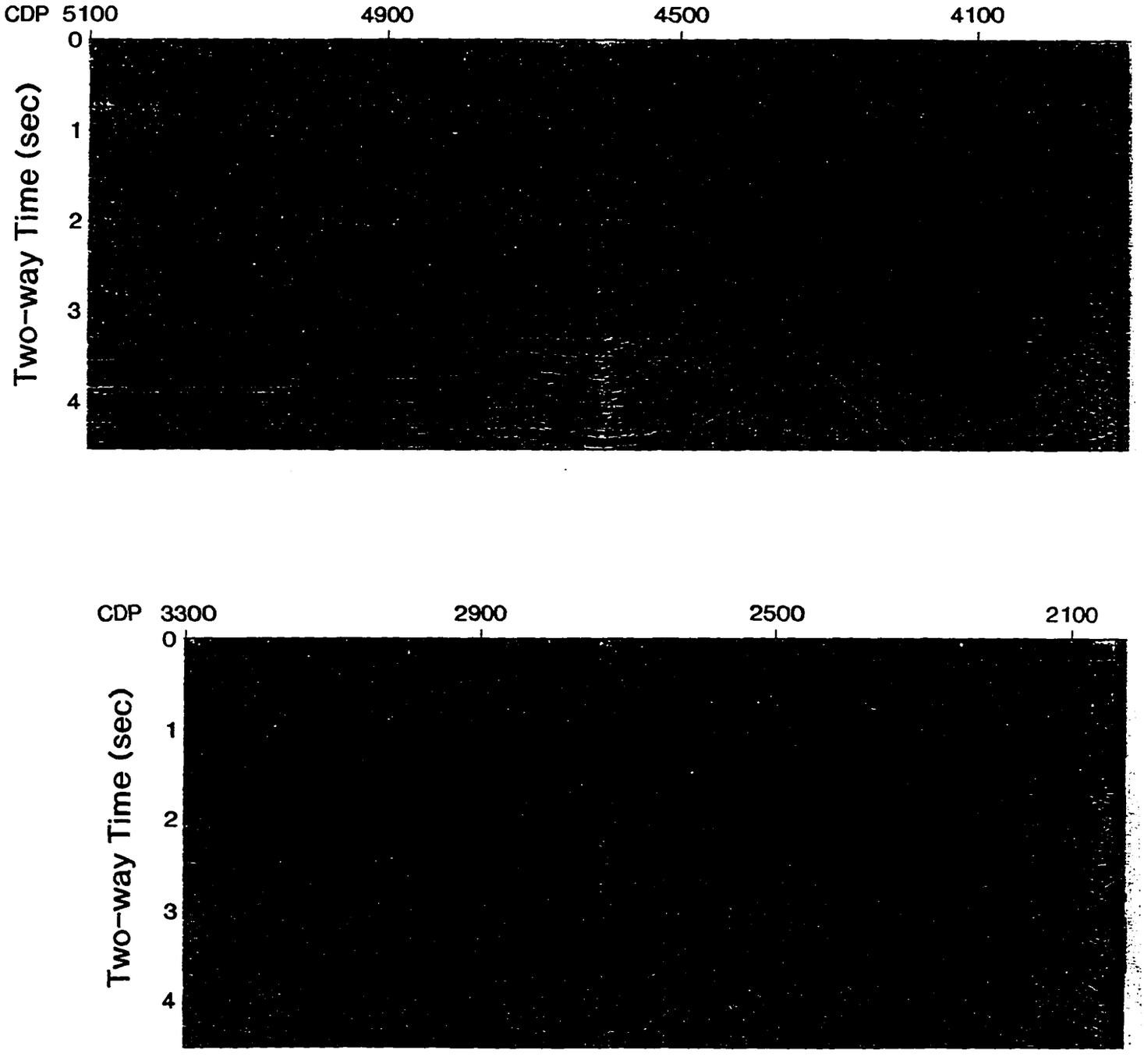

Figure 3.3 Re-processed L89-08 migration from Cascadia basin to the mid
where there is a strong hydrate-bottom simulating reflect

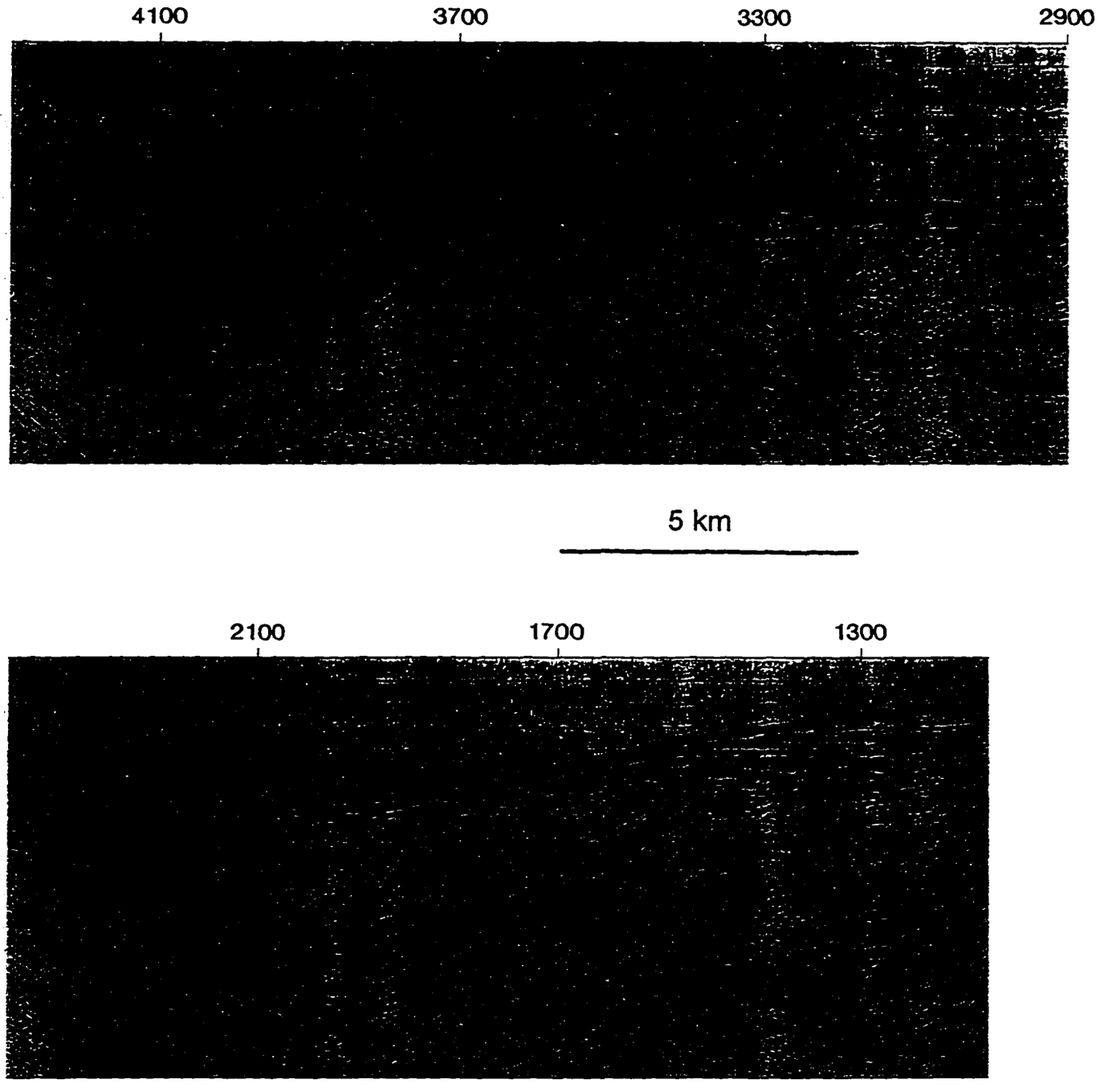

rom Cascadia basin to the mid-slope of the northern Cascadia accretionary prism
rate-bottom simulating reflector (BSR) over much of the slope region.

sediment stratigraphy starts to be disturbed tectonically. The BSR may develop seaward of the deformation front where the largest amount of pore fluid is expelled as inferred from a dramatic velocity increase. However, the strong seafloor-parallel reflectors of the turbidite sequences would make the BSR undistinguishable. During the initial stage of the BSR development, the concentration of methane hydrate is probably low and therefore no clear BSR can be detected. Farther landward in the deformed frontal ridge between CDP 4200 and 4600, the image of the BSR is dimmed by the steep seafloor topography especially on the landward side of the ridge flank. Landward of CDP 4200, the strong BSR can be followed continuously across much of the entire lower-mid slope to CDP 2000, a lateral distance of more than 32 km.

Figure 3.4 shows portions of the two orthogonal reflection lines L89-08 and L89-10 where the BSR is continuous and particularly strong in the thickening slope sediment section. L89-08 is perpendicular to the continental margin and directly across ODP Sites 889/890 (Figure 2.1). L89-10 passes about 1.5 km southwest of the drill sites. On these lines the strong BSR is imaged subparallel to the seafloor at 250-275 ms below the seabed on much of the lower continental slope. Between CDP 2900 and 3000 on L89-08 (Figure 3.4a), there are new slope deposits and sufficient hydrate and gas may not have formed for a clear BSR. Any BSR is indistinguishable from seafloor-subparallel reflections of the undeformed sediments. An anticlinal stratigraphic feature on L89-10 (CDP 2050-2200) probably provides conditions for free gas migration into a local trap which thus produces a strong BSR. On these lines, there are strong and abundant reflections above the BSR and therefore no blanking effect as seen in the Blake Ridge area of the southeastern U.S. margin [*Shipley et*

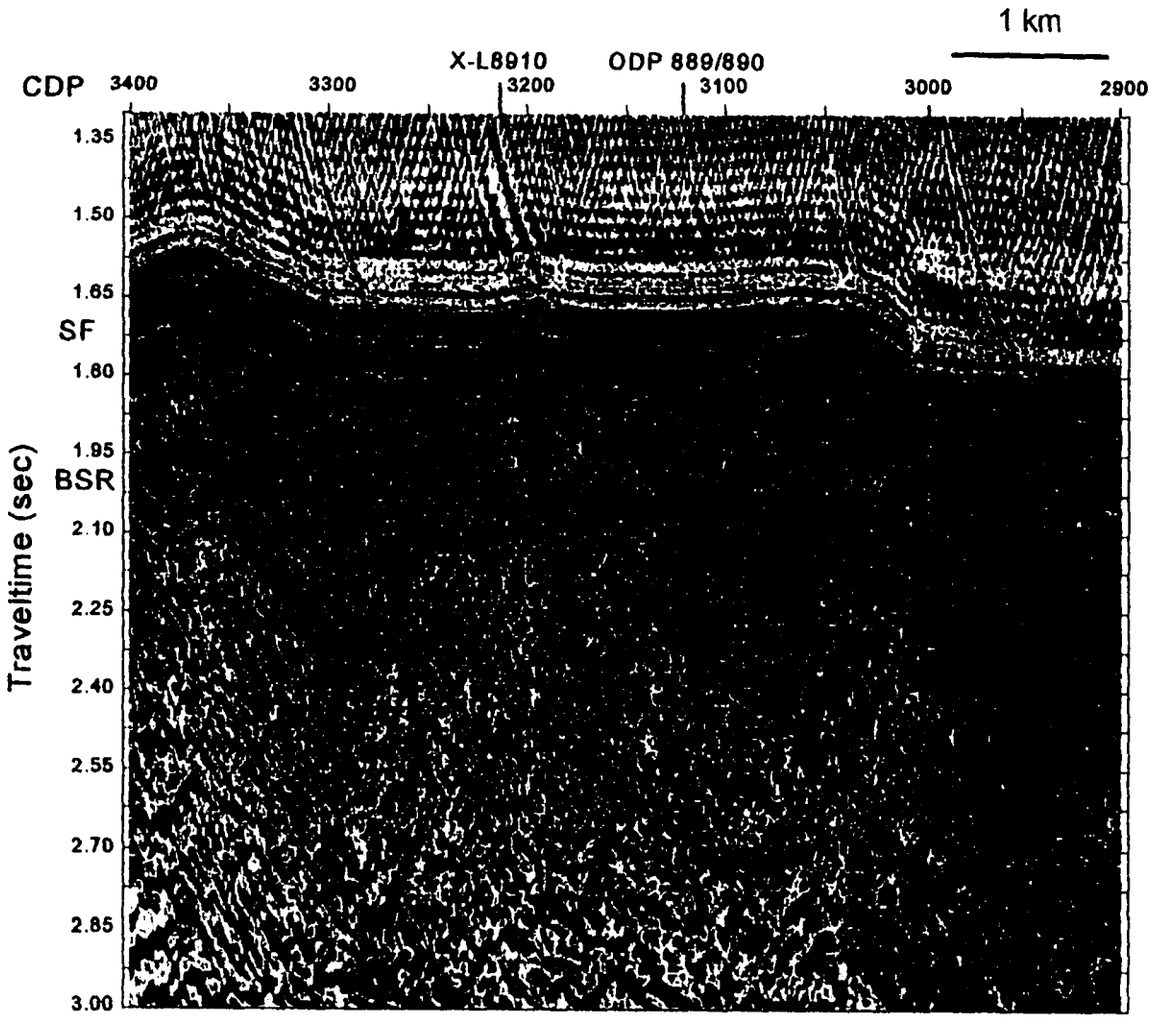

(a)

Figure 3.4 Reflection seismic sections, L89-08 (a) and L89-10 (b), near ODP Site 889 on the lower slope region where the BSR is particularly strong. The basic data processing included wavelet designator, spherical divergence correction, and finite difference migration.

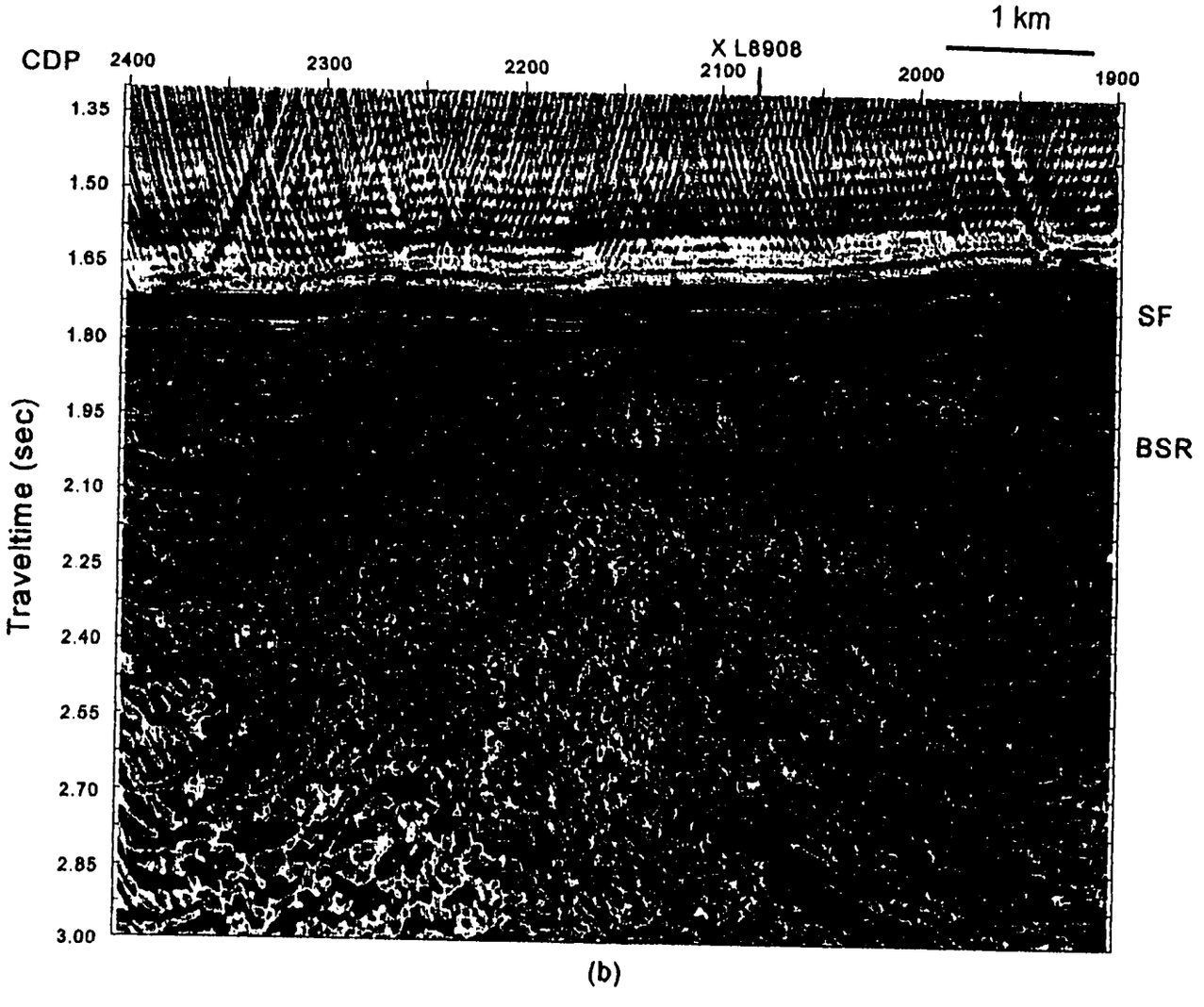

Figure 3.4 Continued.

al., 1979; *Dillon et al.*, 1983] exists in the northern Cascadia accretionary sediments.

3.3 BSR Reflection Characteristics and Reflection Coefficients

The BSR reflection is generally a single symmetrical wavelet with a reversed polarity relative to the seafloor reflection, indicating a sharp and negative impedance contrast downward across the BSR. At the higher frequencies (60-90 Hz and 150-200 Hz) of the 1993 single-channel seismic survey with small air guns of 1.97 L (120 inch^3) and 0.65 L (40

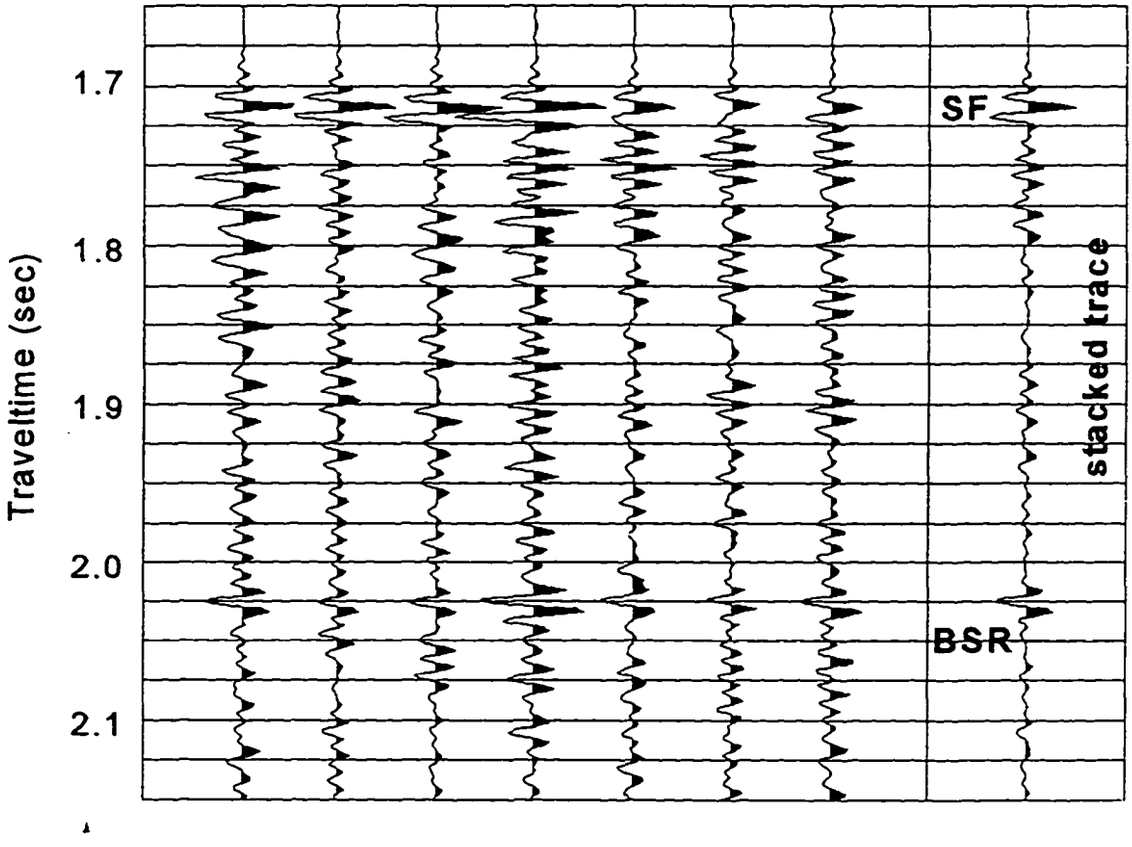

Figure 3.5 Single-channel traces from a 120-inch^3 air gun recorded near ODP Site 889 [*Spence et al.*, 1995]. The trace on the right is a stack of the seven traces shown to the left. The strong BSR beneath the flank of a ridge-formed anticlinal uplift is a single pulse at 2.025 s with a reversed polarity relative to the seafloor reflection (SF).

inch^3) near Sites 889/890 [*Spence et al.*, 1995], no reflections from the top of a hydrate layer or bottom of a gas layer have been identified (Figure 3.5). It has thus been inferred that the top of the hydrate accumulation and the base of the low-velocity free gas layer beneath the BSR must be gradational [e.g., *Spence et al.*, 1995; *Fink*, 1995].

Following *Warner* [1990], the seafloor reflection coefficient has been obtained from the relative amplitudes of the seafloor primary and multiple reflections measured from pre-stack data (Figure 3.6). The BSR reflection coefficient has also been estimated by comparing the BSR amplitudes, corrected for the transmission loss through the seafloor, with that of the seafloor. As the multiples are reflected at different seafloor locations to the primary reflections, the reflection amplitude ratios are averaged over the entire analyzed section. This minimizes the effect of amplitude variations due to varying seafloor conditions and scattering patterns. The seafloor reflection coefficients from L89-10 are estimated as 0.18-0.24. The BSR amplitudes are about 30% of that of the seafloor, and the BSR reflection coefficients are 0.06-0.08. Much higher BSR reflection coefficients, up to 0.15, are found along L89-08. From an analysis of a fine-grid single-channel seismic survey near Sites 889/890, *Spence et al.* [1995] showed much higher BSR reflection coefficients beneath a topographic high formed by an anticlinal uplift. As hydrate density is very close to that of pore water and the amount of free gas below the BSR is assumed to be very small, sediment density is changed very little by the presence of either hydrate or gas across the BSR depth. A velocity decrease of 300-400 m/s is therefore required to produce the impedance contrast representing a BSR reflection coefficient of 0.1. This velocity change could come from (1) high-velocity hydrate filling sediment pore space or binding sediment grains above the BSR and sediment with

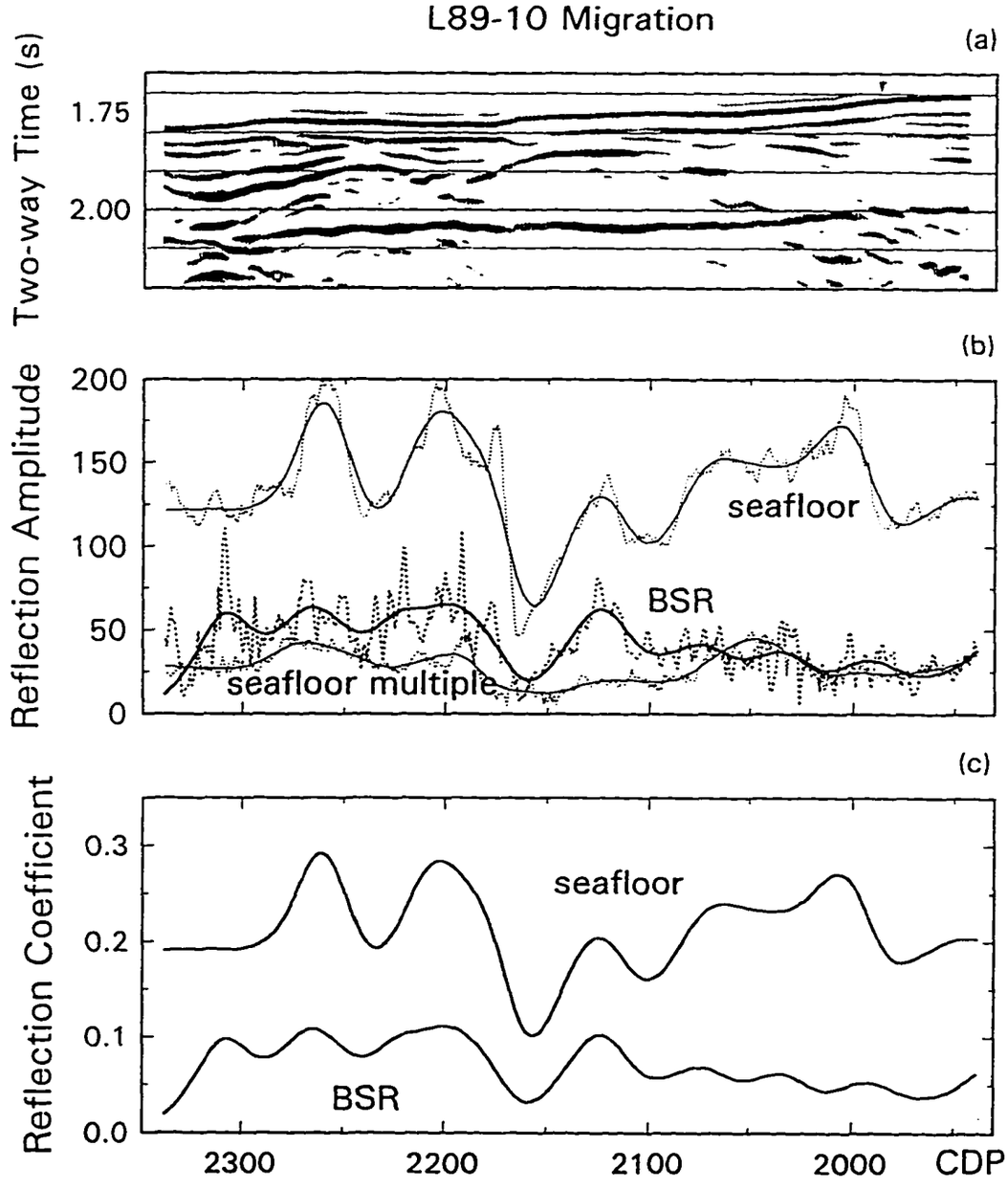

Figure 3.6 (a) A portion of L89-10 migration (4 km) near ODP Site 889. (b) Reflection amplitudes from seafloor primary, first multiple, and the BSR reflections from L89-10 shown in Figure 3.6a. The amplitudes were averaged over three near-offset traces in CDP gathers, and the amplitudes from multiples were measured at farther offsets to eliminate any amplitude variations caused by varying incidence angles. The dashed lines are actual amplitudes measurements, and the solid lines are the smoothed values. (c) The seafloor and BSR reflection coefficients estimated from reflection amplitudes in Figure 3.6b.

normal pore water content containing little or no free gas below [*Hyndman and Spence*, 1992], (2) sediment with little hydrate above and considerable free gas concentration below the BSR [*Singh et al.*, 1993; *Minshull et al.*, 1994; *MacKay et al.*, 1994], or some combination of 1 and 2.

As an attempt to derive limits on the BSR reflection coefficients and thus the velocity contrasts across the interface at the BSR, the observed amplitude ratios between the BSR and the seafloor reflections were measured from L89-08 near the ODP drillsites (Figure 3.7). Assuming that the seafloor reflection coefficient R_{sf} is known and considering the transmission loss at the seafloor, the reflection coefficient at the BSR is $AR_{sf}/(1-R_{sf}^2)$, where A is the amplitude ratio between BSR and seafloor reflections. The calculated BSR reflection coefficients for assumed seafloor reflection coefficients of 0.15, 0.20, and 0.25 are shown in Figure 3.7a. From CDP 3100 to 3200 in the vicinity of the ODP sites where the BSR reflection is strong, the BSR reflection coefficients range from 0.06 to 0.12 if the seafloor reflection coefficient is taken to be 0.20. To place constraints on velocities above and below the BSR that are compatible with the derived reflection coefficients, the sub-BSR velocity can be inferred by a range of assumed values for the velocities above the BSR. Figure 3.7b summarizes the calculation for the velocities below the BSR assuming a constant seafloor reflection coefficient of 0.2. Velocities less than 1600 m/s are found below the BSR for assumed velocity above the BSR of 1800 m/s as obtained from borehole data. Such low velocities, atypical for sediments at several hundred metres below seafloor, may imply the presence of free gas below the BSR. However, if the velocity above the BSR is higher than from borehole data, e.g., 2000 m/s, free gas may not be required to produce the reflection

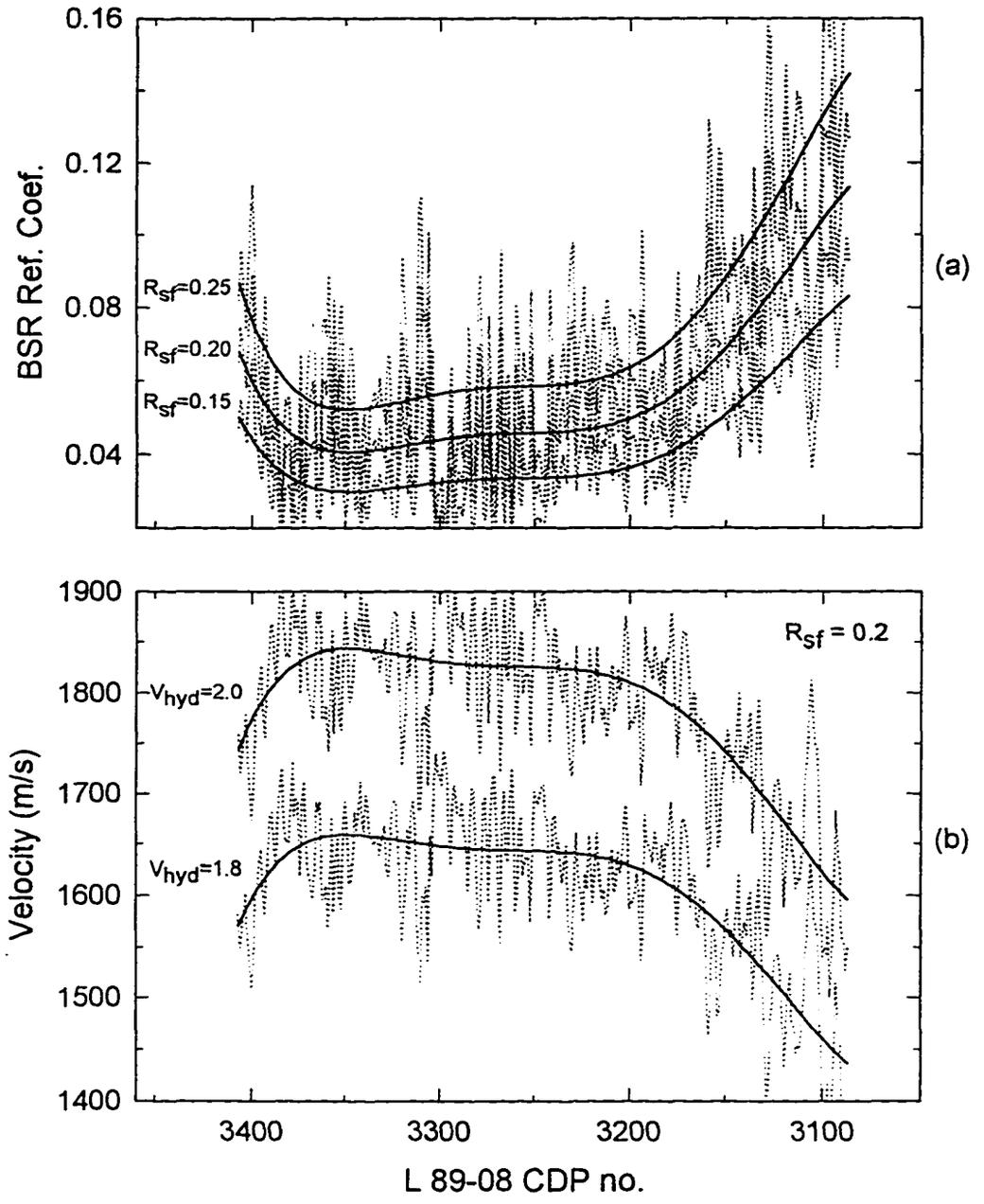

Figure 3.7 (a) Reflection coefficient at the BSR derived from the amplitude ratios of the BSR and seafloor reflections corrected for geometrical spreading, assuming several possible values for the seafloor reflection coefficients. (b) velocity beneath the BSR derived from the reflection coefficients, assuming a seafloor reflection coefficient of 0.2 and sediment velocities above the BSR of 1800 and 2000 m/s. For these estimates, no density changes are considered at the BSR depth. Solid lines in the figures are the smooth averages of the actual measured data in dotted lines.

amplitudes at the BSR. It should be recognized that the reflection coefficient and velocity estimates may be underestimated because the factors of attenuation and scattering at a rough surface, are not considered in the above calculations. In conclusion, the large amplitudes of the BSR observed in the northern Cascadia margin are consistent with the presence of methane, either or both in the form of gas hydrate and free gas in the accretionary prism sediments.

3.4 Velocity Data near of ODP Sites 889/890

At ODP Site 889 (Figure 3.8), sediment cores were recovered at intervals from 20 to 345.8 meters below seafloor (mbsf) at Hole 889A and from 197 to 386.5 mbsf at Hole 889B [*Westbrook et al.*, 1994]. The sediment section is divided into two major units. The upper unit from 0 to 128 mbsf consists of clayey silt to silty clay interbedded with silt and fine sand layers of turbiditic origin and exhibits little deformation. This unit is interpreted to have its origin as slope basin sediments that were deposited approximately in their present location. The sediments of the lower unit are more indurated, through compaction and slight cementation. They are interpreted as accreted Cascadia Basin sediments. Studies on the Cascadia Basin ODP data [e.g., *Davis at al.*, 1992; *Westbrook et al.*, 1994] have suggested that the bulk sediment composition and average grain size (averaged over turbidite layering) do not vary significantly over the upper part of the basin sediment section.

Downhole velocity measurements in ODP Sites 889A and 889B provide the first high-quality in situ velocity data extending through a BSR. At Site 889, Schlumberger logging tools, long-spaced sonic (LSS) and well-seismic tool (WST), were used to obtain sonic and

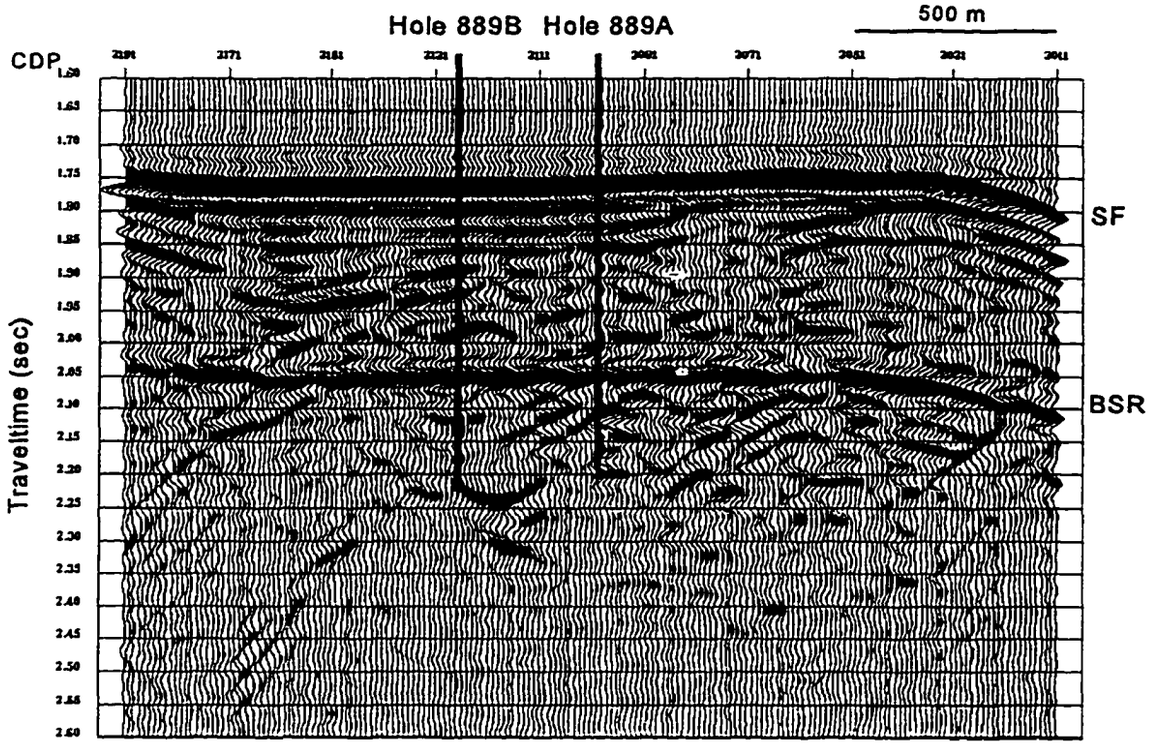

Figure 3.8 Detail of migrated time section from L89-08 in the immediate vicinity of Site 889. Holes 889A and 889B penetrated a small slope basin and accreted sediment to depths of 345.8 and 386.5 meters below seafloor (mbsf), respectively. The logged interval, however, extends only 30 m below the BSR which occurs at 224 mbsf.

vertical seismic profile (VSP) measurements of the formation velocities to a depth of 250 mbsf [*Westbrook et al.*, 1994; *MacKay et al.*, 1994]. The downhole data are compared in this study with detailed MCS velocities from a 10-km-long section of L89-10 centred near the ODP sites.

3.4.1 Sonic Velocity Logging

The sonic logging data were recorded with an LSS tool that used two acoustic transmitters and two receivers to give source-receiver distances of 2.4, 3.0, and 3.6 m. Sonic

log data at Sites 889A and 889B extend from 70.5 to 260.1 mbsf and from 61.7 to 259 mbsf, respectively [*Westbrook et al.*, 1994]. There are large variations in velocity of ± 50 m/s over depth intervals of a few meters associated with the grain size changes in the turbidite section. The layered velocity contrasts may also be enhanced by the high-velocity hydrate being concentrated in the low porosity and high permeability sandier layers. Within the upper 100-120 m of the slope sediments, sonic data show velocities below 1600 m/s, appropriate for recent slope sediment deposits (Figure 3.9). In the 100-m interval above the BSR, the sonic logs recorded average formation velocities of 1800 m/s. The sonic velocities are believed to be a minimum as the hydrate adjacent to the hole might have been partially dissociated or washed out during the drilling. As discussed below, this velocity is well above the no-hydrate reference. The high velocity is interpreted to be the result of velocity enhancement due to hydrate. Just below the BSR, the sonic data exhibit first the values are very different for the two holes and second velocities are not as low as expected for free gas. The minimum velocity value for Hole 889A is 1630 m/s at 231 mbsf. On the basis of the velocities of ~1500 m/s below the BSR from VSP data discussed below, it is concluded that drill fluid invasion displaced much of the free gas into the formation beyond the penetration depth of the sonic logs.

3.4.2 VSP Velocity Measurements

The VSP at Site 889 was run from 243 mbsf, 19 m below the BSR, to 125.5 mbsf. Surface shots fired alternately from a 4.9 L (300 inch^3) air gun and a 6.5 L (400 inch^3) water gun were recorded in the borehole by a single vertical-component geophone. Most receiver

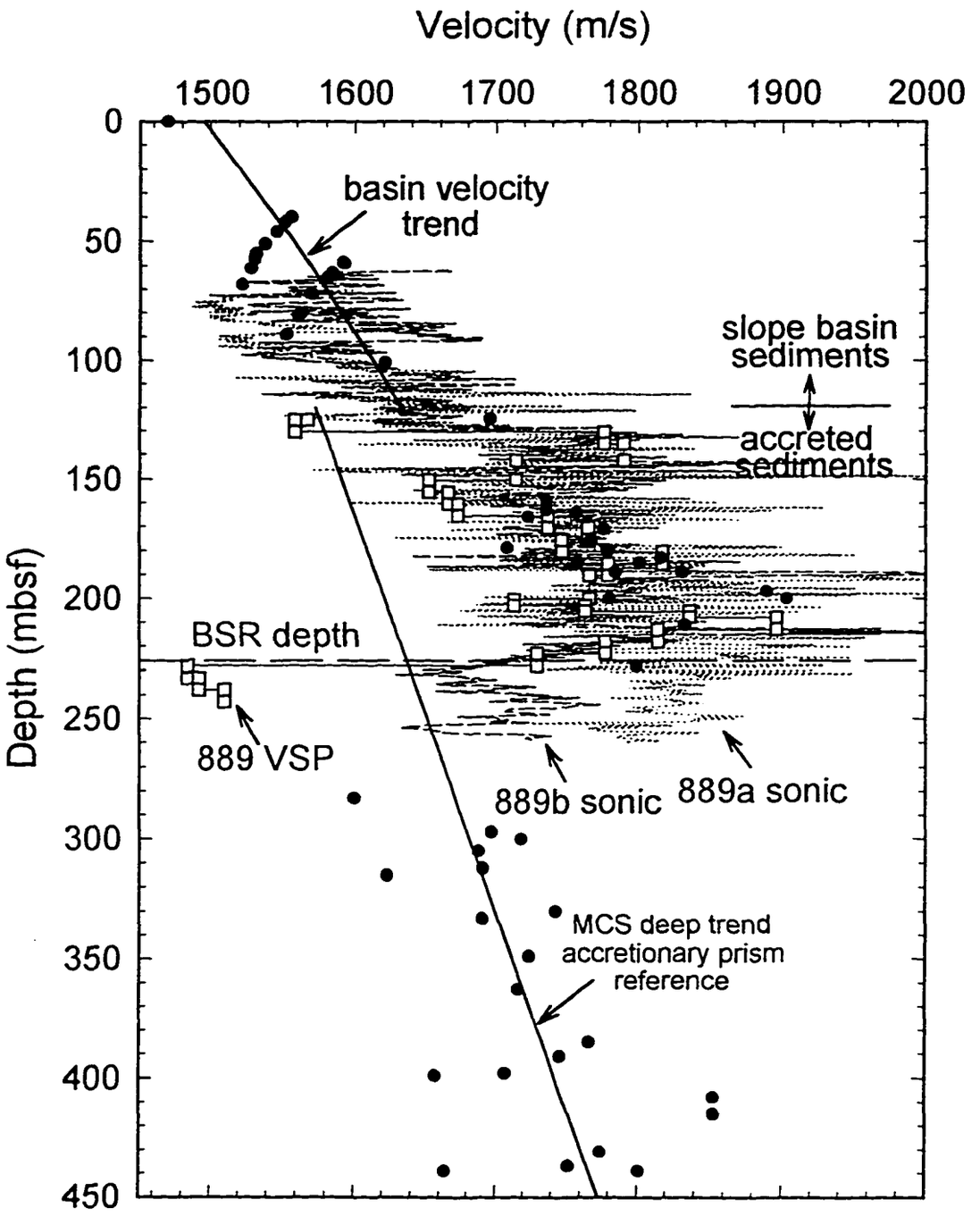

Figure 3.9 Sonic logging (light dotted wiggle lines) and vertical seismic profile (VSP) data for Site 889 (open squares) are shown in comparison with the multichannel seismic (MCS) velocities taken from L89-10 (solid circles). Above the BSR, MCS velocities are in excellent agreement with the in situ measurements. The solid line fitting the velocities represents the reference velocity-depth profile in the slope basin and accreted sediments.

stations were spaced at 5-m intervals [*MacKay et al.*, 1994]. From 130 mbsf to the BSR at 224 mbsf, the VSP velocities range from about 1700 to 1900 m/s (Figure 3.9). The average velocity in this interval, about 1800 m/s, agrees very well with the average of the sonic logs. Below the BSR, the VSP velocity drops sharply to 1520 m/s in an interval of 15 m. The BSR thus clearly represents a strong discontinuity in the VSP velocity data. *MacKay et al.* [1994] suggested that there was only a small velocity enhancement from the presence of hydrate above the BSR and concluded that the low velocity below the BSR is a strong indication of free gas. As neither low density nor high electrical resistivity is associated with the low velocity beneath the BSR, the concentration of free gas must be very low. However, less than a few percent of free gas is sufficient to produce the velocity drop and thus a strong BSR. This is in agreement with the previous results of AVO analyses which required that there be less than a few percent of free gas [*Hyndman and Spence*, 1992].

3.4.3 Multichannel Seismic Velocity Analyses

The 1989 MCS data were collected using a 3700-m-long hydrophone array that is 3 times the water depth in the study area of the ODP drill sites. As discussed above, this large recording aperture allows unusually high resolution of velocity variations. Two velocity studies were carried out employing conventional semblance analyses. The first discussed in the previous chapter was to define regional variations in velocity-depth profiles at locations extending from the deep abyssal basin to the middle continental slope [*Yuan et al.*, 1994]. In the second, detailed MCS velocities were obtained along L89-08 and near ODP Sites 889/890 for comparison with the drill hole logging and VSP data [*Yuan et al.*, 1996].

Figure 3.10 shows a cross-section of semblance-derived interval velocities from analyses of every 1 km along L89-08 where the BSR is visible. The velocities generally increase with depth with the exception of a high-velocity zone in the ~100 m interval above the BSR over almost the entire range where the BSR is present. The velocities of the continental slope sediments in the study area, excluding those above the BSR depth, are well constrained and increase smoothly with depth to a subbottom depth of at least 3000 mbsf (Figure 3.11, also see Figure 2.12). In the interval from the seafloor to the BSR depth, the agreement between MCS velocities and the ODP downhole measurements is excellent (Figure 3.9). Within the upper portion of the drilled slope deposit, the MCS velocities increase with depth to ~1650 m/s at a subbottom depth of 120-140 mbsf. Downward to the BSR depth, velocities from three different sources of varying resolutions all increase rapidly, reaching a maximum of 1900 m/s immediately above the BSR. The average velocity above the BSR is about 1800 m/s, a value otherwise only observed at a comparable subbottom depth near the deformation front and within the trust fault zone where sediments have undergone intense tectonic compaction. The MCS velocities below the BSR are lower, but not as low as the VSP velocities of less than 1500 m/s. It should be noted that the MCS interval velocity has a vertical resolution of ~100 m, so that any individual velocity value obtained represents an average velocity within at least 100 m in thickness. If free gas exists below the BSR but the thickness of gas layer is thin, the MCS velocity will probably fail to detect it. The seismically detectable high velocity above the BSR, conversely, suggests that the hydrate bearing layer must be at least 100 m or more in thickness.

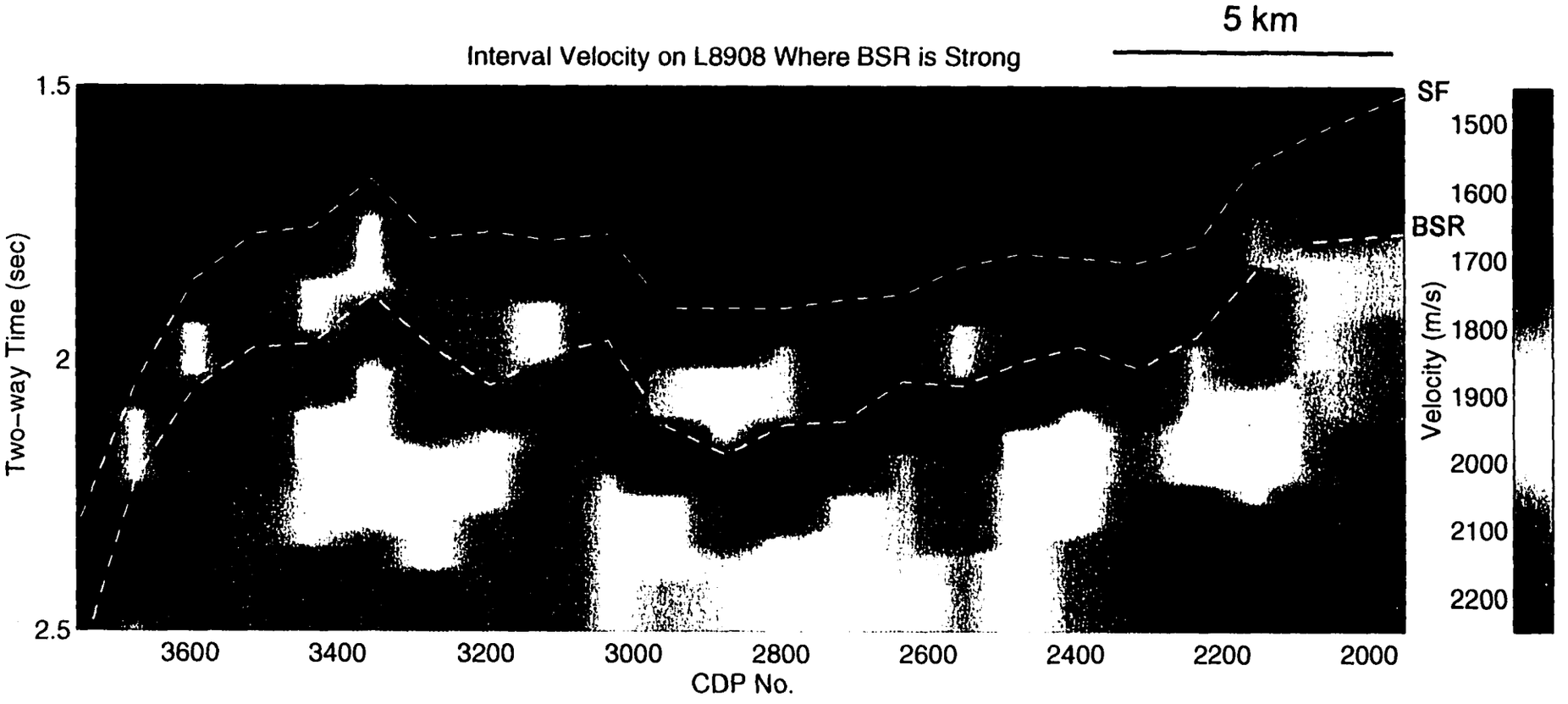

Figure 3.10 Contour plot of semblance-derived interval velocities along L89-08. velocity analyses were made at 1 km interval.

3.5 Reference Velocity of the Slope Sediments

The critical factor required to determine the velocity enhancement due to hydrate and hence the hydrate concentration is a reference velocity-depth profile for sediments containing no hydrate and no gas. The interval with logs and VSP extended only 36 m and 19 m, respectively, beneath the BSR at the ODP sites. The logging data provide good quality velocity measurements above the BSR but did not penetrate deep enough to provide a background velocity unaffected by the presence of either hydrate or free gas. There are also no useful core velocity measurements from ODP Sites 889/890 because of core disturbance. Therefore the only velocity information from below the BSR and the gas layer is provided by the MCS semblance velocity analysis. ODP logging data unaffected by the presence of hydrate has also been analyzed to constrain the reference velocity profile.

3.5.1 Reference Velocity From MCS Data

In the previous discussion, interval velocity-depth functions were determined from Cascadia Basin seaward of the deformation front to the lower-middle slope region where the accretionary prism has approximately doubled in thickness [*Yuan et al.*, 1994]. Both velocity functions obtained in a regional scale and near the ODP drillsites have been used in defining a reference velocity profile in the area of ODP Sites 889/890 where a clear BSR is observed.

At ODP Sites 889/890, the upper 120 m of the holes penetrated slope basin sediments [*Westbrook et al.*, 1994]. Although not an ideal reference, the well-defined, deep-sea Cascadia Basin velocity-depth profile is the best no-hydrate reference for this section (Figure 2.12 and 3.9). Below 120 mbsf the ODP holes penetrated deformed and fractured sediments

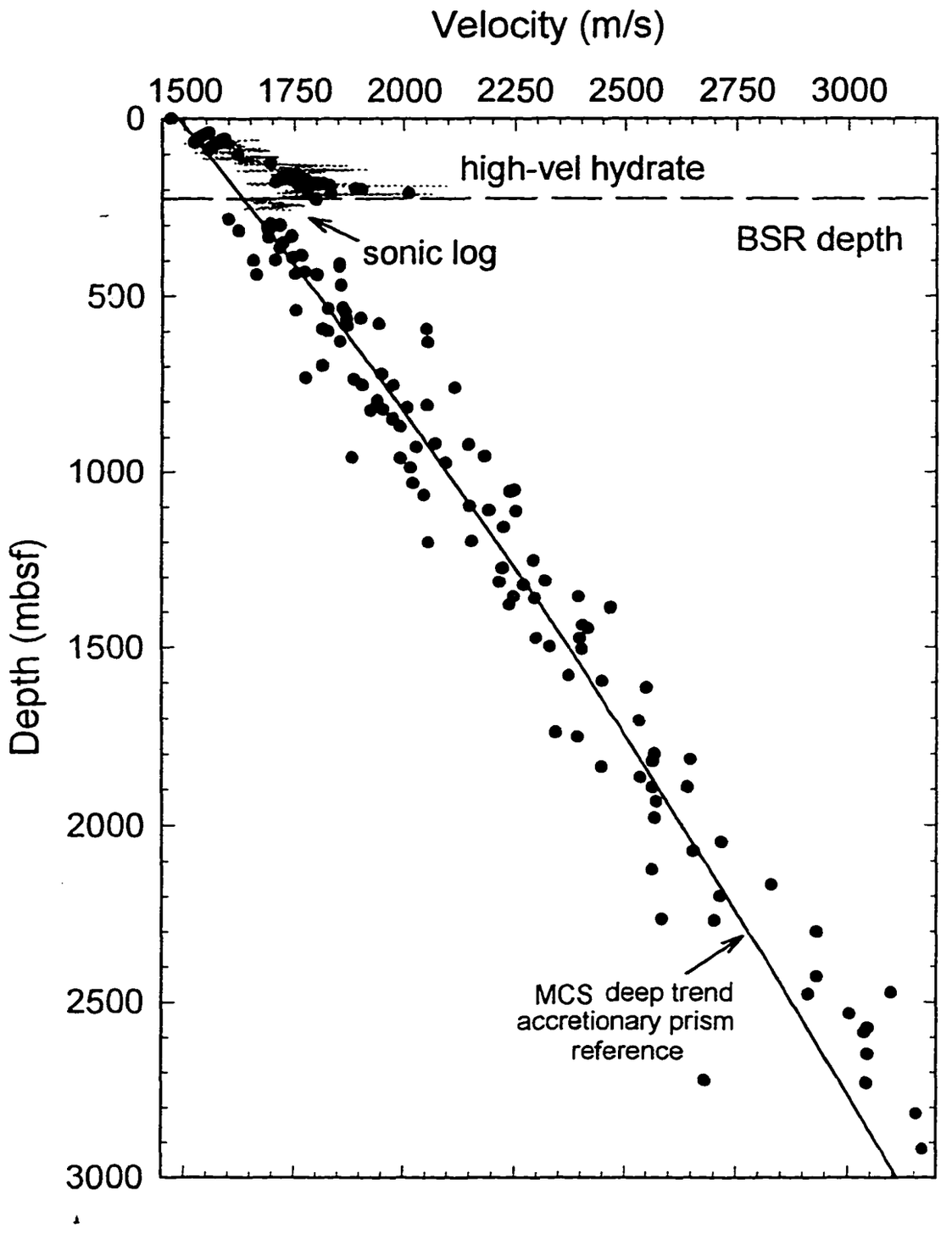

Figure 3.11 L89-10 MCS velocities for a 10 km section over ODP Sites 889/890 and the downhole sonic log at the drill site. The high-velocity hydrate layer is evident to the smoothly increasing velocity with depth down to great subbottom depth.

of the accretionary sediment prism. Upward extrapolation of the MCS velocities from greater depths below the BSR provides the best reference for the sediments below 120 mbsf and above the BSR (Figure 3.9 and 3.11), as the sediment section in this area is quite uniform in composition at a seismic wavelength scale [*Westbrook et al.*, 1994]. This reference velocity-depth profile for the slope sediments has been obtained, excluding the MCS data between 100 and 250 mbsf, using a third-order polynomial fit,

$$V = 1500 + 0.605z - 3.21 \times 10^{-7} z^2 + 7.84 \times 10^{-9} z^3. \quad (3.1)$$

A very similar reference is obtained by interpolation between velocities below the BSR and the near-surface velocities where there is inferred to be little hydrate. The reference velocity at the BSR depth is ~1650 m/s with a statistical uncertainty of about ±50 m/s (Figure 3.11). It should be pointed out that (1) the velocity-depth trend at the lower slope region shows little variations over a wide area even at great depths [*Yuan et al.*, 1994] and thus the high velocity deviation in all velocity data above the BSR from the reference trend is a strong local anomaly and (2) there is no clear systematic sediment composition change in the upper 225 m of the ODP Sites 889/890 sediment section that could explain such anomalously high velocities [*Westbrook et al.*, 1994].

3.5.2 Reference Velocity Information From ODP Logs

A constraint on the reference velocity has also been obtained from other ODP non-velocity logs at Site 889, from 70 to 250 mbsf. The Schlumberger high-temperature lithodensity tool (HLDT) determines formation bulk density (actually electron density) by measuring the absorption of gamma rays emitted by a radioactive source [e.g., *Westbrook et*

al., 1994]. The no-hydrate reference profile can be estimated using a velocity-density relation assuming that the measured gamma ray densities are largely unaffected by the partial replacement of the pore water with hydrate which has a similar density. Anomalously low density values occurred in the density log, which were considered to be artifacts of the variably enlarged hole. *Jarrard et al.* [1995] used a combination of caliper, photoelectric factor, and $\Delta\rho$ logs from two separate detectors of HLDT logging tool to guide the editing of the density log. Only 37% of the recorded data at Site 889 were accepted as reliable. In this study, their accepted data are taken as the formation bulk density unaffected by the presence of hydrate. It should be noted, however, that the edited density data retained only the high values. If some of the rejected values are in fact valid, this editing will have biased the average density to be too high and the inferred reference velocity to be too high.

The sediment porosities can be computed from the log bulk densities using a grain density of 2680 kg/m^3, based on ODP core index measurements [*Jarrard et al.*, 1995]. The velocity/porosity relation discussed in the previous chapter (Figure 2.11) was used to convert the inferred porosity log to the velocity-depth profile which is shown in Figure 3.12 together with the MCS velocities. The velocities from the density data average between 1600 and 1700 m/s in the logged interval, slightly higher than the reference velocities from upward extrapolation of the MCS data. In the vicinity of the BSR, the density based velocities follow the MCS reference velocity trend well.

Neutron logs respond primarily to hydrogen content as neutrons lose energy when colliding with hydrogens of similar atomic mass. Neutron porosity can also be calculated assuming that all hydrogen is in the form of pore water. The neutron porosity logs at Site 889

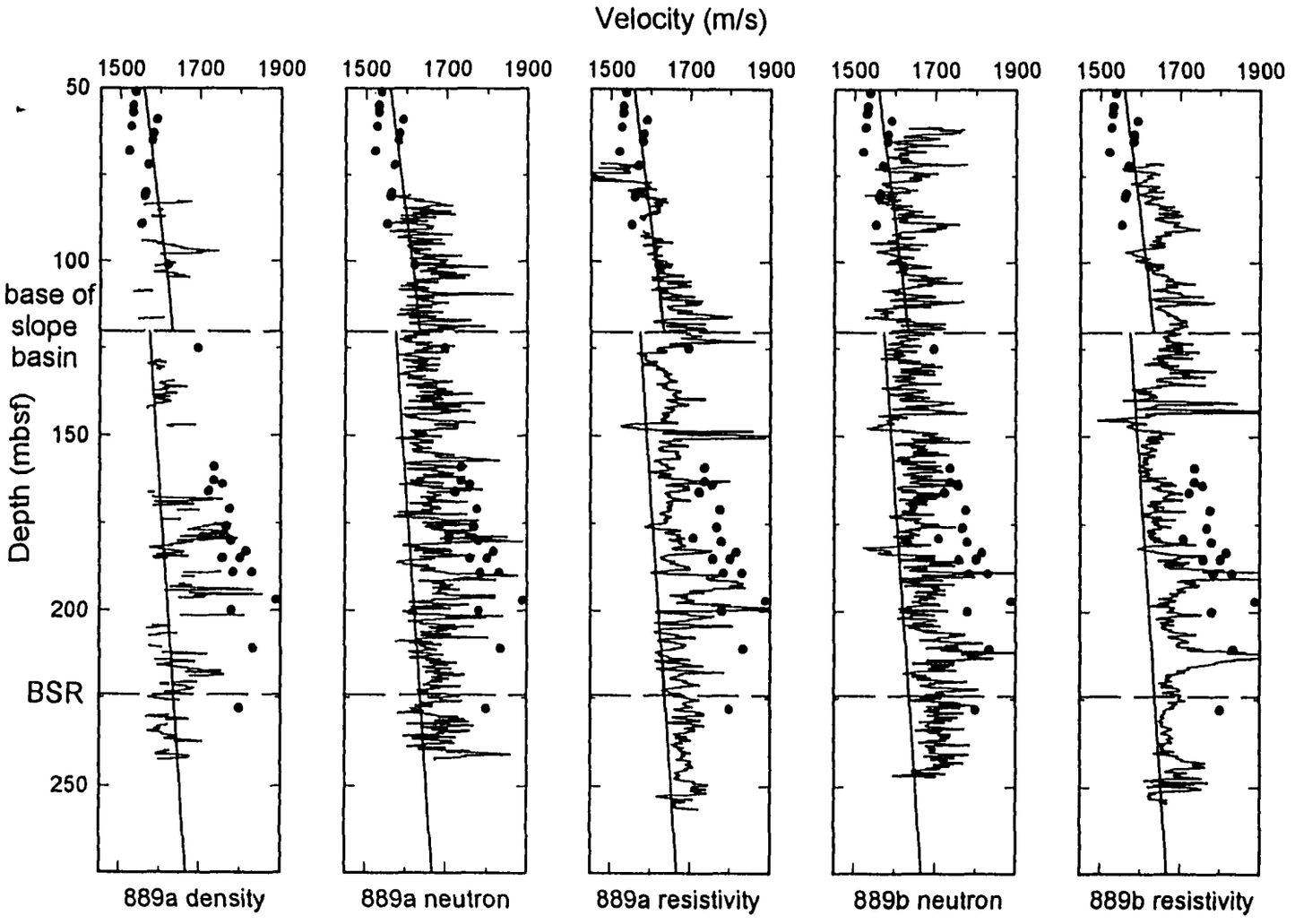

Figure 3.12 Velocities inferred from ODP downhole gamma ray density, neutron porosity, and resistivity logs at Site 889 (light solid lines). These data serve as a reference velocity trend in the interval where hydrate possibly exists. The MCS velocities (solid circles) and the reference velocity trend (heavy solid lines) are also plotted for comparison.

are similar to the density-based porosities and have also been converted to velocities using the velocity/porosity relation shown in Figure 2.11. The neutron porosity-based velocities shown in Figure 3.12 are again slightly higher than the reference velocities but more than 100 m/s lower than the sonic and MCS velocities. The resistivity logs at both 889a and 889b have similar characteristics (Figure 3.12). Electrical resistivity responds inversely to sediment water content and salinity, and thus porosity estimates can be made using the resistivity log. Using the same approach to convert porosity to velocity as above, the resulting resistivity-based velocities increase with depth closely following the basin trend from 50 to 120 mbsf. In the section below 120 mbsf, the resistivity logs and resistivity-based velocities show a decrease possibly related to the accreted sediments. Overlying the BSR, several spikes show higher velocities and resistivities than typical for such low-porosity sediments, indicating the presence of methane hydrate.

Two types of laboratory measurements on core recovered from the ODP Site 889 could provide reference velocity information. Core velocities will approximate the sediment velocities before original hydrate formation if the hydrate dissociation upon recovery did not significantly disturb the porosity and sediment structure. Unfortunately, the cores were highly disturbed by free gas formed upon hydrate dissociation in the zone above the BSR (see photographs of *Westbrook et al.* [1994]), and no useful laboratory velocities were obtained. Numerous core bulk density and porosity measurements were made that could be converted to reference porosity in the same manner as described above for the density logs. The resulting reference velocities above the BSR are slightly higher than that estimated from upward extrapolation of the MCS data, but lower than downhole log, VSP, and MCS

velocities. Again sample disturbance is a problem and only the more indurated high-velocity samples which are nonrepresentative could be measured.

3.6 Conclusions

An integrated analysis of multichannel seismic and ODP downhole velocity data for an area of the Cascadia mid continental slope off Vancouver Island has allowed the velocity enhancement associated with the presence of hydrate to be estimated. The multichannel, downhole log, and downhole VSP velocity-depth profiles are in excellent agreement where they overlap from just below the seafloor down to the depth of the BSR. The increase in seismic velocity associated with the formation of gas hydrate in marine sediments can be used to obtain semiquantitative estimate of hydrate concentration. The reference velocity-depth profile for no hydrate has been obtained by upward extrapolation of the deeper MCS velocities and through the downhole density log. This reference is critical in estimating hydrate or methane gas concentration and performing full waveform inversion to examine velocity structure of the BSR in detail. The velocity enhancement increases downward from near zero at the seafloor to a maximum of about 200 m/s above the BSR at 224 mbsf. Just above the BSR the velocity is increased to about 1800 m/s from the no-hydrate reference of 1600 m/s. On a seismic wavelength scale the velocity enhancement has a gradational top and increases smoothly with depth to the BSR, which explains why there is no consistent seismic reflection from the top of the hydrate layer. At ODP Sites 889/890, the clear velocity increase due to hydrate above the BSR accounts for ~2/3 of the impedance contrast required to produce the BSR reflection amplitudes. The remainder of the impedance contrast appears

to come from the velocity decrease associated with small concentrations of free gas below the BSR, which is resolved in the downhole VSP data.

CHAPTER 4 BSR REFLECTION AMPLITUDE VARIATIONS WITH OFFSET

The characteristics of reflection amplitude-versus-offset (AVO) can be an important indicator of sediment physical properties since AVO depends on the variations of P and S-wave velocities across the reflection interface [e.g., *Ostrander*, 1984; *Shuey*, 1985; *Rutherfold and Williams;* 1989]. The AVO analysis is a well established technique in the petroleum industry for gas exploration. It is based on the theory and observation that free gas substantially reduces the P-wave velocity with little effect on S-wave velocity and thus changes Poisson's ratio, such that the reflection amplitude increases with increasing reflection angle or offset. In standard AVO analysis offset-dependent amplitude variations are used as an indicator of gas and to estimate the Poisson's ratio contrast. The reflector commonly occurs at a shale/gas-sand interface for most gas reservoirs. The situation is however quite different for unconsolidated near-seafloor sediments containing hydrates or free gas. The hydrate BSR doesn't occur at a lithology boundary, and the gas layer involved below the BSR is usually thin. The hydrate BSRs also possesses detailed amplitude characteristics that are uncommon in the standard AVO analysis.

In this chapter, reflection characteristics of the BSR on MCS lines L89-08 and L89-10 are presented to illustrate the AVO of the BSR. The BSR amplitudes along seismic lines can allow mapping of hydrate areal distributions. Many authors have studied the AVO effect of the BSR [e.g., *Minshull and White*, 1989; *Hyndman and Spence*, 1992; *Bangs et al.*, 1993;

Katzman et al., 1994; *Andreassen et al.*, 1995]. They have shown in models that the variation of reflection amplitude with increasing incidence angle is strongly dependent on the contrast in Poisson's ratios at the interface. In this study the physical parameters for unconsolidated sediments at the BSR depth of ODP sites 889/890 are determined from theoretical calculations and from ODP log data to model the AVO effect. The amplitude behaviour of the hydrate BSR is found not to be as useful as was earlier predicted to determine the amount of free gas below the BSR. This is because the Poisson's ratio changes at the BSR in the unconsolidated sediments are likely very small and ambiguity in the models arises when there is no reliable S-wave velocity information.

4.1 Observed Offset-dependant Amplitude Behaviour of the BSR

For the AVO analysis, the following processing sequence and corrections were applied to the MCS data to obtain true amplitude-versus-offset data: (1) shot domain signature deconvolution (source wavelet removal and zero phase output), (2) spherical divergence spreading loss correction, and (3) source and receiver array directivity correction. The hydrophone receiver and the air gun source array both have large directivity attenuations that are important for the BSR analysis. The receiver array attenuation depends on the total number of hydrophones and the hydrophone spacing interval Δx. For the BSR characteristic wave length of λ, the hydrophone array directivity attenuation as a function of incidence angle α can be calculated following *Sheriff and Geldart* [1982]:

$$F = \frac{\sin[n\pi(\frac{\Delta x}{\lambda})\sin\alpha]}{n\sin[\pi(\frac{\Delta x}{\lambda})\sin\alpha]}, \qquad (4.1)$$

where n is the total number of hydrophones in the array. The amplitude attenuation is about 20% at an angle of 45°, the maximum incidence angle at the BSR depth for the main area studied. The air gun array attenuation with angle is more complex because of the bubble pulse, ghost reflection from the sea surface, and the array configuration of multiple interacting sources with different signal dominant frequencies and amplitudes. A model of the waveform as a function of incidence angle based on method of *Giles and Johnson* [1973] was provided by the data acquisition contractor, Digicon Geophysical Corporation, to give the source array attenuation. The combined source and receiver array attenuation is negligible near vertical incidence, but reaches 50% at far offset corresponding to an incidence angle of 45° for the BSR [*Hyndman and Spence*, 1992]. This directivity correction has been applied to the CDP gathers before AVO modelling and inversion either in x-t (offset-traveltime) or ω-p (frequency-slowness) domain.

The BSR amplitudes typically do not increase linearly with offset as is commonly assumed in the standard AVO analysis. Rather they increase slowly or decrease at near offsets then increase rapidly at far offsets. Figure 4.1 illustrates a typical normal moveout (NMO) corrected common-depth-point (CDP) gather from L89-08 near the ODP drillsites 889/890. Source and receiver array directivity corrections have been applied. The BSR at this location exhibits a constant or a small decrease in amplitude to an offset distance of about 2000 m and a rapid increase at far offsets. Figure 4.2 shows measurements of directivity-

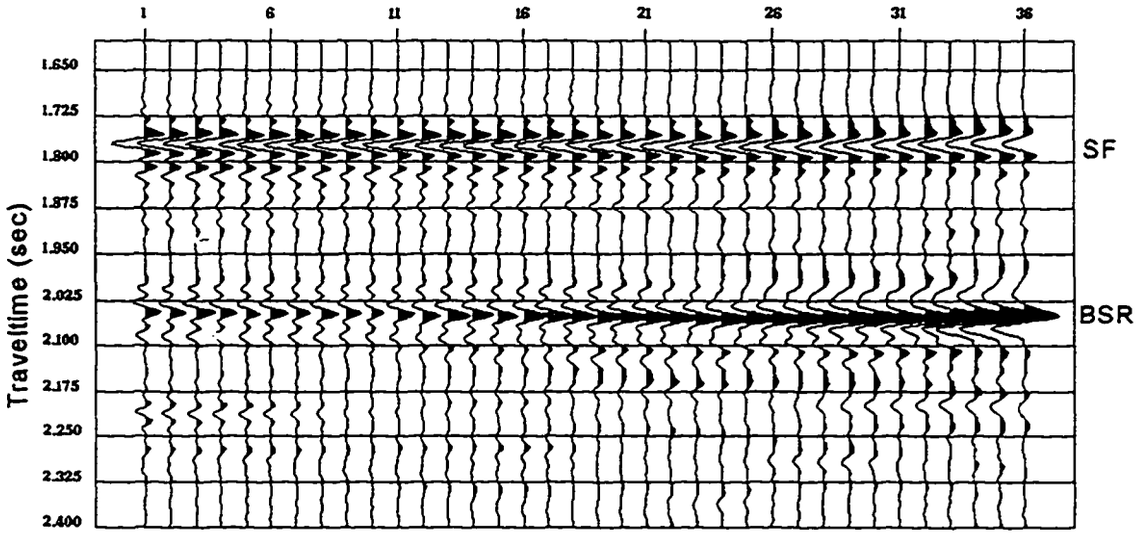

Figure 4.1 Common-depth-point gather with normal moveout and array directivity corrections from L89-08 at CDP 3091 near the ODP drillsites, illustrating the seafloor and BSR amplitude-versus-offset behaviour. The trace spacing within the gather is 100 m and the offset range is from 183 to 3585 m.

corrected and uncorrected amplitudes for the seafloor and BSR from four adjacent gathers of L89-08. Amplitudes have been normalized to the near offset value. The seafloor amplitudes decrease approximately linearly with offset, while the BSR amplitudes increase rapidly beyond the mid-offset range of about 2000 m.

To examine the lateral amplitude variations of both the seafloor and BSR, limited offset stack sections from L89-08 were produced in the vicinity of the ODP sites. As noted above, the stacked amplitude for the BSR does not increase much in the near to mid offset ranges (Figure 4.3a and 4.3b), but it increases substantially on going to the far offsets (Figure 4.3c). No array directivity correction has been applied for these stack sections, so that the BSR amplitudes at the far offsets are only 40-50% of their corrected values. The BSR

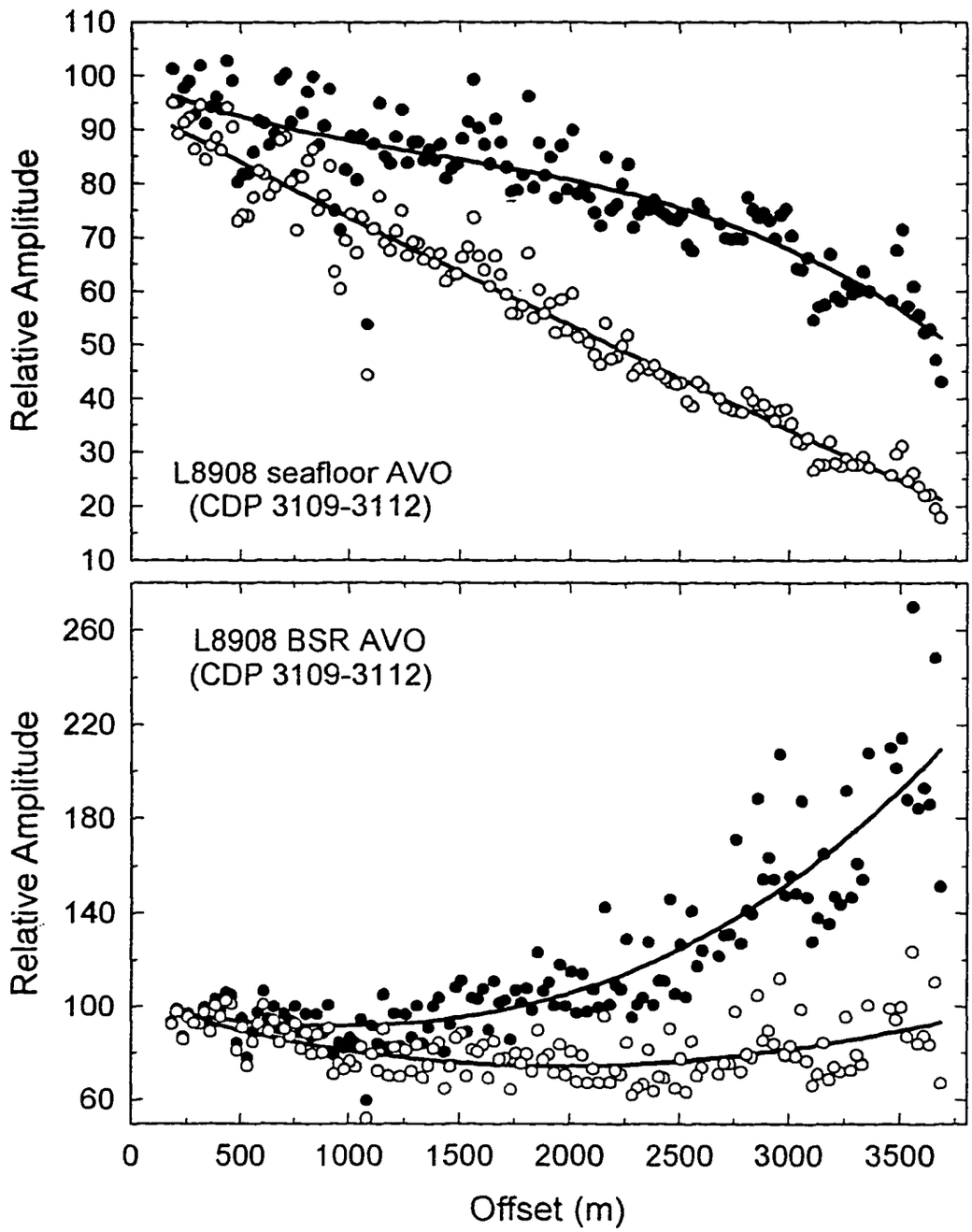

Figure 4.2 AVO for four gathers (CDP 3109-3112) from L89-08 at the ODP drillsites 889/890. The amplitude values are normalized to 100 for the average at near offset. The array directivity corrected and uncorrected amplitudes are shown with solid and open symbols, respectively. Heavy lines are the 3rd order regression through the measured amplitudes.

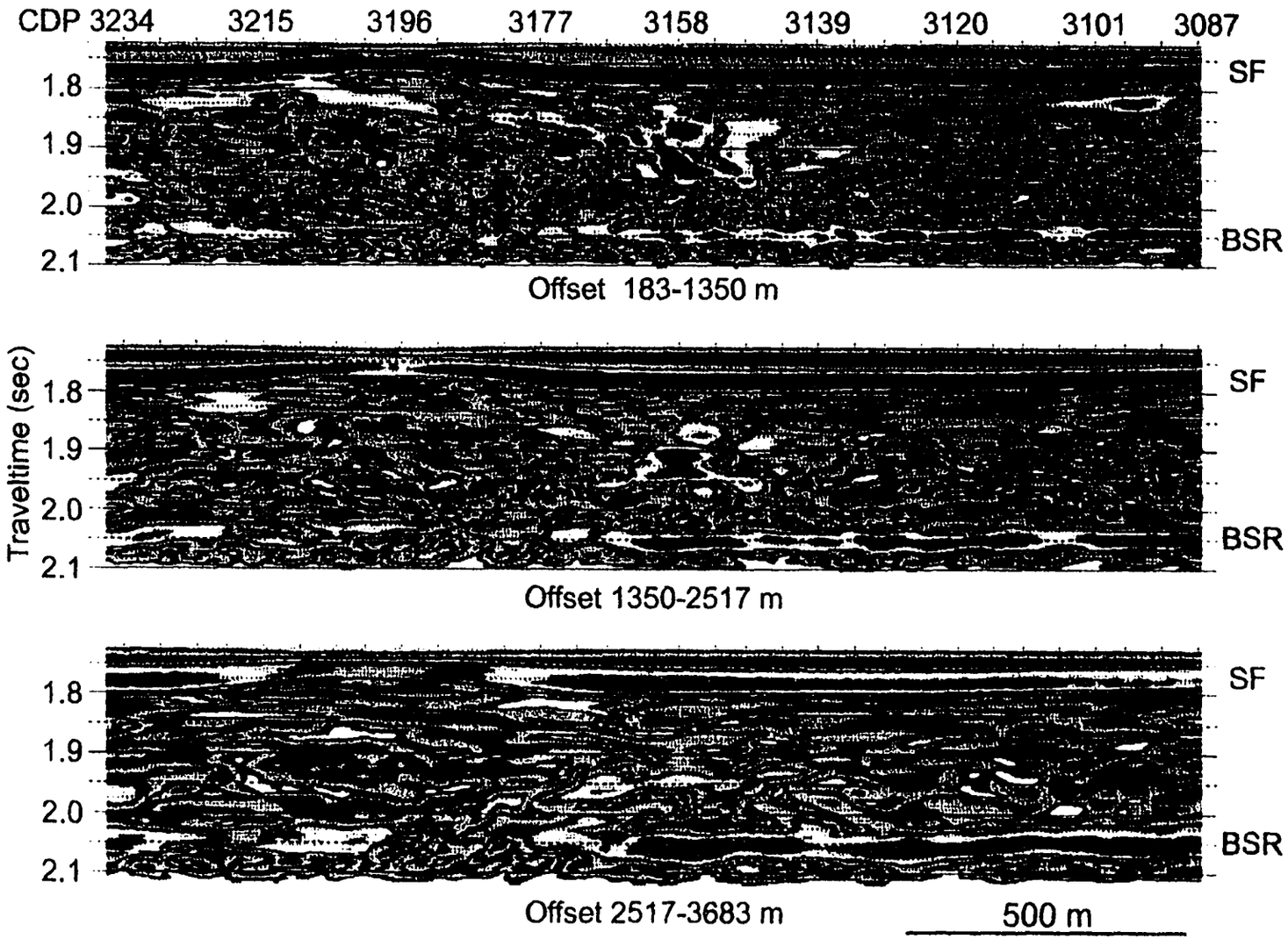

Figure 4.3 Range-limited stack sections for the near (183-1350 m), middle (1350-2517 m), and far offsets (2517-3683 m) along L89-08 near the ODP sites 889/890.

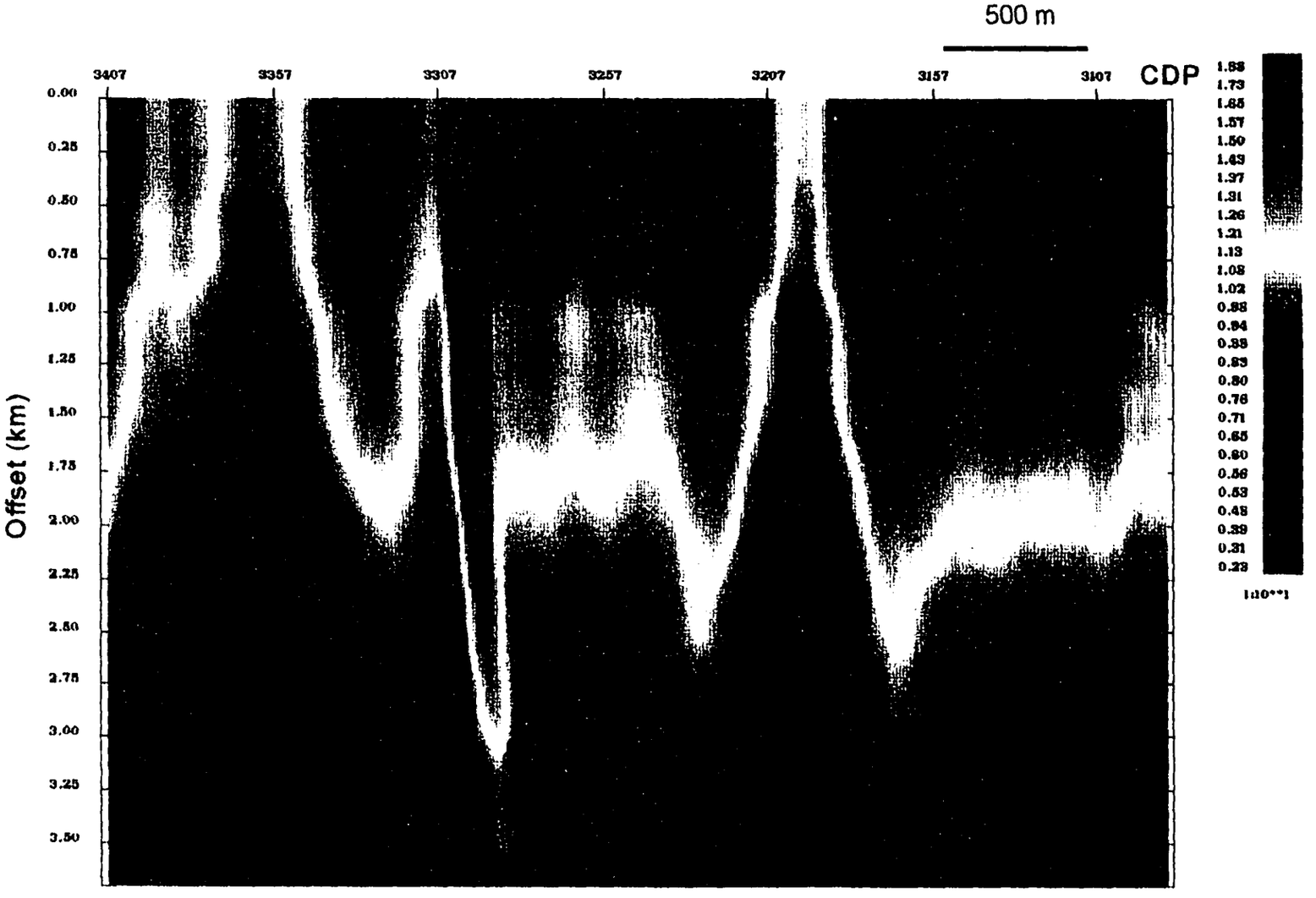

Figure 4.4 Seafloor amplitude variations over both offset and lateral distance along L89-08 near the ODP sites 889/890.

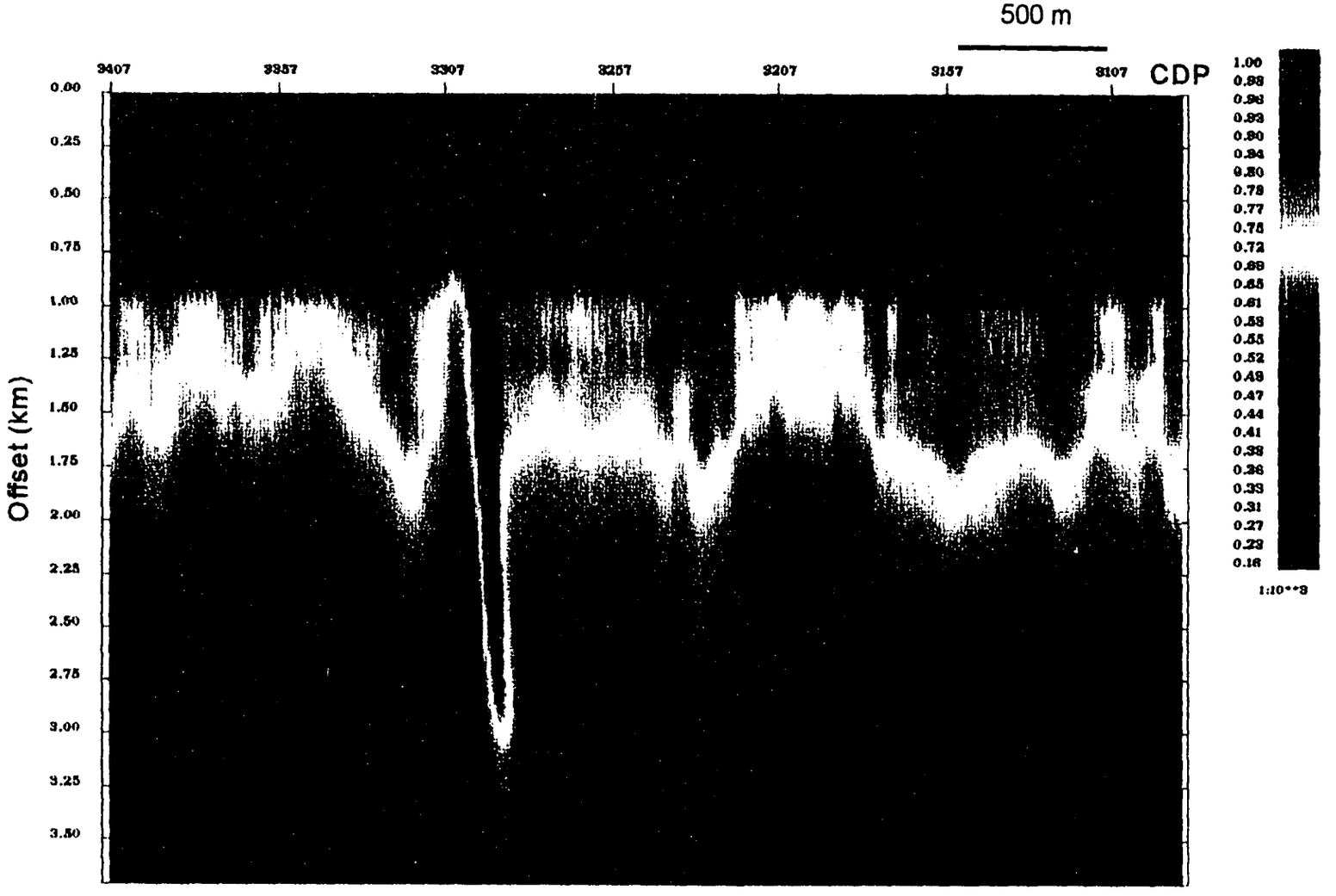

Figure 4.5 L89-08 seafloor reflection amplitudes with measured amplitudes being normalized to the average value of the three near-offset traces.

amplitudes shown in Figure 4.3 are generally high from CDP 3080 to 3160. A gentle seafloor topographic high near CDP 3200 may have a de-focussing effect which is responsible for the relative low reflection amplitudes from both the seafloor and BSR.

There are lateral variations in AVO over short distances, sometimes less than 100 m. To examine the amplitude variations with offset along a line, the seafloor and BSR amplitudes were picked on NMO-corrected CDP gathers with an offset range up to 3.7 km, at an interval of 12.5 meters. The lateral distances are 4 km for L89-08 (Figures 4.4-4.7) and 5 km for L89-10 (Figures 4.9-4.10). A weighted smoothing in a 2-D window of 200x60 m was then applied to remove small scale amplitude changes. The amplitudes, uncorrected for array directivity attenuation, were colour contoured.

Some large scale-amplitude variations appear to be produced by varying seafloor conditions, such as focussing and de-focussing by seafloor topography and the scattering by surface roughness. Examples of focussing and defocussing can be found near CDP 3200, 3300, and 3360 in Figure 4.4 where the seafloor amplitudes have been significantly altered by the seafloor features, similar to the topographic high shown in Figure 4.3. These variations make the lateral amplitude comparisons difficult, but they can be removed by normalizing amplitudes to the near offset value (e.g., Figure 4.5). After normalization, the seafloor amplitudes along L89-08 decrease linearly with increasing offsets over much of the measured distance range.

The same procedure was applied to the measured BSR amplitudes. Figures 4.6 and 4.7 display measured and normalized BSR amplitude contour plots. High amplitudes are seen on the right hand side of Figure 4.6, which corresponds to the high amplitude region

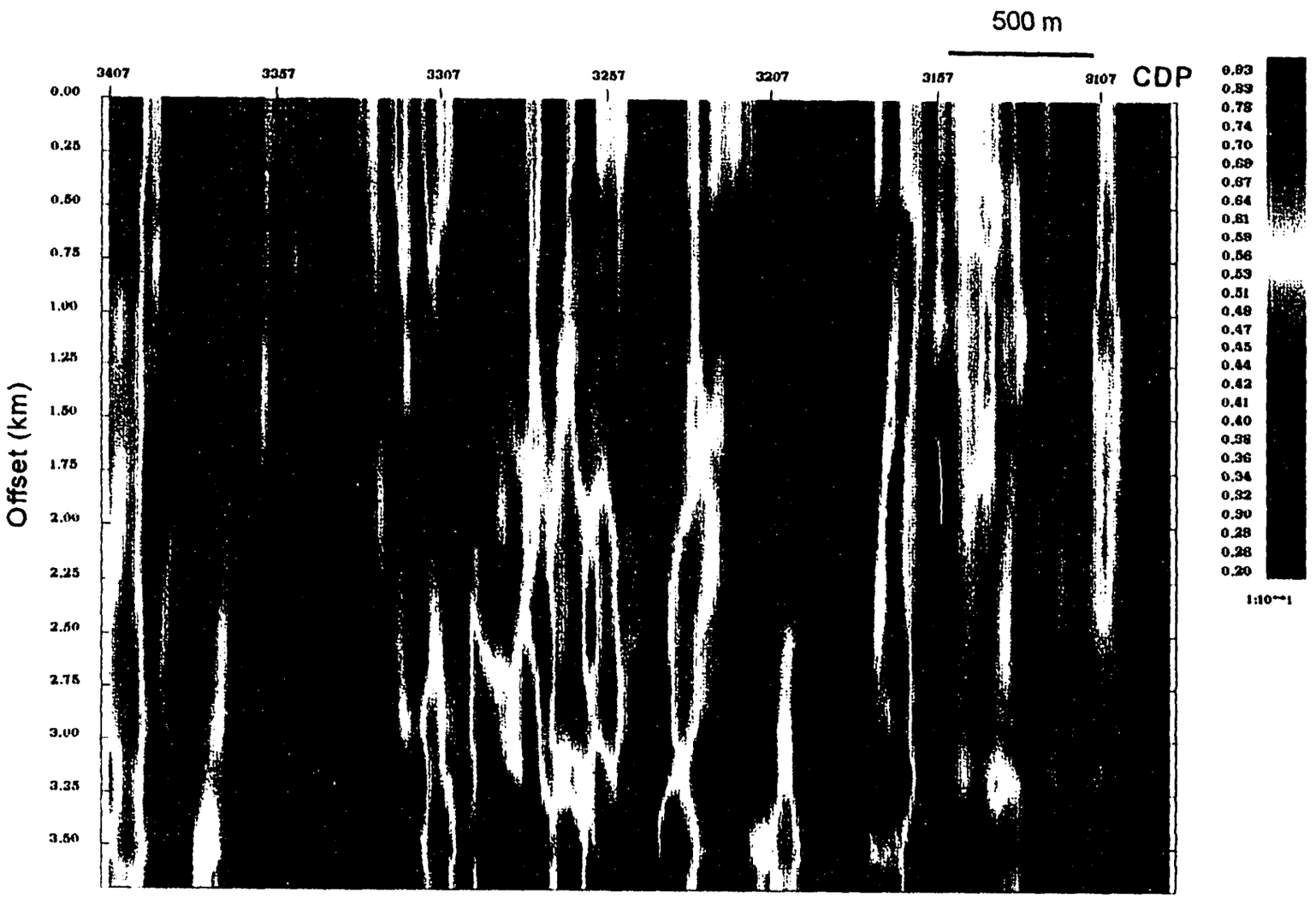

Figure 4.6 BSR amplitude variations over both offset and lateral distance along L89-08 near the ODP sites 889/890.

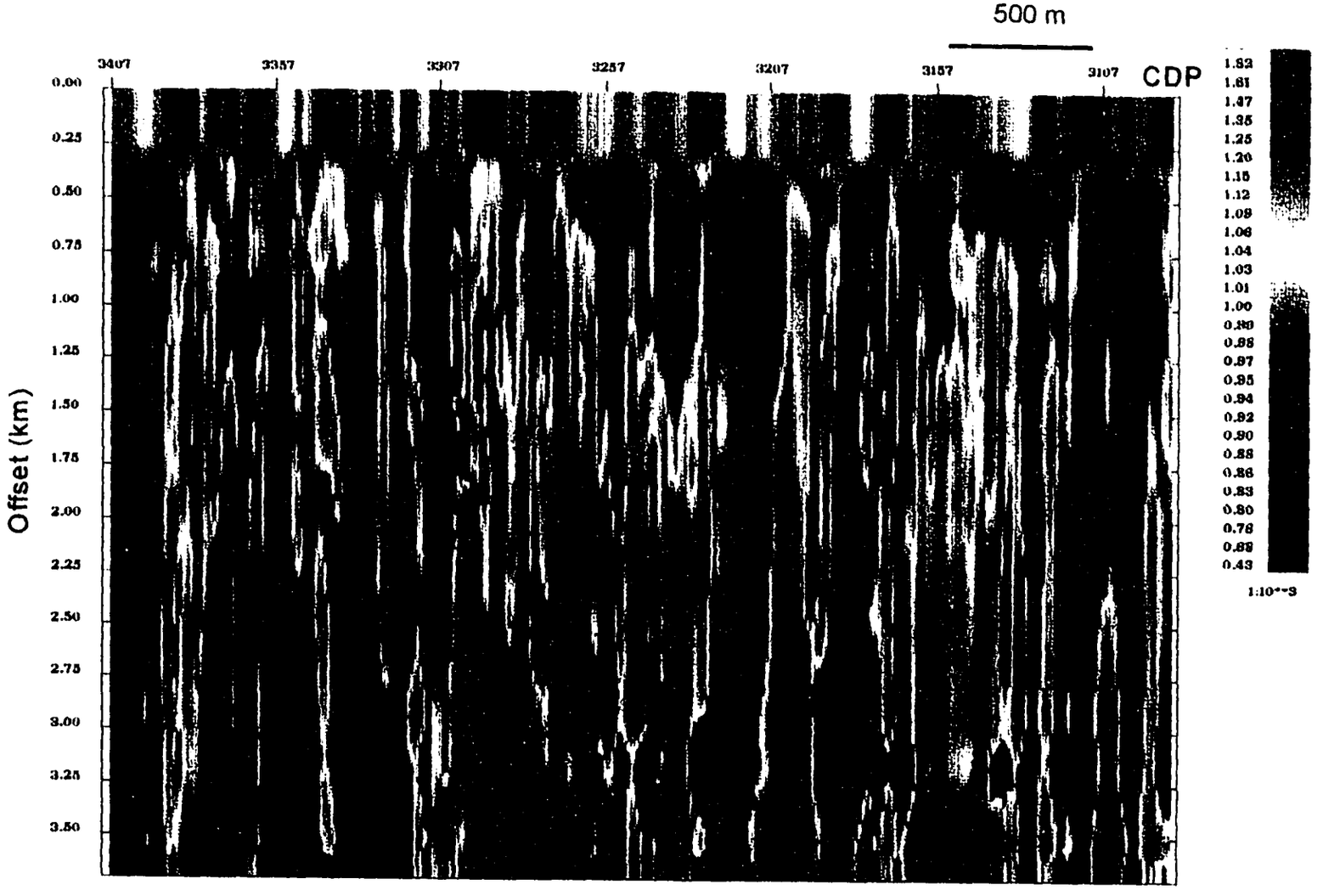

Figure 4.7 L89-08 BSR reflection amplitudes with measured amplitudes being normalized to the average value at the near offset.

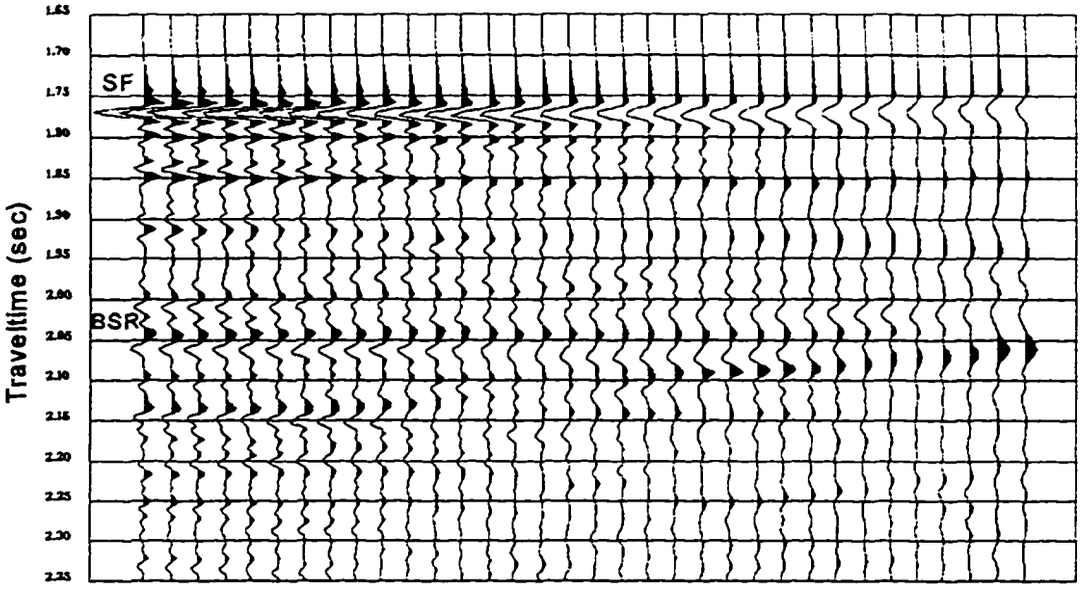

Figure 4.8 Common-depth-point gather with normal moveout from L89-08 at CDP 3183. The high BSR amplitudes at far offsets have been reduced by the interference from an event below the BSR.

from CDP 3080 to 3160 on Figure 4.3. Again, the subdued amplitudes near CDP 3200 and 3360 are attributed to the seafloor topography. With amplitude normalization applied (Figure 4.7), the BSR amplitudes are seen to increase with offset over most of the measured region, although there is decrease in amplitude with offset for some limited regions. Even higher amplitudes at the far offsets are expected when array directivity attenuation is removed. The lateral BSR amplitude variability, shown as vertical strip patterns at a scale of one to several hundred metres, is possibly due to variations in hydrate distribution. The recent ODP drilling on the Blake Ridge of the eastern U.S. margin documented hydrate occurrences varying from finely disseminated hydrate occupying sediment pore space to nodules of solid hydrate, as well as one massive gas hydrate zone greater than 30 cm in thickness [*Matsumoto*, 1996].

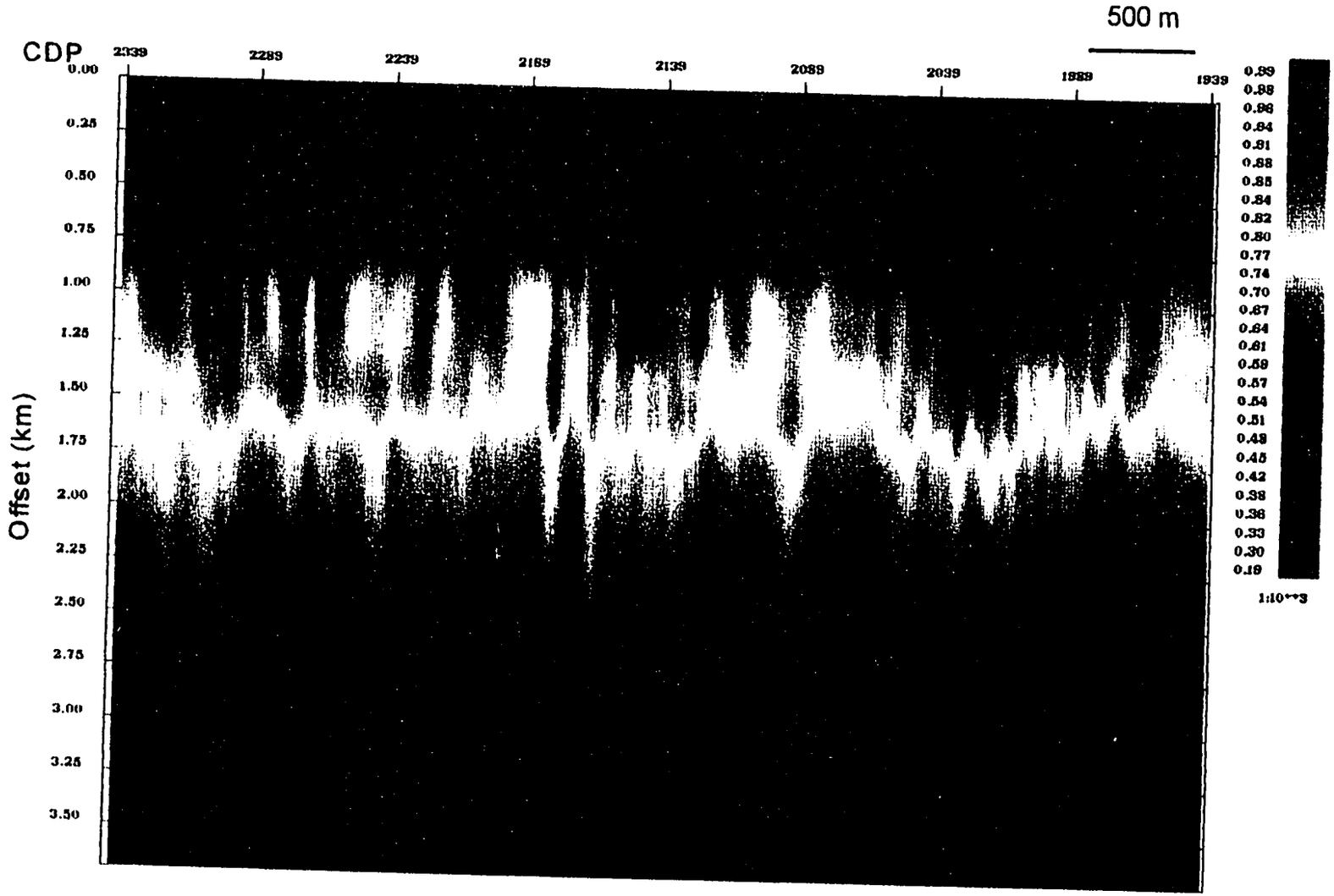

Figure 4.9 1.89-10 seafloor reflection amplitudes with measured amplitudes being normalized to the average value at the near offset.

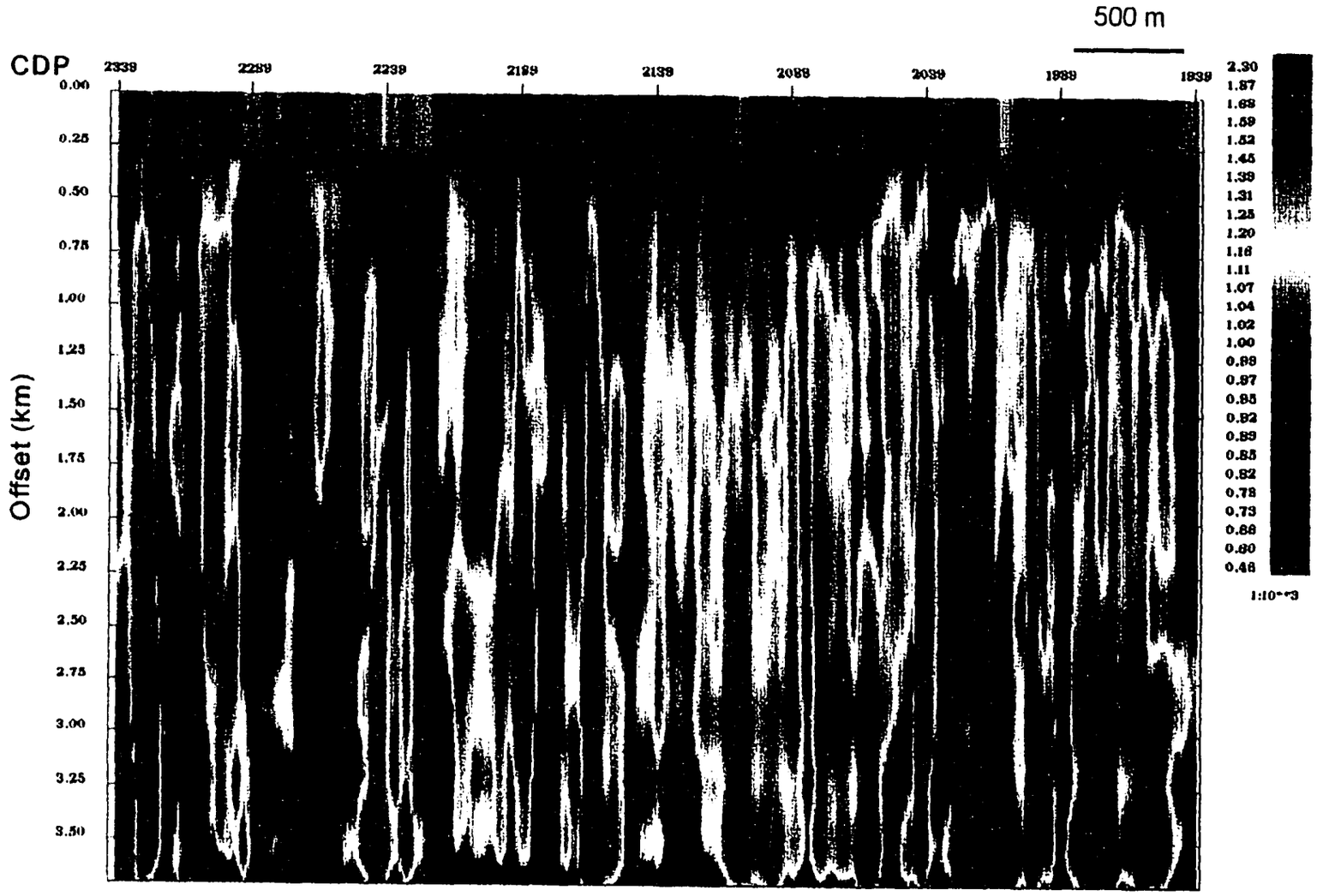

Figure 4.10 1.89-10 BSR reflection amplitudes with measured amplitudes being normalized to the average value at the near offset.

The reflection amplitudes will certainly be influenced by such uneven areal distributions.

At some locations, the BSR amplitudes are contaminated by the interference from other reflections and the AVO character is distorted. Figure 4.8 shows an example at CDP 3183 from L89-08. The BSR amplitudes at mid to far offsets are reduced by the interference from a later event, which causes the overall subdued AVO character in the region near CDP 3183 shown in Figure 4.7.

Figures 4.9 and 4.10 illustrate L89-10 seafloor and BSR reflection amplitudes with normalization applied. The seafloor amplitude behaviour on L89-10 is more uniform than on L89-08. However, the BSR amplitude characteristics are comparable to those on L89-08, having increasing amplitudes with offsets and having laterally varying AVO.

4.2 Sediment Physical Properties Used in the Modelling

4.2.1 Density and Porosity Measurements from ODP data

Sediment physical properties were measured on cores recovered from Holes 889A/B and 890B during ODP Leg 146 [*Westbrook et al.*, 1994]. Figures 4.11a and 4.11b present the bulk density and porosity data derived from index properties. The sediments in the cored interval are dominated by interbedded silts, clays, and fine sand. In general, bulk density increases and porosity decreases, as expected for gravitational compacting sediment. Sharp lithologic and grain size changes or diagenetic-related excursions to higher bulk densities occur locally. Superimposed on this general trend there is an increase in density and decrease in porosity at ~150 mbsf at the base of the slope basin, and perhaps a small change at the BSR at 250 mbsf. The bulk density generally varies from 1.8 to 2.0 Mg/m^3, and the

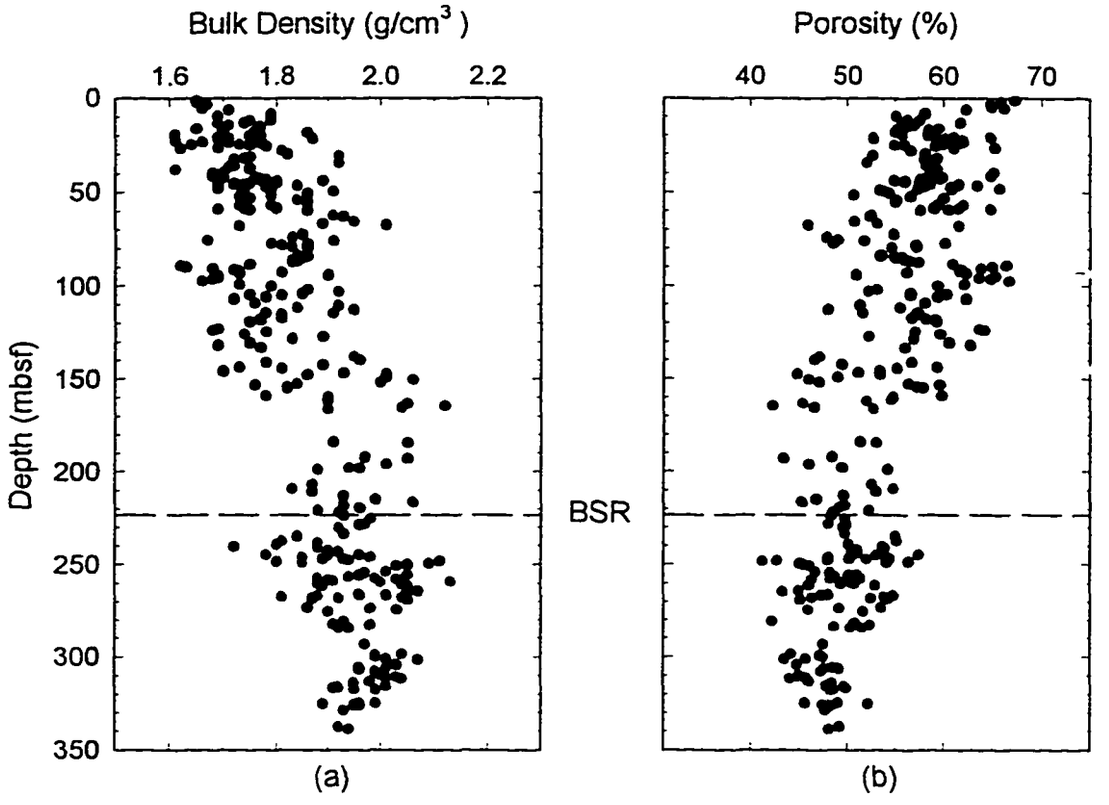

Figure 4.11 (a) Bulk density measured from core samples at ODP Holes 889A/B and 890B. (b) Porosities at ODP Holes 889A/B and 890B as a function of sub-bottom depth (from *Westbrook et al.*, 1994).

average porosity is 50% in a ~100 m interval above the BSR.

4.2.2 Velocity of Hydrate-bearing Sediment

The relation between velocity enhancement and hydrate concentration depends upon the degree to which the hydrate forms at grain boundary contacts or in the main pore spaces [e.g., *Dvorkin et al.*, 1991]. Because there is little information on the grain-scale distribution of the hydrate, a simple model approximation to relate the amount of hydrate concentration in the pore space to sediment P-wave velocities has been used. A number of other

approaches have also been suggested, but those that give the correct reference velocity for no-hydrate are quite similar (see discussions by *Desmons*, 1996). In the model used here, a velocity is obtained for the combination of pure hydrate and the sediment matrix, i.e., the velocity of fully hydrate-saturated sediment (no pore fluid). This composite matrix is then combined with water-saturated sediment (no hydrate) to determine an overall model velocity [*Lee et al.*, 1993; *Wood et al.*, 1994]. The velocity of water-saturated sediment, V_{sed}, is taken from the reference velocity at the level of the BSR, as defined in Chapter 3 (e.g., Figure 3.11). The velocity of fully hydrate-saturated sediment, V_{hysed}, is then determined by the simple time-average equation which works well for combining solid matrix materials [*Wyllie et al.*, 1958],

$$\frac{1}{V_{hysed}} = \frac{\phi}{V_{hyd}} + \frac{1-\phi}{V_m}, \tag{4.2}$$

where V_{hyd}, the velocity for pure methane hydrate, is taken to be 3730 m/s [*Pearson et al.*, 1983; *Sloan*, 1990] and V_m, the matrix velocity, is 4500 m/s [e.g., *Davis and Villinger*, 1992]. For porosities of $\phi = 0.45$ and $\phi = 0.55$, the calculated velocities for fully saturated sediment with hydrate filling all available pore space, V_{hysed}, are 4120 and 4040 m/s, respectively. The velocity of partially hydrate-bearing sediment with saturation S can then be approximated again by the time-average equation combining the velocity of hydrate saturated sediment with that of water saturated sediment containing no hydrate,

$$\frac{1}{V_p} = \frac{S}{V_{hydsed}} + \frac{1-S}{V_{sed}}, \tag{4.3}$$

Figure 4.12 shows a plot of P-wave velocity versus hydrate saturation in sediment for V_{sed}=1600 m/s and porosity ϕ=0.55 (lower line) and for V_{sed}=1700 m/s and ϕ=0.45 (top

line). The porosity values are based on results from ODP core measurements presented in Figure 4.11, and the velocities are appropriate for no-hydrate sediment based on the MCS and ODP velocity data discussed in Chapter 3. The patterned area in Figure 4.12 indicates the range of enhanced velocities, from 1700 to 1900 m/s, resulting from the presence of hydrate. Taking the porosity values from ODP data, the solid dots in Figure 4.12 suggest that hydrate

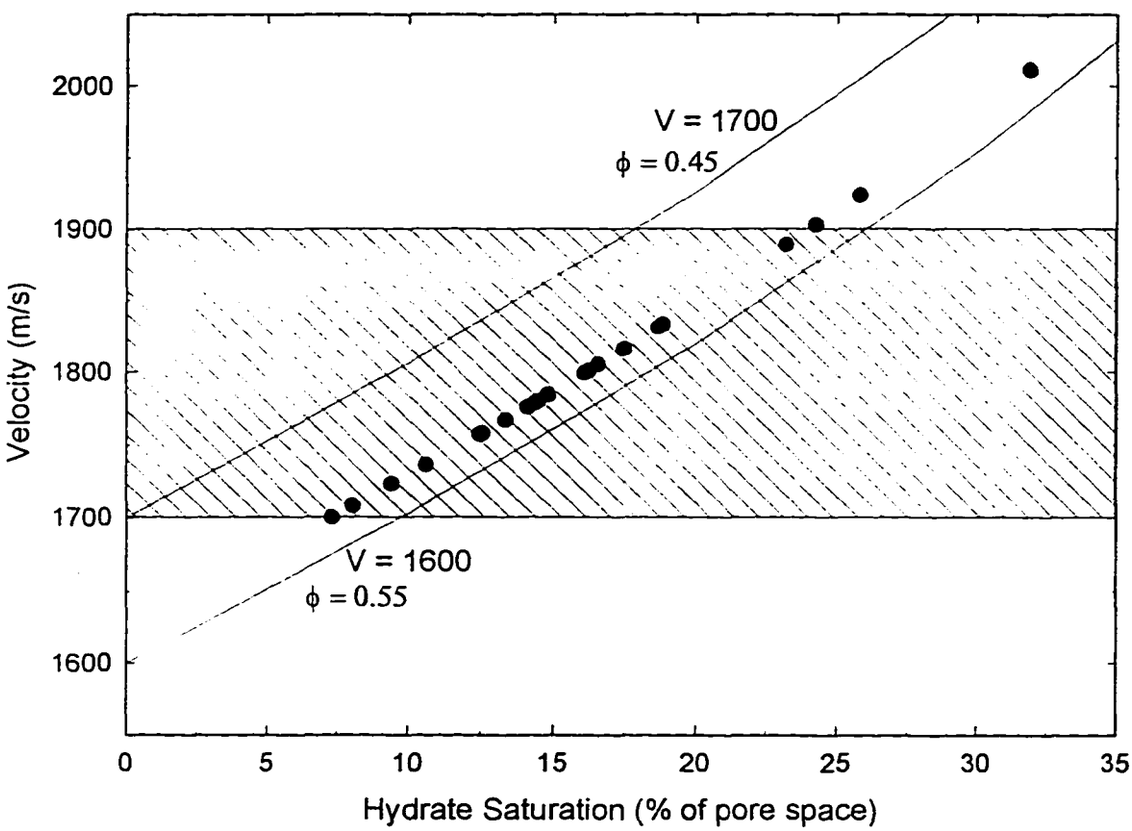

Figure 4.12 Sediment velocities enhanced by hydrate concentration from two sets of parameters: (1) hydrate-free velocity is 1700 m/s; fully hydrate-saturated velocity is 4120 m/s, for the sediment whose porosity is 45% (top solid line); (2) hydrate-free velocity is 1600 m/s; fully hydrate-saturated velocity is 4040 m/s, for the sediment whose porosity is 55%. Measured velocities (solid dots) between 1700 and 1900 m/s suggest that 10-25% of the sediment pore space is filled with hydrate.

saturation of 10-25% of the sediment pore space is required to explain the observed MCS velocities in the hydrate-enriched zone.

Little is known about S-wave velocities in hydrate-bearing sediment and no laboratory measurements of this type are available. Some S-wave velocity increase in the sediments is expected, as cementing of hydrate in the grain contact will likely increase the shear modulus of the sediment matrix. Assuming that S-wave velocity increases with hydrate concentration in proportion to the P-wave velocity increase, V_s (in km/s) can be estimated from P-wave velocity using empirical relationships of *Hamilton* [1979],

$$V_s = 1.137\, V_p - 1.485, \tag{4.4}$$

and of *Castagna et al.* [1985],

$$V_s = \frac{V_p - 1.36}{1.16}. \tag{4.5}$$

The latter equation gives lower V_s values than that obtained from (4.4) for the same V_p.

4.2.3 Velocity Estimates for Sediment Containing Free Gas

Free gas in a porous media causes a drastic reduction in P-wave velocity but has little effect on S-wave velocity [*Domenico*, 1976; 1977; *Gregory*, 1976; *Murphy*, 1984; *Ostrander*, 1984]. From Biot's theory, *Geertsma* [1961] developed a basic equation for P-wave velocity in a fluid-filled media. *Biot* [1956a, b] included the effect of viscosity of the fluid and he assumed that the fluid is compressible and that it may flow relative to the solid, causing

frictional losses. *Geertsma* [1961] obtained the P- and S- wave velocities as a function of frequency, as well as for the limiting cases of zero and infinite frequency. The P-wave velocity V_p and S-wave velocity V_s for partially gas-saturated oceanic sediment at infinite frequency are

$$V_p = \left\{ \left[\frac{1}{C_b} + \frac{4}{3}G_b + \frac{\frac{\phi\rho_b}{k\rho_f} + (1-\beta)(1-\beta-\frac{2\phi}{k})}{(1-\phi-\beta)C_s + \phi C_f} \right] \frac{1}{\rho_b(1-\frac{\rho_f\phi}{\phi_b k})} \right\}^{1/2},$$

$$V_s = \left[\frac{G_b}{\rho_b(1-\frac{\rho_f\phi}{\rho_b k})} \right]^{1/2}, \qquad (4.6)$$

where β is the ratio C_s/C_b, and k expresses the degree of coupling between pore fluid and rock matrix, ranging from unity for no coupling to infinity for perfect coupling [*Domenico*, 1976]. The meanings of the symbols in the above formulae and the values used for typical BSR depths of a few hundred metres below seafloor at the ODP sites 889/890 are given in Table 4.1.

The compressibility of pore fluid is given by

$$C_f = S_g C_g + (1-S_g)C_w, \qquad (4.7)$$

where C_g and C_w are compressibilities of methane gas and water, respectively, and S_g is the gas saturation.

It is assumed that the bulk compressibility C_b is determined by the compressibility of

Table 4.1 Quantities used in evaluating P-wave velocity for gas-saturated sediment [*Westbrook et al.*, 1994; *Minshull et al.*, 1994; *Desmons*, 1996]

Symbol	parameter	Value	Unit
C_b	compressibility of rock matrix (bulk compres.)	1.63×10^{-9}	Pa^{-1}
C_s	compressibility of solid grain	2.5×10^{-11}	Pa^{-1}
C_g	compressibility of methane gas	7.74×10^{-8}	Pa^{-1}
C_w	compressibility of water	4.19×10^{-10}	Pa^{-1}
C_p	compressibility of pore fluid	2.84×10^{-9}	Pa^{-1}
C_{p0}	pore compressibility at zero differential pressure	2.96×10^{-9}	Pa^{-1}
ρ_g	methane gas density	1.84×10^{2}	$kg\ m^{-3}$
ρ_s	sediment grain density	2.65×10^{3}	$kg\ m^{-3}$
ρ_w	sea water density	1.03×10^{3}	$kg\ m^{-3}$
ϕ	fractional porosity	50%	
G_b	shear modulus of rock matrix	5.7×10^{7}	Pa
k	coupling factor	3.0	

the solid grain C_s and pore compressibility C_p. The pore compressibility C_p is defined as pore volume change with respect to differential pressure P_d:

$$C_p = -\frac{1}{V_p}\frac{dV_p}{dP_d} \tag{4.8}$$

As bulk volume V_b is given by $V_b = V_s + V_p$, differentiation with respect to P_d and division by V_b gives

$$\frac{1}{V_b}\frac{dV_b}{dP_d} = \frac{1}{V_b}\frac{dV_s}{dP_d} + \frac{1}{V_b}\frac{dV_p}{dP_d}. \tag{4.9}$$

Noting that fractional porosity $\phi=V_p/V_b$ and $(1-\phi)=V_s/V_b$,

$$\frac{1}{V_b}\frac{dV_b}{dP_d} = (1-\phi)\frac{1}{V_s}\frac{dV_s}{dP_d} + \phi\frac{1}{V_p}\frac{dV_p}{dP_d}, \tag{4.10}$$

or,

$$C_b = (1-\phi)C_s + \phi C_p. \tag{4.11}$$

Pore compressibility C_p can be determined from the pore compressibility at zero differential pressure C_{p0} and the pressure gradient m:

$$C_p = C_{p0} + mP_d, \tag{4.12}$$

where differential pressure P_d is given by

$$P_d = (\rho_{av} - \rho_w)gz. \tag{4.13}$$

At a depth of 200 m below seafloor where average density ρ_{av} is about 1800 kg/m^3 and sea water density ρ_w is 1030 kg/m^3, differential pressure P_d is estimated as 1.5×10^6 P_a.

Density of pore fluid ρ_f depends on the fractional gas saturation S_g:

$$\rho_f = (1-S_g)\rho_w + S_g\rho_g, \tag{4.14}$$

where ρ_w is the density of seawater, and ρ_g is the density of methane gas. The bulk density ρ_b is then given by

$$\rho_b = \phi\rho_f + (1 - \phi)\rho_s \qquad (4.15)$$

For sea water density ρ_w=1030 kg/m^3, grain density ρ_s=2650 kg/m^3, and ϕ=0.5, the calculated bulk density ρ_b is 1840 kg/m^3 at zero gas saturation, which is in agreement with the ODP core density measurements just above the BSR as shown in Figure 4.11.

The shear modulus G_b in equation (4.6) was adjusted to obtain a P-wave velocity for

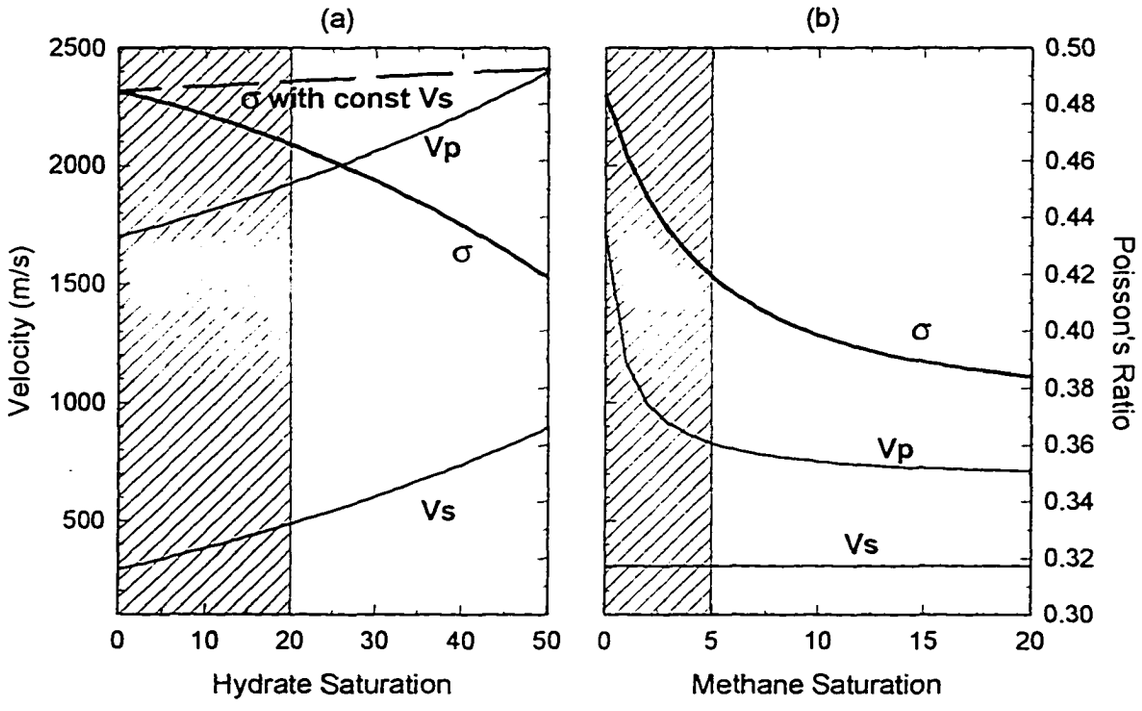

Figure 4.13 Variations of computed velocities and Poisson's ratio in marine sediment (porosity 0.5) at ~200 m subbottom with hydrate saturation (a) and methane gas saturation (b) in percentage of pore space. Poisson's ratios for hydrate and methane saturation are also shown. The hatched areas indicate the most likely hydrate saturation of 0-20% and methane saturation of 0-10%.

zero methane saturation consistent with the reference velocity at the BSR depth from the MCS data. An intermediate coupling factor of 3.0 is chosen for unconsolidated sediment at ~200 m depth below sea floor. With the quantities in Table 4.1, the compressional P-wave velocity of water-saturated sediment from equation (4.6) is 1718 m/s.

Figure 4.13 summarizes the velocity variations resulting from both hydrate and methane gas saturations that are measured as a percentage of pore space for sediment with a porosity of 50%. The P-wave velocity variations for hydrate saturation are obtained from equation (4.3) based on hydrate-free sediment velocity of 1700 m/s, and the S-wave velocities are obtained following *Castagna et al.* [1985]. Both V_p and V_s for gas saturations are from equation (4.6).

A small quantity of gas, 1-2%, in the pore space of sediment causes a dramatic decrease in P-wave velocity, while further increase in gas saturation makes little change. S-wave velocities however do not change much with increasing gas saturation as the shear modulus is not significantly affected by the presence of gas and the density change is very small for low gas saturations.

4.2.4 Poisson's Ratio Change at the BSR

Poisson's ratio has been commonly used as a representing parameter in AVO modelling since the offset-dependant amplitude variations are primarily determined by a contrast of Poisson's ratios [e.g., *Shuey,* 1985; *Hyndman and Spence,* 1992; *Minshull et al.,* 1994; *Katzman et al.*, 1994; *Andreassen et al.*, 1995]. Based on theory of elasticity, Poisson's ratio is derived as

$$\sigma = \frac{2 - (\frac{V_p}{V_s})^2}{2[1 - (\frac{V_p}{V_s})^2]}. \qquad (4.16)$$

Poisson's ratio σ will decrease with decreasing V_p/V_s as seen from Figure 4.14. A rapid change in Poisson's ratio occurs for a decrease in V_p/V_s from 3 to 1.4. This is the range for many consolidated sediments which is the reason that a small amount of gas in petroleum industry experience causes a large change in Poisson's ratio and thus in AVO. This is, however, not the predominant range of V_p/V_s encountered for the unconsolidated sediments several hundred meters below seafloor. For such sediments, a small amount of gas has less effect on Poisson's ratio and AVO. *Hamilton* [1979] presented in situ V_p/V_s values for water-saturated silt clays, turbidites, and mudstones (Figure 4.15a). V_p/V_s decreases with depth but is greater than 3 until below a subbottom depth of 600 m. For an S-wave velocity of 300 m/s, appropriate for water-saturated sediment at 2-300 m below seafloor, V_p/V_s is above 4 for the estimated range of P-wave velocities (Figure 4.15b), even for the low V_p caused by gas below the BSR. It follows that changes of Poisson's ratio are usually small for water-saturated

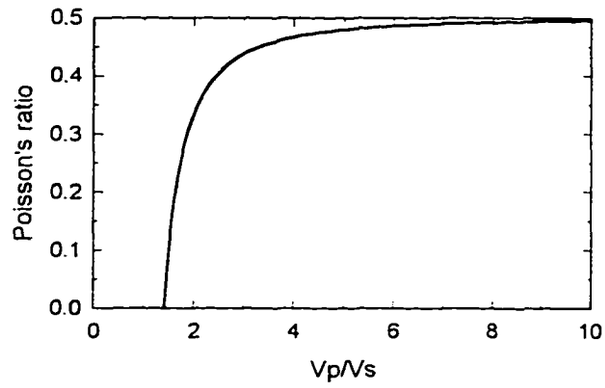

Figure 4.14 Poisson's ratio versus V_p/V_s. Large changes in Poisson's ratio occur for V_p/V_s from 3 to 1.4.

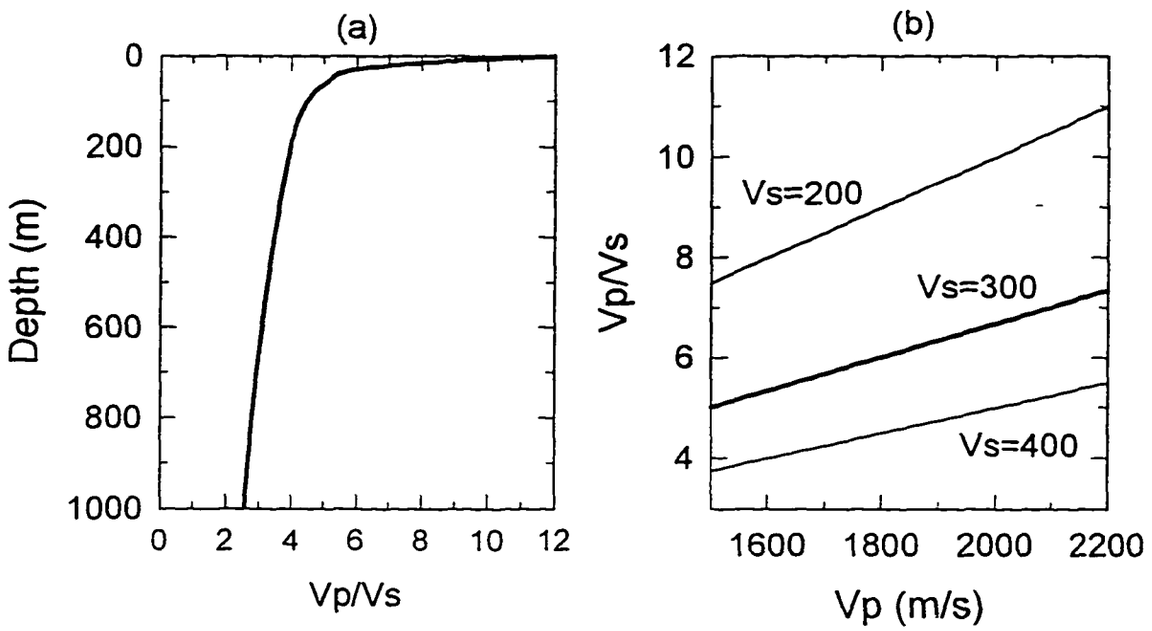

Figure 4.15 (a) V_p/V_s ratio in terrigenous sediments (from *Hamilton* [1979]). (b) V_p/V_s versus V_p assuming constant Vs of 200, 300, and 400 m/s.

unconsolidated sediments, porosity of ~50 %, at the BSR depth unless there is a large increase in S-wave velocity below the BSR, which is very unlikely.

For pure hydrate, Poisson's ratio of 0.33 has been measured in the laboratory [*Whalley*, 1980; *Pandit and King*, 1983]. Unfortunately, no laboratory or field data are available for the Poisson's ratio of sediments with partially hydrate-filled porosity and the effect of hydrate is difficult to estimate accurately. Figure 4.13a shows two possible scenarios as to how Poisson's ratio changes with hydrate saturation. If S-wave velocity is not affected by hydrate saturation, a small increase in Poisson's ratio will occur with increasing of hydrate saturation, due to the P-wave velocity increase. Since the effect of hydrate forming an

intergranular filling is to decrease the ratio of fluid/solid in the sediment and create cementation at the grain contact [*Dillon et al.*, 1980], the cemented sediment is expected to resist shear traction better and there should be at least some increased grain boundary competence. Therefore, an S-wave velocity increase is expected and a Poisson's ratio decrease will thus follow (Figure 4.13a). As Poisson's ratio in the sediment containing free gas relies mainly on the P-wave velocity, the above two scenarios lead to only a small Poisson's ratio contrast across the BSR for most of the possible hydrate and gas saturations indicated by the hachured areas in Figure 4.13. If the hydrate saturation is high and the gas saturation is low, the contrast in Poisson's ratio could become positive in the situation where S-wave velocity is increased by the hydrate cementation above the BSR. In general, the magnitude of Poisson's ratio change across the BSR is very small, and the ability of AVO analysis to resolve the presence of a small amount of gas is limited.

The above scenarios differ greatly from the gas-sand models common in the hydrocarbon exploration industry. In these models, a large Poisson's ratio drop is expected across a lithological boundary from a shaley cap rock to a sandy gas reservoir. The lithology change results in an increase in S-wave velocity. *Shuey* [1985] illustrated a typical field case of gas-sand in the Gulf of Mexico with S-wave velocity increasing from 940 m/s to 1300 m/s and Poisson's ratio decreasing from 0.4 in shale to 0.1 in underlying sand. In the case of BSRs, there is no large increase in S-wave velocity occurring below the reflector as the lithology does not change.

Laboratory and theoretical analyses show Poisson's ratio of 0.1 for consolidated sediment rocks with a small gas concentration [*Domenico*, 1976; *Murphy*, 1984; *Ostrander*,

1984]. Such Poisson's ratio are too low for the sediment at the BSR depth, as P-wave velocities of 1250-800 m/s commonly representing 1-5% of gas concentrations (see Figure 4.12) would imply S-wave velocities of 830-530 m/s. These values are not expected for high-porosity and water-saturated sediment several hundred metres below seafloor [*Halmilton*, 1979]. In the AVO modelling of *Hyndman and Spence* [1992], *Katzman et al.* [1994], and *Andreassen et al.* [1995], Poisson's ratios of 0.2-0.3 were used for sediment containing gas. For a P-wave velocity of 1250 m/s used in their modelling, these Poisson's ratio values give S-wave velocities up to 765 m/s which is probably still too high. Unlike in the standard AVO analysis and most BSR amplitude studies, where Poisson's ratio is used as a representative parameter, it should be noted in studying unconsolidated sediments that Poisson's ratio is determined by both V_p and V_s and V_s in the sediment containing hydrate is not a well determined parameter.

4.3 BSR Amplitude Modelling

4.3.1 Zoeppritz Reflection Coefficients

The observed AVO characteristics from the BSR, assuming a single interface, can be investigated using the Zoeppritz equations [*Bortfeld*, 1961; *Aki and Richards*, 1980; *Shuey*, 1985] which give the reflection coefficients for plane waves as a function of incidence angle and elastic parameters. *Minshull et al.* [1994] examined model AVO characteristics for a high amplitude BSR arising from the contact between overlying sediment containing hydrate and underlying sediment containing free gas of various amounts. Small amounts of free gas, 2-10%, and ~20% of hydrate seem to give the best match between the calculated reflection

coefficient and the observed AVO character. However, caution must be taken since only the maximum amplitude values are used and the BSR is treated as a simple plane boundary dividing two-half spaces. If velocity gradients or thin layers are present, the simple Zoeppritz equations are no longer valid and therefore this reflection coefficient calculation provides only a rough guide to the AVO behaviour.

A closed form of approximation of the Zoeppritz equation, which separates contributions from P-wave velocity V_p and Poisson's ratio σ, was given by *Shuey* [1985]:

$$R(\theta) = R_o + \left[R_o A_o + \frac{\Delta\sigma}{(1-\sigma)^2}\right] \sin^2\theta + \frac{1}{2}\frac{\Delta V_p}{V_p} (\tan^2\theta - \sin^2\theta), \qquad (4.17)$$

where

$$A_o = B - 2(1 + B)\frac{1-2\sigma}{1-\sigma}, \qquad B = \frac{\frac{\Delta V_p}{V_p}}{\frac{\Delta V_p}{V_p} + \frac{\Delta\rho}{\rho}}. \qquad (4.18)$$

The first term in the Zoeppritz equation is the normal incidence P-wave reflection coefficient, the second term contributes mostly at intermediate angles of incidence (<30°), and the third term is significant at larger angles. The reflection coefficient at vertical incidence, R_o, is negative for the BSR. If Poisson's ratio change $\Delta\sigma$ is negative, i.e., decreases downward, then the reflection coefficient $R(\theta)$ becomes more negative, or the magnitude increases with angle of incidence, as in the standard AVO analysis. However, if $\Delta\sigma$ is small, the second term

in equation (4.17) is insignificant and the reflection coefficients is almost unchanged with offset. If $\Delta\sigma$ is positive, the magnitude of reflection coefficient $|R(\theta)|$ will decrease at intermediate angles. For a P-wave velocity decrease at the BSR, the third term involving ΔV_p will result in an increase in $|R(\theta)|$, and at large incidence angles a rapid increase in the reflection amplitudes. Since Poisson's ratio is not expected to change much at the BSR, as discussed above, the BSR amplitude behaviour is thus controlled primarily by a change in P-wave velocity and is less by the small contrast in Poisson's ratio.

The model AVO behaviour, with nearly constant amplitudes at the near to mid offsets and a rapid increase in amplitudes at far offsets, is illustrated in Figure 4.16. The computed reflection coefficients are for typical elastic parameters of sediments at the BSR depth near the ODP 889/890 drill sites. P-wave velocities and densities above and below the BSR represent ~20% of hydrate saturation above the BSR and less than 1% of free gas below. S-wave velocities are obtained from P-wave velocities using the empirical relation from *Castagna et al.* [1985] shown in equation (4.5). Values of V_s calculated with Hamilton's relation (equation 4.4) are slightly higher than those from Castagna's, but they probably cover the range of S-wave velocity variations for unconsolidated marine sediments and the difference in the calculated reflection coefficients with two empirical relations is small. If no V_s increase occurs due to the hydrate above the BSR, a constant V_s of 250 m/s determined by the V_p below the BSR, reflection amplitudes increase almost monotonically with angle of incidence. If V_s above the BSR increases to 465 m/s as determined from the P-wave velocity of 1900 m/s, and there is a small Poisson's ratio increase at the BSR, the reflection coefficients are constant or decrease slightly at incidence angles of up to 35°. At larger incidence angles,

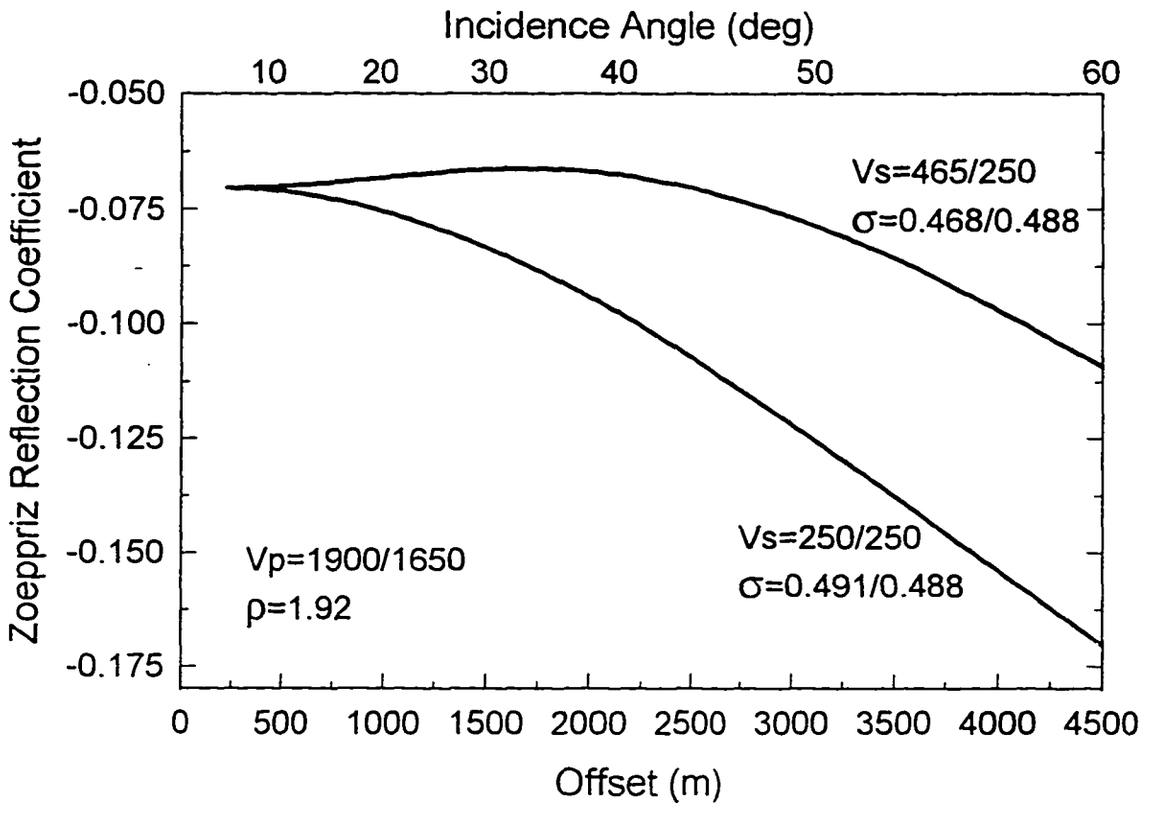

Figure 4.16 Computed BSR reflection coefficient with offset or angle of incidence, using the full Zoeppritz equation. P-wave velocity and density values above and below the BSR are fixed. S-wave velocities are obtained from P-wave velocities with empirical relation of *Castagna* [1985]. V_s and Poisson's ratio σ used to calculate the reflection coefficient are displayed with the corresponding curve.

i.e., beyond an offset of 2000 m, reflection amplitudes increase more rapidly.

This nonlinear model AVO behaviour agrees well with the BSR amplitude behaviour shown in Figures 4.1 and 4.2. Therefore, the nearly constant amplitudes at near to mid offsets and the rapid increase in amplitudes towards far offsets are probably due to a small increase or near zero Poisson's ratio change and a large V_p increase across the BSR. Furthermore, the S-wave velocity above the BSR, where hydrate increases the shear strength, may be larger

than below the BSR. This reduces the Poisson's ratio contrast and produces the non-linear BSR amplitude behaviour.

Ecker et al. [1996] recently presented impedance inversion results that suggested an increase in V_s from 900 m/s above the BSR to 1100 m/s below. It should be noted, however, that the CDP gathers used in their impedance estimates had a limited aperture coverage up to a maximum incidence angle of 35°, and the impedance values were estimated using linearized Zoeppritz equations. The non-linear characteristics of the BSR amplitudes probably were not presented in the data and thus the V_s value might have been overestimated.

It can thus be suggested that the large increase in BSR reflection amplitude at far-offsets is primarily controlled by ΔV_p instead of $\Delta\sigma$. It is also noted that to generate the high amplitudes at large offsets, having turning rays produced by a velocity gradient above the BSR is not the only solution, as was suggested by *Hyndman and Spence* [1992]. However, velocities normally increase with depth, and with the presence of high velocity hydrates turning rays may occur that will enhance the far-offset amplitudes. It should also be emphasized that the single interface Zoeppritz equation provides only a rough guide to the BSR amplitude response. The BSR amplitude behaviour from models with velocity gradients, mode conversion, and thin layers may be different from the examples shown in Figure 4.16.

4.3.2 Single Interface Synthetic Seismogram Modelling

The analyses of seismic velocity and BSR reflection coefficients have shown that the BSR is at a sharp interface dividing sediment layers of different P-wave velocities. Figure 3.9 shows that a P-wave velocity decrease by 250-300 m/s occurs at the BSR. As discussed

above this velocity contrast could come from (1) normal water-saturated sediment overlying sediment containing free gas, (2) hydrate-bearing sediment overlying normal water-saturated sediment, or (3) a combination of the above. The AVO responses from various forms of these three velocity models have been investigated in this study with synthetic seismograms generated by raytracing and the Zoeppritz equations. Gradients of the model input parameters V_p, density ρ, and Poisson's ratio σ are approximated by thin homogenous layers and the layer interference effects are accommodated by thin layers of 0.25 m in thickness, much thinner than the 40-50 m wavelength of the zero-phase source wavelet. Selection of model velocity parameters for various hydrate or gas saturations are shown in Table 4.2 where V_s in hydrate-bearing sediment is allowed to increase from a reference value of 290 m/s in water-saturated sediment. Impedance contrasts at the BSR remain constant for all three models: (1) normal water-saturated sediment overlying sediment containing gas, or gas-only model, (2) sediment containing hydrate overlaying sediment with small amount of gas, or

Table 4.2 Input parameters for AVO modelling with different hydrate or gas saturations (V_p and V_s are given in m/s, and ρ is in Mg/m^3)

	normal	low-hydrate	high-hydrate	low-gas	high-gas
V_p	1700	1850	2000	1550	1400
V_s	290	420	550	290	290
ρ	1.9	1.9	1.9	1.9	1.9
σ	0.485	0.473	0.459	0.482	0.477

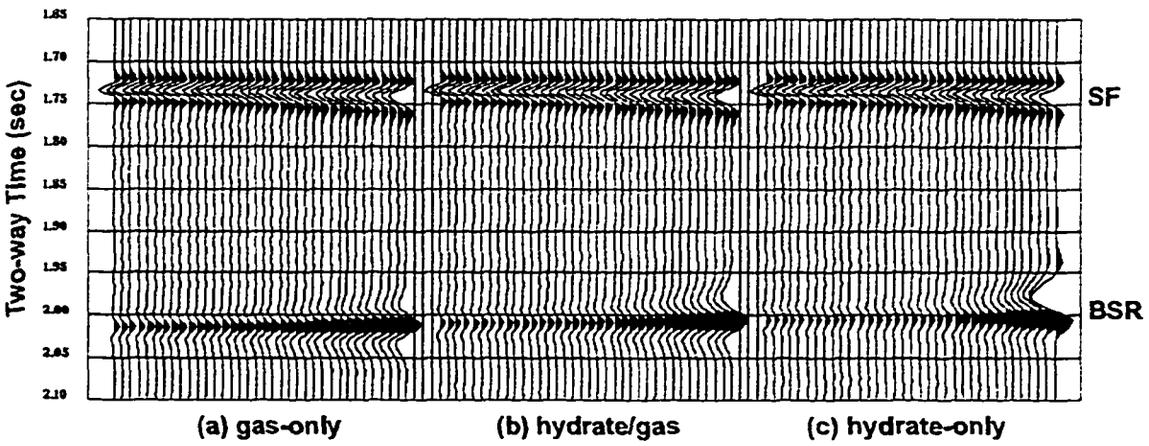

Figure 4.17 Synthetic CDP gathers generated by ray tracing and the Zoeppritz equations using an AVO modelling program from Hampson-Russell Software Service. Three different models are tested: (a) normal water-saturated sediment overlaying sediment containing gas, or gas-only model, (b) sediment containing hydrate overlaying sediment with small amount of gas, or hydrate/gas model, (c) and sediment with hydrate overlying normal sediment, or hydrate-only model. Impedance contrasts at the BSR remain constant.

hydrate/gas model, and (3) sediment with high hydrate saturation overlying normal water-saturated sediment, or hydrate-only model.

The synthetic seismograms generated from the above models are displayed in Figure 4.17. The reflection amplitudes at near offset are nearly the same since the impedance contrast is unchanged. There is a general trend of BSR amplitude-increase with offset, but the differences among different models are insignificant except for a phase rotation at the farthest offsets in the hydrate-only model associated with the turning rays due to the high hydrate saturation (Figure 4.17). Figure 4.18 displays the measured BSR peak amplitude values from three models. Amplitudes from the gas-only model increase nearly linearly with offsets at near-to-mid offsets in comparison to the other models. For the hydrate-only model,

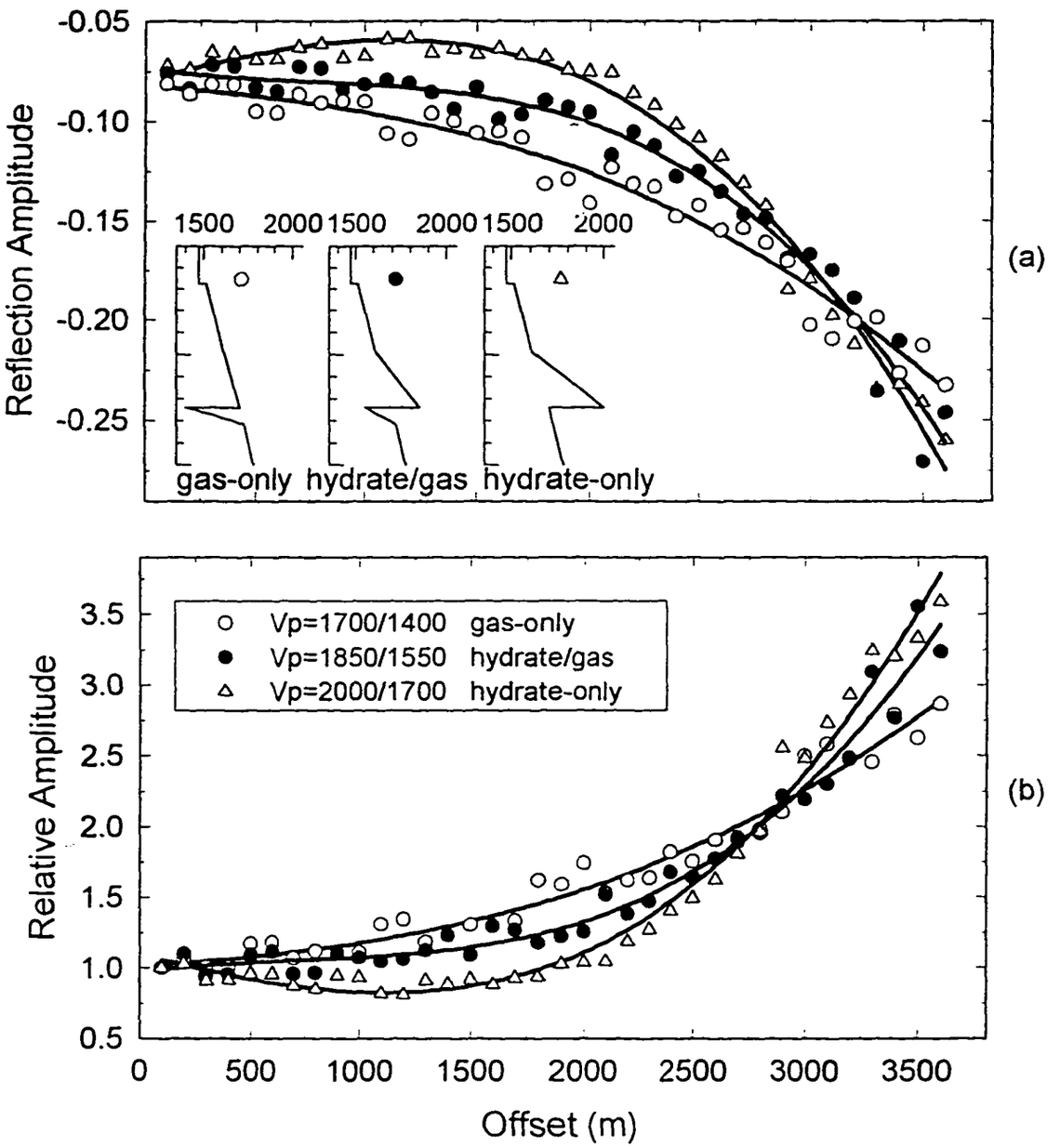

Figure 4.18 (a) Measured reflection amplitudes from synthetics in Figure 4.17 from the three BSR velocity models shown in the insets. (b) Reflection amplitudes normalized to a near offset value.

as the S-wave velocity above the BSR is increased by the hydrate to 550 m/s and there is a Poisson's ratio increase at the BSR, the amplitudes remain constant or slightly decrease at near-to-mid offsets and increase rapidly at far offsets. If there is no S-wave velocity increase above the BSR, a Poisson's ratio decrease will then produce higher amplitudes at mid-to-far offsets, similar to that shown in Figure 4.16. The hydrate/gas model shows an amplitude trend intermediate between the other two models, but when normalized to the near-offset amplitude (Figure 4.18b) the difference between the models is not significant considering measurement errors in real data, such as variations in receiver sensitivity and directivity, as well as in source strength. Both the hydrate/gas and hydrate-only models have an S-wave velocity increase and a Poisson's ratio increase at the BSR, resulting in a non-linear AVO response. The Poisson's ratio decrease at the BSR is small for the gas-only model, and the difference in amplitude response from different models is not as large as for the single interface models shown in Figure 4.16.

The AVO model results shown in Figures 4.17 do not include reflections from multiples or converted phases, but the conclusion is still valid that the small amplitude differences shown by AVO modelling are not diagnostic of different BSR velocity models. Especially, AVO analysis can not unambiguously distinguish between gas and hydrate/gas models as the cause of the BSR.

4.4 Conclusions

As seen in the discussions from the previous sections, the BSR is associated with a P-wave velocity change from either water-saturated sediment or high velocity hydrate-bearing

sediment to sediment containing zero or small amounts of free gas. Several additional conclusions can be drawn from the observed and modelled nonlinear BSR amplitude-versus-offset behaviour.

(1) The lateral BSR amplitude variability on a scale of one to several hundred metres is possibly due to variations in hydrate distribution, i.e., ranging from finely disseminated hydrate occupying sediment pore space to nodules of solid hydrate, as well as massive gas hydrate zone.

(2) A small amounts of hydrate above or free gas below the BSR do not have a large effects on the sediment density, so that the impedance contrast at the BSR is primarily due to a P-wave velocity change.

(3) An S-wave velocity increase probably exists above the BSR as the result of hydrate cementation. The nonlinear AVO character, constant or slightly decreasing amplitudes at near-to-mid offsets and a large amplitude increase at far offsets, can be reproduced in the model results if such S-wave velocity increase is assumed. Large amplitudes at far offsets can be produced by turning rays in the high velocity hydrate, but such turning rays are not necessarily required for large amplitudes.

(4) The large Poisson's ratio drop producing the linear amplitude increase in the standard AVO analysis is partly a consequence of a P-wave velocity decrease and an S-wave velocity increase in consolidated sediment rocks of different lithologies above and below the boundary. The contrast in Poisson's ratio at the BSR is likely small for water-saturated sediment, as small amounts of gas have little effect and there is no lithology contrast across the boundary. At the BSR, the non-linear amplitude behaviour suggests that the BSR

amplitudes are primarily the result of a P-wave velocity change and are less controlled by the a Poisson's ratio change because it is so small. In the standard AVO analysis, the gradient of amplitude-versus-offset has proven to be diagnostic of the presence of gas [e.g., *Shuey*, 1985]. This gradient however is not useful for quantitatively estimating Poisson's ratio contrasts in unconsolidated sediments.

(5) AVO modelling alone is not sufficient to distinguish different BSR velocity structure models, especially between impedance contrast mainly due to high velocity hydrate and contrast mainly due to low velocity underlying gas. The subtle differences in AVO behaviour from different models could possibly be detected through very careful full waveform inversion and with a well defined reference velocity representing water-saturated sediment unaffected by either hydrate or free gas.

CHAPTER 5 FULL WAVEFORM INVERSION OF GAS HYDRATE BOTTOM-SIMULATING REFLECTORS

The previous analyses of the BSR amplitude variations with offset or reflection angle used only the maximum wave amplitudes. additional information is contained in the detailed waveforms. Forward model fitting of waveforms would be very difficult and time consuming. However, several automated full waveform inversion schemes for multichannel seismic data have been developed [e.g., *Wood et al.*, 1994; *Hannay*, 1995]. The scheme used here has proven to be well suited to investigate the fine structure of velocity variations at and near the BSR [*Singh et al.*, 1993; *Minshull et al.*, 1994; *Singh and Minshull*, 1994]. This inversion technique tries to find a velocity-depth model such that the synthetic data produced by the model fit both the amplitude and waveform of the real data sample by sample, over all offsets in a full-fold CDP gather. *Singh et al.* [1993] and *Singh and Minshull* [1994] applied this waveform inversion to the MCS data near ODP Site 889. Their resulting velocity structure near the BSR was confirmed in general by the downhole logging and VSP data at the site but in detail it does not match either the MCS velocities and the downhole velocity data in the 100 m interval just below the seafloor, and the MCS data well below the BSR (as presented in Chapter 3). Additional waveform inversions, therefore, have been carried out using the recently available ODP well log and VSP data, as well as the large scale MCS velocity-depth function, to provide a better-constrained starting model for the inversion.

The inversion strategy consisted of a sample by sample minimization of a misfit function between real data and synthetic data by a nonlinear local search [*Singh et al.*, 1993;

Minshull et al., 1994]. A starting model was progressively modified during successive iterations to reach an optimal match between the data and the synthetics. The sophisticated inversion scheme is both computationally expensive and labour intensive and is thus limited to one-dimensional models and to approximately represent horizontally layered sub-surface structure. The inversion was implemented for L89-08 and L89-10 in the vicinity of the ODP Sites 889/890 on selected CDP gathers. BSR amplitude contour plots displayed in Figures 4.6, 4.7 and 4.10 guided the site selections. CDP gathers representative of different AVO characteristics were chosen at locations where the main reflectors, including the seafloor and BSR, are close to horizonal.

5.1 Inversion Data Preparation

Data preparation for the inversion included source wavelet designature, band-pass filtering, geometrical correction, source and receiver directivity correction, and transformation into τ-p (intercept time-slowness) domain and subsequently into ω-p (frequency-slowness) domain [e.g., *Minshull et al.*, 1994]. To avoid spatial aliasing in the τ-p transform, four adjacent CDP gathers were combined to give a 144-fold gather with a trace spacing of 25 m. Prior to the τ-p transform, blank traces were inserted at offset locations where the field data were incomplete due to recording failure.

The trace-to-trace amplitude variations due to varying source strength and receiver sensitivities were generally small, but are as high as 30% for a few traces (Figure 5.1). An attempt was made to remove these amplitude variations using a smoothed seafloor AVO response as a reference. Illustrated in Figure 5.1 are the measured and smoothed seafloor and

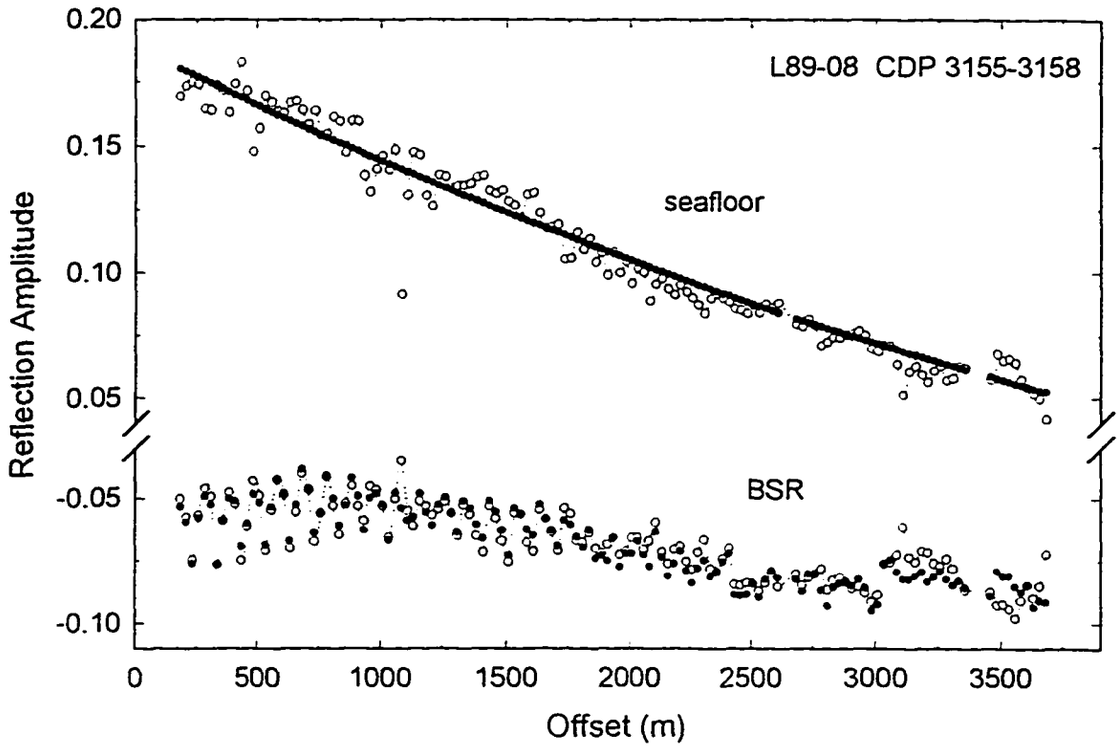

Figure 5.1 Measured seafloor and BSR peak amplitudes (open circles) showing the trace-to-trace variations due to varying source strength and receiver sensitivities. Smoothing the seafloor amplitudes provides a calibration reference to remove the variations. Solid symbols are the amplitude values with the variations removed at the seafloor and reduced at the BSR.

the measured and corrected BSR peak amplitudes. The seafloor amplitudes variations have been largely eliminated with the smoothing operation, but most of the BSR amplitude variations still exist. They thus must be due to causes other than source strength and receiver sensitivities.

5.2 Estimation of Source Wavelet

One of the most difficult and uncertain aspects of the inversion scheme is obtaining

an accurate estimate of the source wavelet. This can be approached in several ways, including the empirical estimate with auto-correlation of the seismic trace, if the actual wavelet is minimum phase and if the reflectivity of the subbottom structure can be treated as random and frequency independent [*Yilmaz*, 1987; *Sheriff and Geldart*, 1986]. Alternatively it can be obtained through deconvolution of the seafloor first multiple with the seafloor primary reflection [*Korenaga et al.*, 1996]. If the seafloor is assumed to be a simple interface across which only the density changes, then the seafloor reflection is simply a uniformly scaled version of the source. The seafloor reflection in the study area is, in most places, a single symmetrical zero-phase pulse, after the source wavelet designature has been applied. This behaviour is characteristic of a reflection from a simple interface (Figure 5.2). The MCS velocity data and the ODP Leg 146 log data have also shown that at the seafloor there is only a small velocity increase from 1465 to about 1520 m/s (see Figures 3.9 and 3.11) whereas there is a density increase from 1.02 to 1.72 Mg/m^3 (see Figure 4.11). Thus, the seafloor in the study area can be approximately treated as a density interface. The advantages of using the seafloor reflection to estimate the source wavelet include a generally high signal to noise level and any ghosting effects are automatically included in the estimate. The disadvantage of this approach is the inaccuracies due to the possible interference of reflections close to the water bottom with the source coda, and any velocity changes or gradient across the interface which produces a change in amplitude versus angle of incidence.

Figure 5.2 illustrates 12 near offset traces from a composite gather at CDP 3155-3158 on L89-08. Small trace to trace variations occur over an offset range of 183-458 m but they can be eliminated or reduced by summing the adjacent traces. The stacked trace shown on

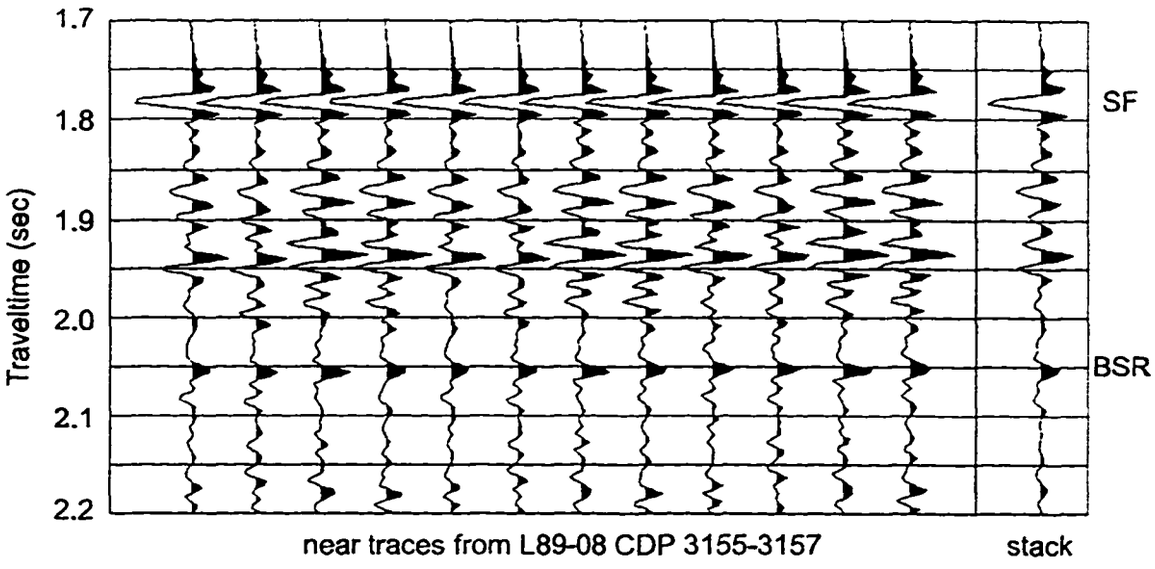

Figure 5.2 Source wavelet estimated from near traces at CDP 3155-3157 on L89-08. The near traces within an offset range of 183-458 m were stacked to eliminate small trace to trace variations. The stacked trace shown on the right was used to produce an offset-independent source wavelet.

the right in Figure 5.2 was used to extract the offset-independent source wavelet (Figure 5.3) for the subsequent inversion. In most cases, the BSR is clearly a simple reflection but the seafloor reflection is sometimes contaminated by the interference with later arrivals. Proper truncation of the seafloor reflection to avoid the interference

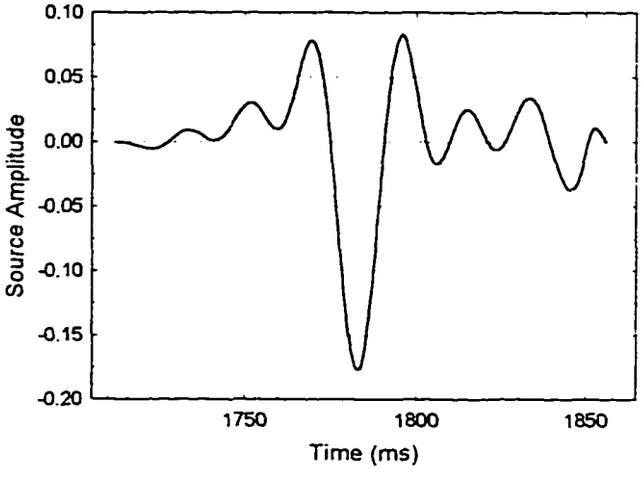

Figure 5.3 Example of source wavelet estimation from 12 traces at CDP 3155-3158 on L89-08.

which is not part of the source wavelet is important in obtaining a stable solution from the inversion.

The amplitudes of the seafloor reflection varied from location to location, and the waveform of both the reflected and transmitted phases also varied at some locations, possibly due to frequency dependent effects such as scattering and attenuation as shown in Figures 4.4 and 4.5. Thus, an individual source wavelet had to be estimated from each gather selected for the inversion.

5.3 Plane Wave Decomposition and Determination of Long Wavelength Velocity Structure

In the routine developed by *Minshull et al.*, [1994] and *Singh and Minshull* [1994], the long wavelength velocity structure has been estimated using a Monte Carlo search in the τ-p domain for layer velocities. This method has also been used at selected location for an initial trial in this study. As discussed below, a better starting model comes from the integration of the MCS and downhole velocities.

The τ-p mapping of seismic data is particularly useful for the 1-D inversion since it decomposes the medium response into a series of non-interacting cylindrical plane waves. Transformation into the τ-p domain was achieved using the exact Radon transform [*Chapman*, 1981]. Truncation artifacts due to the finite extent of the recording array were alleviated by tapering at near and far offsets prior to the transform. Figure 5.4 illustrates the result of the τ-p transform with slowness ranging from 0.01 to 0.55 s/km from a composite CDP gather at CDP 3286-3289 on L99-08. Both the seafloor and BSR reflections are strong

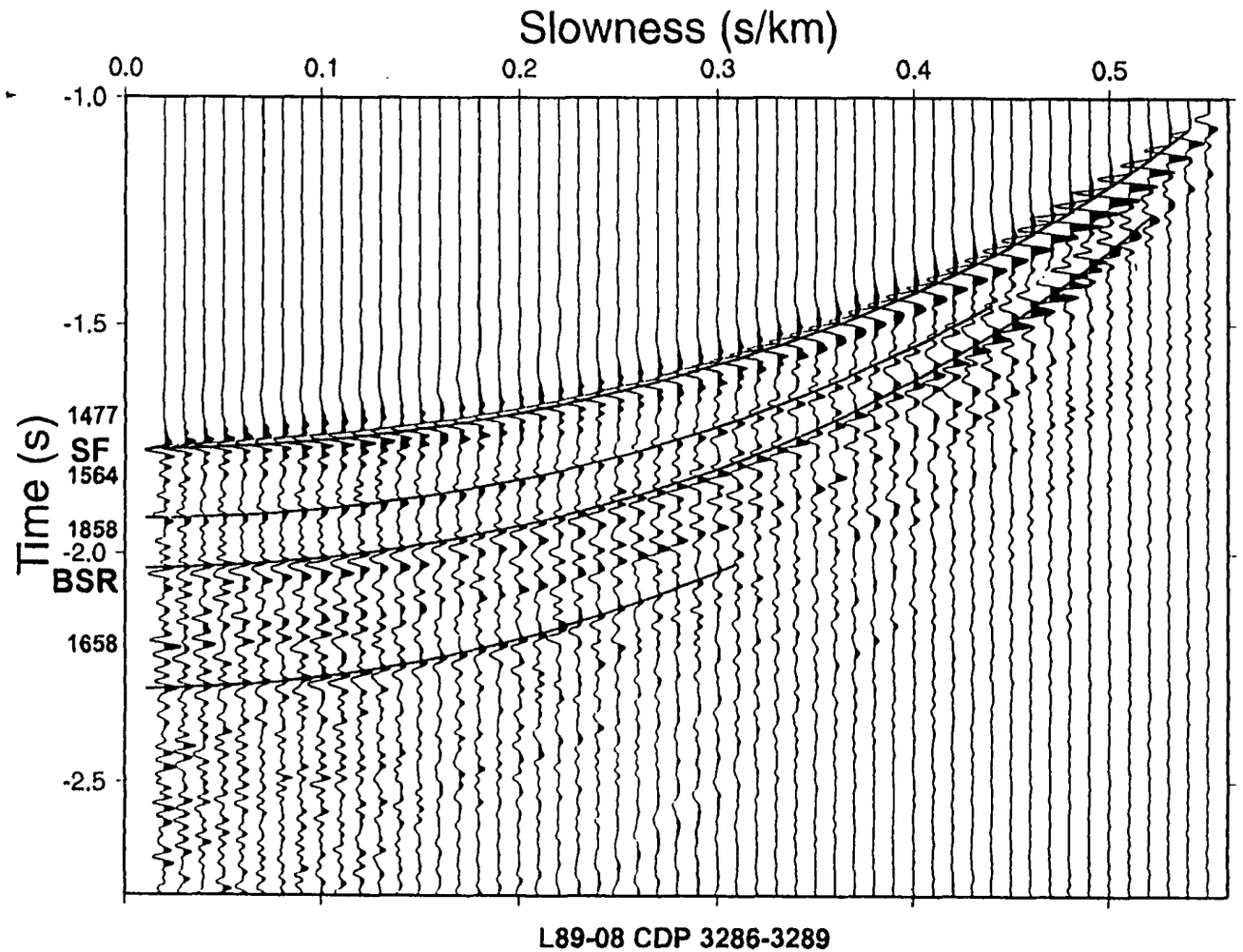

Figure 5.4 The τ-p transform of a composite CDP gather of L89-08 for the Monte Carlo velocity search. The final velocities determined from ellipses along four reflectors, including the seafloor and BSR, are listed on the left of the figure.

and there appear to be clear reflectors above and below the BSR.

For the first step of the inversion, typically four reflectors were picked to estimate an optimal long wave-length interval velocity model by maximizing the semblance coherent energy within a 60 ms time window centred along elliptical trajectories of the reflectors in the τ-p domain [*Minshull et al.*, 1994; *Singh and Minshull*, 1994]. For any given τ_o corresponding to a reflection arrival, *Singh et al.* [1991] defined the coherent energy $E[v(t_o)]$ as a function of velocity as

$$E[v(\tau_o)] = \int_{\tau_o}^{\tau_o + \Delta\tau} dt \left[\int dp\ u\left(\tau_o\sqrt{1 - v^2(\tau_o)p^2} - \tau_o + t,\ p\right)\right]^2, \qquad (5.1)$$

where $u(\tau, p)$ is the wave field, and $\Delta\tau$ is the length of the time window. For each τ_o within the time window, a grid search for RMS velocities ranging from 1400 to 2000 m/s was performed for each selected reflection. The velocity corresponding to the maximum energy is taken to be the RMS velocity at τ_o. From the resultant RMS velocity model, a primary interval velocity model with error bounds was calculated, and 50 initial models were randomly generated within the error bounds [*Minshull et al.*, 1994]. A Monte Carlo search [*Metropolis et al.*, 1953] was then performed with the initial models to find the maximum value of the total normalized energy along all the elliptical trajectories. After 100 iterations of the Monte Carlo search, the optimization was switched to a local search using the simplex method [*Nelder and Mead*, 1965] for faster convergence.

As an example (Figure 5.4), the four prominent reflectors chosen at CDP 3286-3289 are the seafloor, a shallow reflector below the seafloor near intercept time of 1.9 s at the lowest slowness, the BSR just below 2.0 s, and a deep reflector below the BSR at 2.25 s.

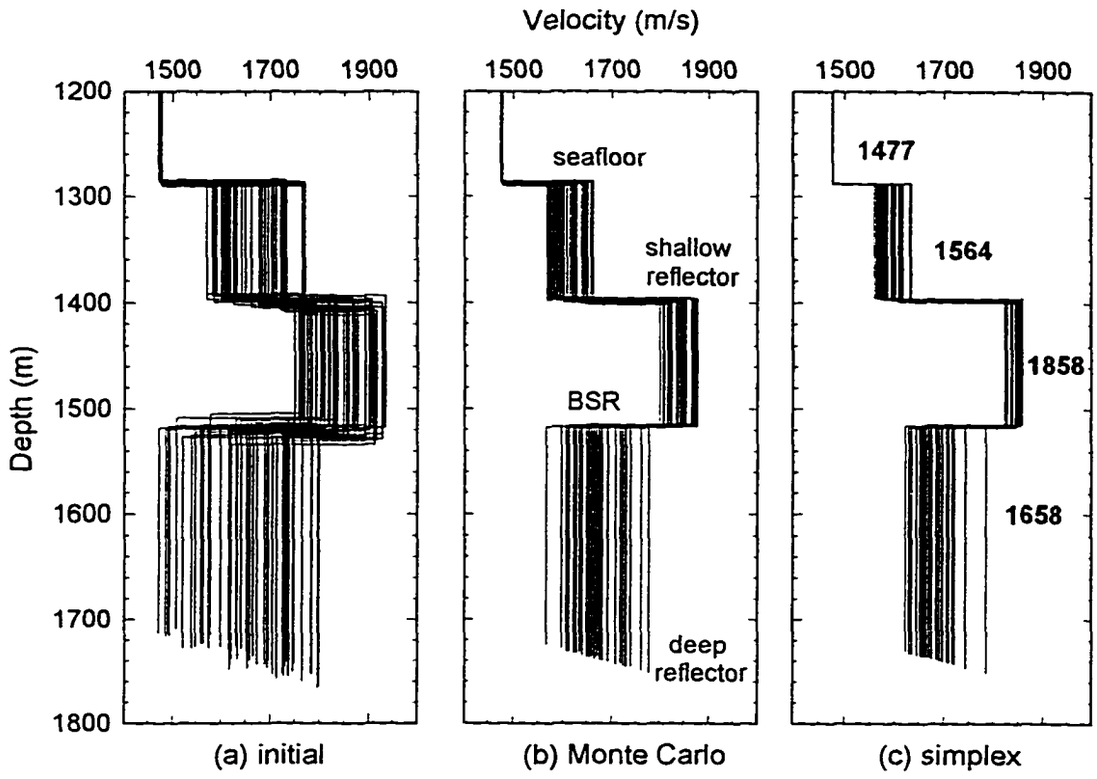

Figure 5.5 Interval velocity search results for L89-08 CDP 3286-3289 from (a) random initial model after a grid search, (b) 100 Monte Carlo iterations, and (c) simplex optimization. The final velocities for the four chosen reflectors also shown.

The two reflectors above and below the BSR are important in constraining the velocity structure around the BSR where large velocity changes are expected. To avoid reflection interference at large slownesses, the Monte Carlo search was performed only to a maximum slowness value of 0.44 s/km for the shallow reflector above the BSR and 0.31 s/km for the deep reflector below the BSR. Figure 5.5 illustrates the velocity convergence from the initial grid search, the Monte Carlo search, and the final simplex optimization processes. The initial models converged quickly to the four final velocities shown in Figures 5.4 and 5.5c. The elliptical trajectories determined by these final velocities are superimposed on the

corresponding reflectors shown in Figure 5.4. These velocities, representing long spatial wavelength velocity variations from the seafloor to the BSR and below, are in general agreement with the average layer velocities from the MCS data, the log data, and the VSP data presented in Chapter 3. The velocity increases from an average of 1564 m/s in the 100 m below the seafloor to an average of 1858 m/s in a 100 m interval above the BSR. The average velocity in the ~200 m interval below the BSR, where no hydrate is expected, is only 1658 m/s, much less than the velocity above the BSR. A smoothed version of the semblance velocities, consistent with the model derived from the Monte Carlo search, was used as an initial model for the waveform inversion (Figure 5.6).

5.4 BSR Full Waveform Inversion

The second step was the full waveform inversion in ω-p (frequency-slowness) domain to find the fine velocity structure [*Singh et al.*, 1993, *Minshull et al.*, 1994, *Singh and Minshull*, 1994]. A Fourier transform into the ω-p domain was applied and the data were resampled to 8 ms by discarding frequencies above 62.5 Hz to reduce the parameter space for the inversion. The synthetic seismograms from an initial long-wavelength velocity model were computed using the reflection transmission matrix method [*Kennett and Kerry*, 1979]. The method accurately treats multiples and mode conversion in the medium, and therefore includes all nonlinear effects. Starting from the initial velocity model, a nonlinear local velocity search using the conjugate gradient method [*Dietrich and Kormendi*, 1990] is performed by minimizing a misfit function defined as

$$S(\mathbf{m}) = \frac{1}{2} \|\mathbf{d}_{cal} - \mathbf{d}_{obs}\|_D^2 + \|\mathbf{m} - \mathbf{m}_o\|_M^2 , \tag{5.2}$$

where $\mathbf{d}_{cal}(\omega, p) = \mathbf{f}(\mathbf{m})$ is the calculated wavefield corresponding to the model $\mathbf{m}$ and $\mathbf{f}$ is the forward modelling operator, $\mathbf{d}_{obs}$ is the observed wavefield, and $\mathbf{m}_o$ is the initial model. The norms $\|\cdot\|_D^2$ and $\|\cdot\|_M^2$ are weighted L_2 norms defined as

$$\|\mathbf{d}\|_D^2 = \mathbf{d}^{*T}\mathbf{C}_D^{-1}\mathbf{d}, \tag{5.3}$$

and

$$\|\mathbf{m}\|_M^2 = \mathbf{m}^T\mathbf{C}_M^{-1}\mathbf{m}, \tag{5.4}$$

where $\mathbf{C}_D$ is the data covariance matrix, $\mathbf{C}_M$ is a priori model covariance matrix, the superscript T denotes the transpose of the matrix, and * denotes the complex conjugate. $\mathbf{C}_D$ and $\mathbf{C}_M$ were chosen as $0.5\mathbf{I}$ and $1.0\mathbf{I}$, where $\mathbf{I}$ is a unity matrix, so that the inversion is dominated by the data misfit and should be only weakly influenced by the starting model. The model parameters include P and S wave velocities, density, and P and S wave attenuations as functions of depth. Because P-wave velocities are considered to be the most influential parameter for the BSR amplitude behaviour and the starting models for S-wave velocity and density are less constrained, only P-wave velocities are updated by the conjugate gradient search.

In theory, the progressive constrained inversion scheme ensures convergence toward a global solution without exploring the entire model space, but in practice the actual convergence of the algorithm depends largely on the initial input model $\mathbf{m}_o$, so a good

estimate of $\mathbf{m}_o$ is essential for the success of the inversion. The smoothed version of the semblance velocities, consistent with the model derived from the Monte Carlo search discussed in the previous section, was discretized at 8-m intervals and used as an initial model for the waveform inversion. This starting model should be in the vicinity of the global solution. Figure 5.6 illustrates the initial velocity model and the MCS velocities, VSP velocities, and velocity result from the Monte Carlo search. In this starting model there is a small and gradual velocity increase at the seafloor from 1470 to 1560 m/s and a small velocity gradient to about 120 mbsf. A higher velocity gradient is introduced for the ~100-m-thick interval above the BSR where velocity increases to a maximum of 1868 m/s, preserving the traveltime from the seafloor to the BSR. Immediately beneath the BSR, velocity drops to 1615 m/s, subsequently increasing downwards with depth to follow the reference trend determined by the MCS velocities.

S-wave velocities and densities were calculated from the P-wave velocities using the empirical relations of *Castagna* [1985] and *Hamilton* [1978]. The densities at the seafloor were then modified to agree with the ODP density data at the seafloor (Figure 4.10) and to reproduce a seafloor reflection coefficient of 0.27, which was determined by comparison of the seafloor primary and multiple reflections in the previous chapter.

The final velocity model resulting from 10 iterations of the inversion (Figure 5.6) has velocities immediately below the seafloor generally increasing downward, that are only slightly greater than water velocity. The seafloor impedance contrast mainly comes from the density change from seawater to turbidite sediment. From ~120 mbsf to the BSR at 224 mbsf, the velocities are substantially higher than those of the sediments below the seafloor and

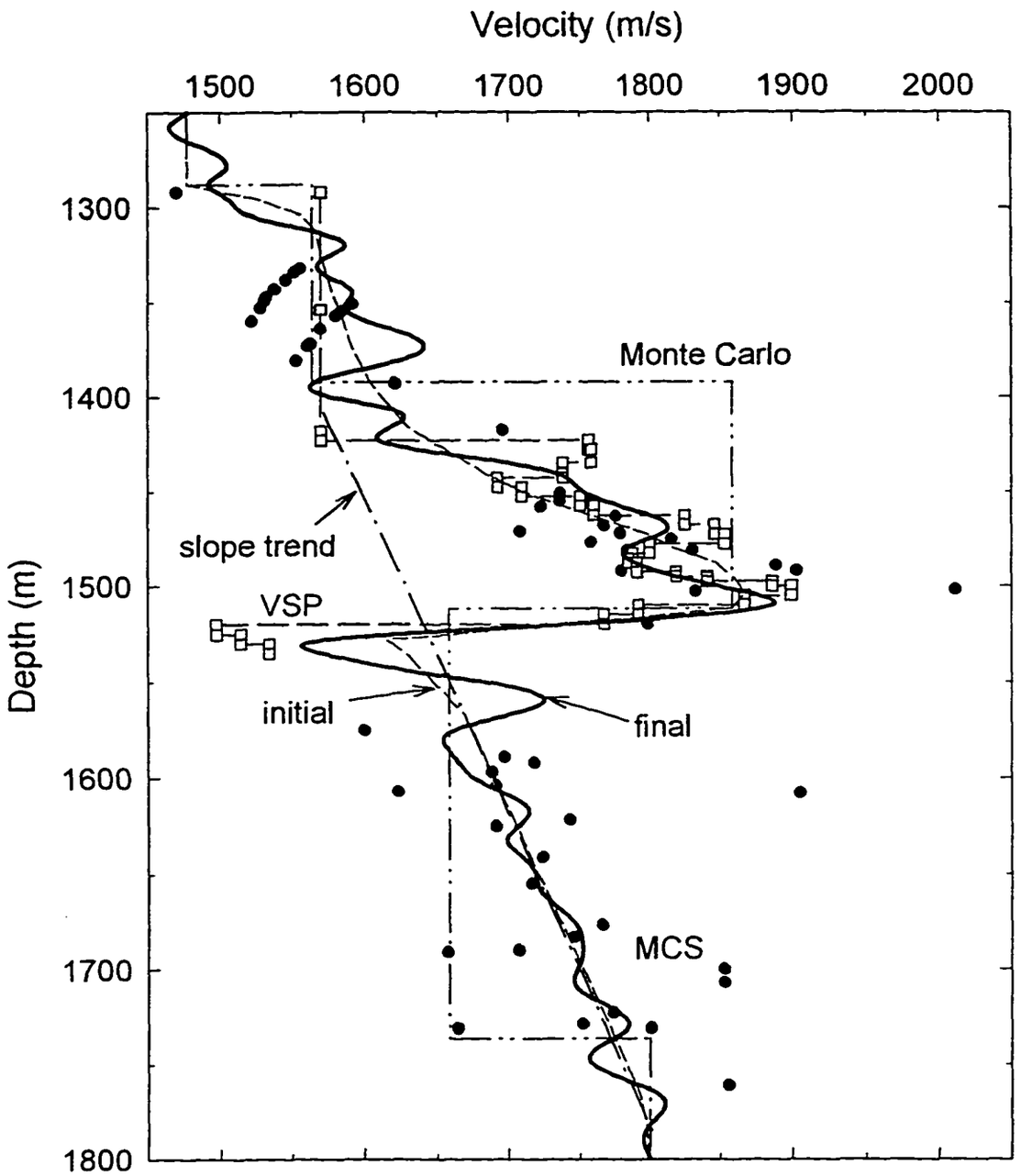

Figure 5.6 Comparison of velocity data near the BSR from (1) Monte Carlo search (thick dashed line), (2) starting model for the inversion (light dash line), (3) full waveform inversion (solid heavy curve), (4) MCS data (solid dots), (5) VSP velocities (dash line with symbols), and (6) no-hydrate reference velocity profile (dotted dash line).

below the BSR. In the ~100 m interval above the BSR, the match between the inversion result and the MCS semblance and VSP velocities is excellent, considering the uncertainties of the different techniques. At the BSR itself, the inversion gives a sharp decrease from a maximum velocity near 1900 m/s immediately above the BSR to a minimum of 1570 m/s just below the BSR, in an interval of ~25 m. Taken the reference velocity unaffected by the presence of hydrate or free gas as 1660 m/s at the BSR depth, the velocity drop below the BSR probably corresponds to a gas-bearing zone with a low gas saturation of 1-2%. Excellent waveform fit is achieved throughout the entire slowness range of the inversion (Figure 5.7). In this inversion result, the BSR is caused mainly by the velocity increase above the BSR and less by the velocity decrease below the BSR. The low-velocity layer bearing free gas beneath the BSR as resolved in the VSP data is too thin to be well resolved with the MCS velocity analysis. The gas layer also must have a transitional base which does not produce a seismic reflection. The waveform inversion is able to resolve the velocity contrast across the BSR but unable to provide reliable velocity information below the BSR except that there is a thin gas layer. Thus caution must be taken in using this method alone to infer whether the BSR impedance is primarily due to high-velocity hydrate or low-velocity free gas.

As discussed in Chapter 4, if the S-wave velocity above the BSR is not affected by the hydrate, a Poisson's ratio decrease will occur across the BSR, and this leads to higher reflection amplitudes at the mid to far offsets (Figure 4.16). Consequently, no large P-wave velocity contrast is required to model the BSR amplitudes as the increase in reflection amplitudes is accounted for by the Poisson's ratio contrast. This possibility was tested with a starting velocity model, referred to as constant-V_s model. In this model the S-wave

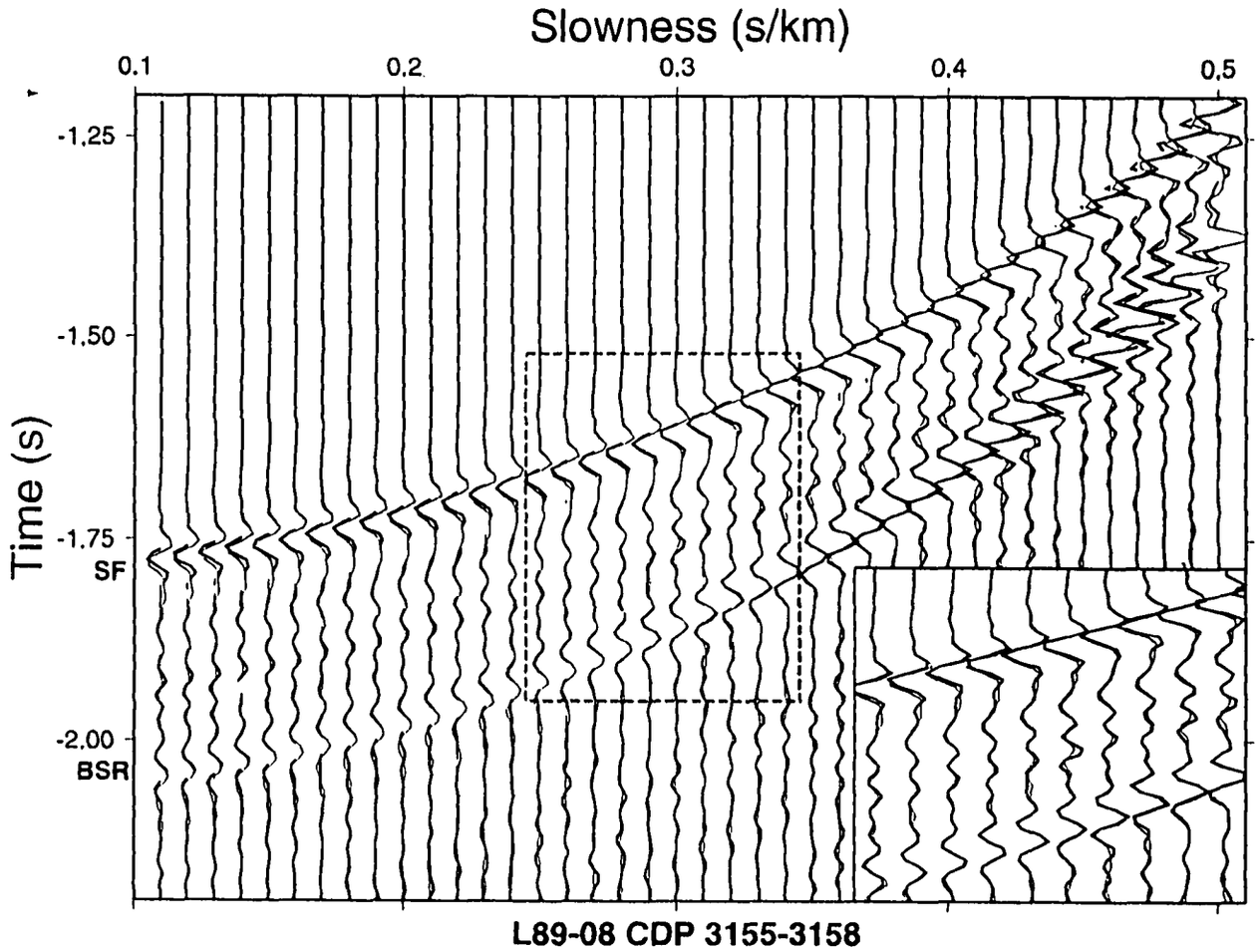

Figure 5.7 Waveform inversion results for L89-08 CDP 3155-3158. The seafloor and BSR reflections are very well matched by the synthetics (thin wiggle lines).

velocities increase only with depth and there is no V_s enhancement due to hydrate cementation above the BSR. All the other parameters remained the same as those in the previous starting model shown in Figure 5.6, referred to as the high-V_s model. The final P-wave velocity results from inversion of CDP 3155-3158 in the slowness range of 0.11-0.40 s/km are displayed in Figure 5.8. Although the waveform fit is not degraded in the modelled slowness range, the final velocities from the constant-V_s model show a slightly smaller P-wave velocity contrast at the BSR in comparison with the velocities from the high-V_s model. This V_p difference illustrates the trade-off between P-wave velocity contrast and S-wave velocity contrast at the BSR. For the reflection amplitude character at the BSR, both P-wave velocity increase and S-wave velocity decrease above the BSR will result in an increase in Poisson's ratio contrast and produce nearly the same AVO effect up to the mid offset range. At the far-offset range, however, reflection amplitudes depend more on the P-wave velocity contrast and require higher P-wave velocities than those from the constant-V_s model.

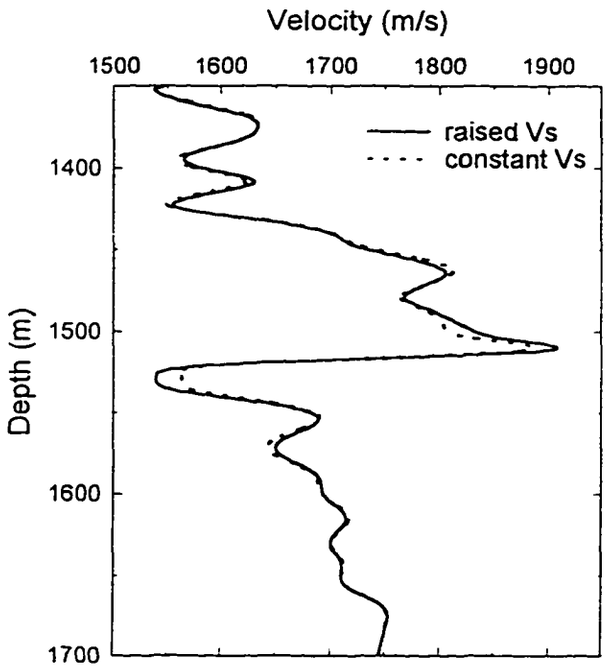

Figure 5.8 Final inversion velocities from two starting models with differing V_s structure above the BSR. A reduced V_p contrast is produced from the model with no V_s increase above the BSR.

5.5 Sensitivity of Inversion Solution

To quantitatively address the question whether the BSR impedance contrast is primarily due to high-velocity hydrate or low-velocity free gas, and to inspect the reliability of inversion result, a series of inversion tests were run. The initial velocities in the vicinity of the BSR were replaced with three different possible models. The starting model in Figure 5.6 and Figure 5.9a assumes that the BSR is caused by hydrate-bearing sediment overlying sediment containing a small amount of free gas. Three alternative starting models based on this hydrate-over-gas model are: (1) gas-only model which reduces the velocity above the BSR to 1770 m/s and the minimum velocity below the BSR to 1456 m/s (Figure 5.9b), (2) no-gas model which increases the low velocity below the BSR to the no-hydrate/no-gas reference value of 1660 m/s (Figure 5.9c), and (3) no-hydrate/no-gas model in which velocities increase smoothly with depth with no velocity contrast at the BSR. The average velocity below the seafloor in the no-hydrate/no-gas model is increased to preserve the observed traveltime from the seafloor to the BSR (Figure 5.9d). S-wave velocities above the BSR in the gas-only and no-hydrate/no-gas models were adjusted in accordance with the modified P-wave velocities. All the other parameters, including slowness and depth ranges for the test inversions, were kept the same as those for the hydrate-and-gas model in Figure 5.9a. Figure 5.9 displays the final velocity results from the four different initial models. Although the differences of the BSR velocity structures are quite significant in the starting models, the general features of the final velocities, (a)-(c) in Figure 5.9, are very similar and agree with the other velocity determinations very well: a maximum velocity above the BSR near 1900 m/s, a ~25-m-thick low velocity zone with a minimum velocity of ~1550 m/s. Final

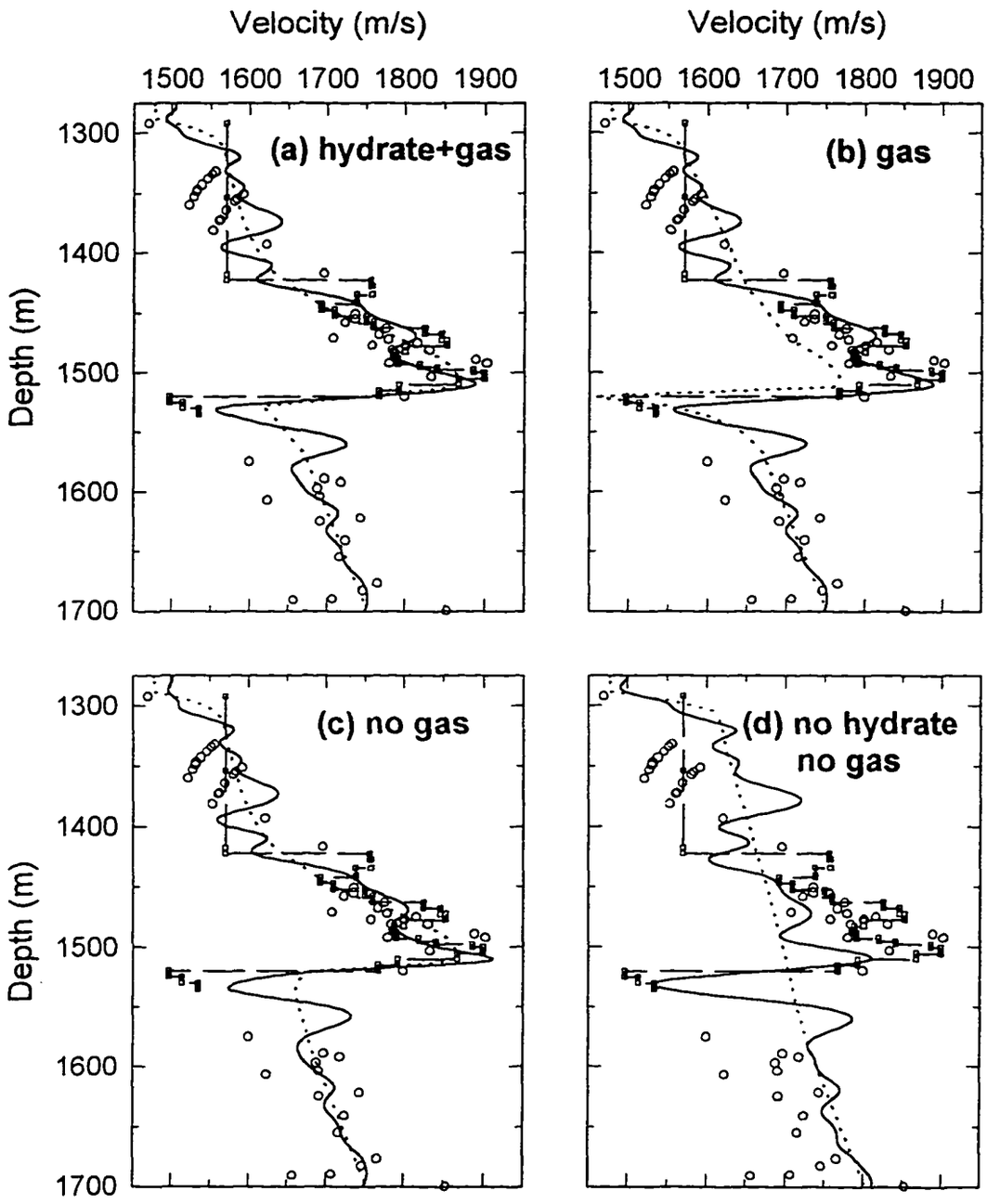

Figure 5.9 Inversion final velocities (solid lines) from different starting models (dashed lines). (a) hydrate-over-gas model in which the BSR is caused by hydrate-bearing sediment overlying sediment containing small amount of free gas. (b) gas-only model which has a minimum velocity of 1456 m/s below the BSR, (c) no-gas model which removes the low velocity below the BSR, and (d) no-hydrate/no-gas model which allows no velocity contrast at the BSR. Velocities from MCS (open circles) and VSP (dashed lines with symbols) are also shown.

results from the gas-only model correctly predicted the downhole and semblance velocities above the BSR, but did not produce velocities less than 1550 m/s below the BSR. Values of the inversion misfit functions, defined in equation 5.2 and measured over the entire slowness range for the inversion, are shown in Figure 5.10. The misfits of all three starting models with a P-wave velocity contrast at the BSR were initially slightly different, but after 3-4 iterations they were all similar, below 150 (Figure 5.10). The no-hydrate/no-gas model, however, had a very high initial misfit of 550 as expected, because the initial model was far from the long-wavelength velocity structure defined by the Monte Carlo search and other data. The inversion failed to reduce the misfit to the same level achieved with the other three starting models. From this latter starting model, the final velocities in Figure 5.9d have an especially low velocity of ~1520 m/s below the BSR and an insignificant velocity increase above the BSR relative to the reference. This model result is similar to that presented by *Singh et al* [1993] and *Singh and Minshull* [1994] using an initial model with no

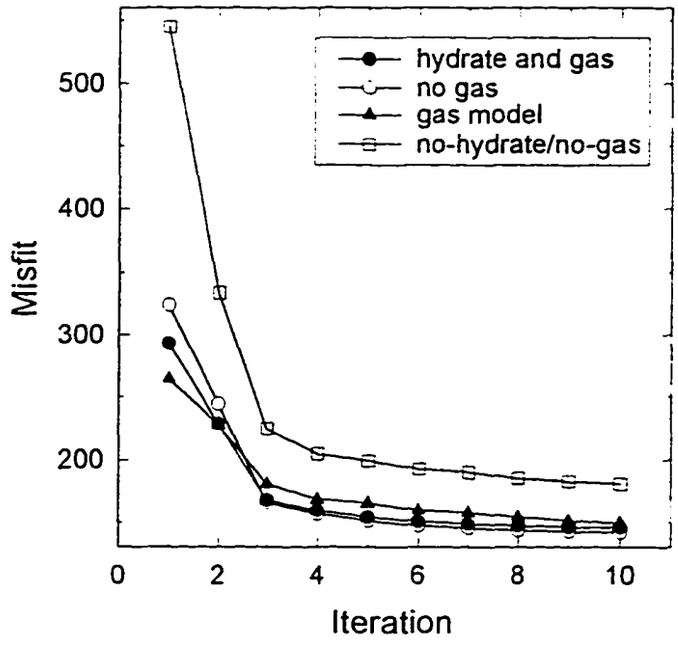

Figure 5.10 Misfit function versus number of iterations during the inversion for models shown in Figure 5.8.

velocity contrast at the BSR depth. From this model result they concluded that the BSR was caused mainly by free gas.

The above tests clearly demonstrate that the non-linear search of the inversion is robust enough to find the final solution representing a global minimum regardless of the detailed velocity structures at the BSR depth, provided a long-wavelength velocity structure in the starting model is adequately defined. A long-wavelength velocity profile, that includes a high velocity layer above the BSR and a velocity decrease below as determined by the MCS semblance and VSP data, is essential for the inversion to converge to the global solution with minimum misfit. Without such long-wavelength velocity information, the inversion is still able to resolve the velocity contrast at the BSR, but the absolute velocities above and below the BSR may not be correct. From the inversions shown above and the reference velocity profile defined in the previous chapters, it is clear that the data require both the high velocities above the BSR, representing sediment pore spaces partially filled with hydrate, and the low velocity zone immediately below the BSR, representing sediments containing a small amount, 1-2%, of free gas.

5.6 Inversion at other locations

For a quantitative comparison of the detailed BSR velocity structures at different locations, the above inversion procedure was carried out at two other sites, CDP 2110 from L89-10 and CDP 3286 from L89-08. The selection of these gathers was based on the representative seafloor and BSR amplitude characteristics shown in the AVO contour plots of Figures 4.4 to 4.10. Figure 5.11 displays the three CDP gathers and the measured seafloor

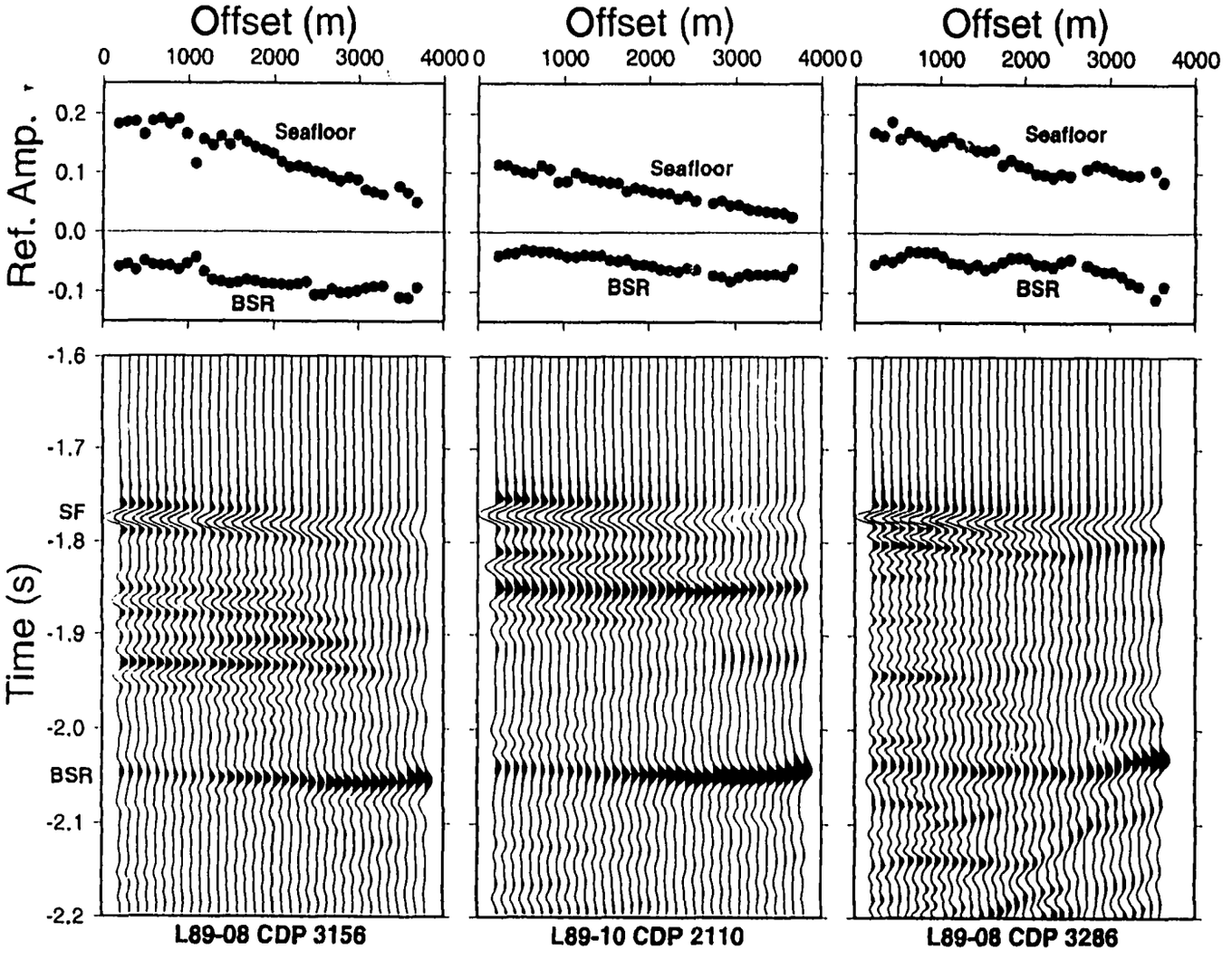

Figure 5.11 Variations of seafloor and BSR amplitudes with offsets from three locations, CDP 2110 on L89-10, and CDP 3156 and 3286 on L89-08. No directivity correction was applied.

and BSR reflection amplitudes. The seafloor reflection scattering near CDP 3200 on L89-08 (Figure 3.4) results in reduced seafloor reflection amplitudes as evident in Figures 4.3 and 4.4. L89-10 intersects L89-08 near the topographic high shown in Figure 3.4 and thus the overall seafloor reflection amplitudes at CDP 2110 are not as high as those from the other two sites on L89-08. However, regardless of the different overall reflection strength, the AVO characteristics for the seafloor reflection at the three sites are consistently similar with decreasing amplitudes towards far offsets (Figure 5.12). The only exception is at CDP 3286

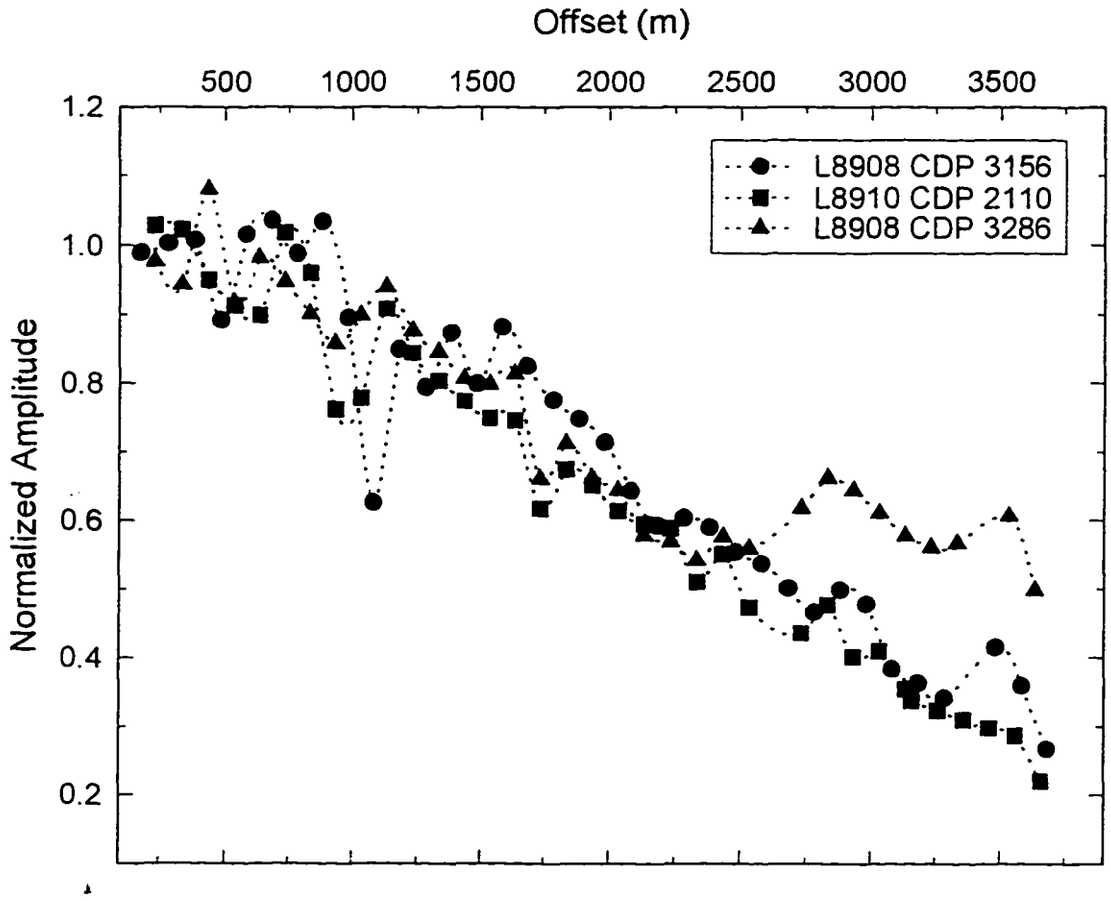

Figure 5.12 Seafloor reflection amplitudes-versus-offset from three CDP gathers for the inversion. The measured amplitudes are normalized to a constant value at near-offset.

where the seafloor amplitudes at far offsets are contaminated by the interference with other arrivals (Figure 5.11).

There also exist small trace-to-trace variations in reflection amplitudes within each gather, resulting from varying source strength and receiver sensitivities. To characterize the BSR amplitude variations with offset and to compare the AVO behaviour at different locations, a method of data analysis similar to that of *Chiburis* [1984, 1993] was used. The characterization of BSR amplitude behaviour uses target and reference horizons to eliminate or greatly reduce amplitude effects from causes other than offset. In *Chiburis's* method of AVO analysis, a reference horizon is chosen over which no offset-dependent amplitude effects are expected. However, if the assumption can be made, such as suggested in Figure 5.12, that the amplitude behaviour remains the same from site to site, the seafloor reflection can still serve as a reference to compare offset-dependent amplitude effects at the BSR. Therefore, amplitude ratios between the seafloor and BSR reflections are plotted at each offset in Figure 5.13a. With the seafloor reflections as a reference, the displayed BSR relative amplitudes do not represent the actual AVO response, since they incorporate the relative amplitude variations of the seafloor, but the trace-to-trace amplitude variations are largely eliminated and the comparison among CDP gathers can be made easily. The overall seafloor reflection amplitudes vary at different CDP locations, but the BSR reflection amplitudes at near offset from all three gathers are consistently about 30% of the seafloor reflection (Figure 5.13a). There is a large difference in the rate of BSR amplitude increase with offset, CDP 2110 has significantly higher far-offset amplitudes.

CDP 2110 is located at the apex of a sub-surface anticlinal feature possibly caused by

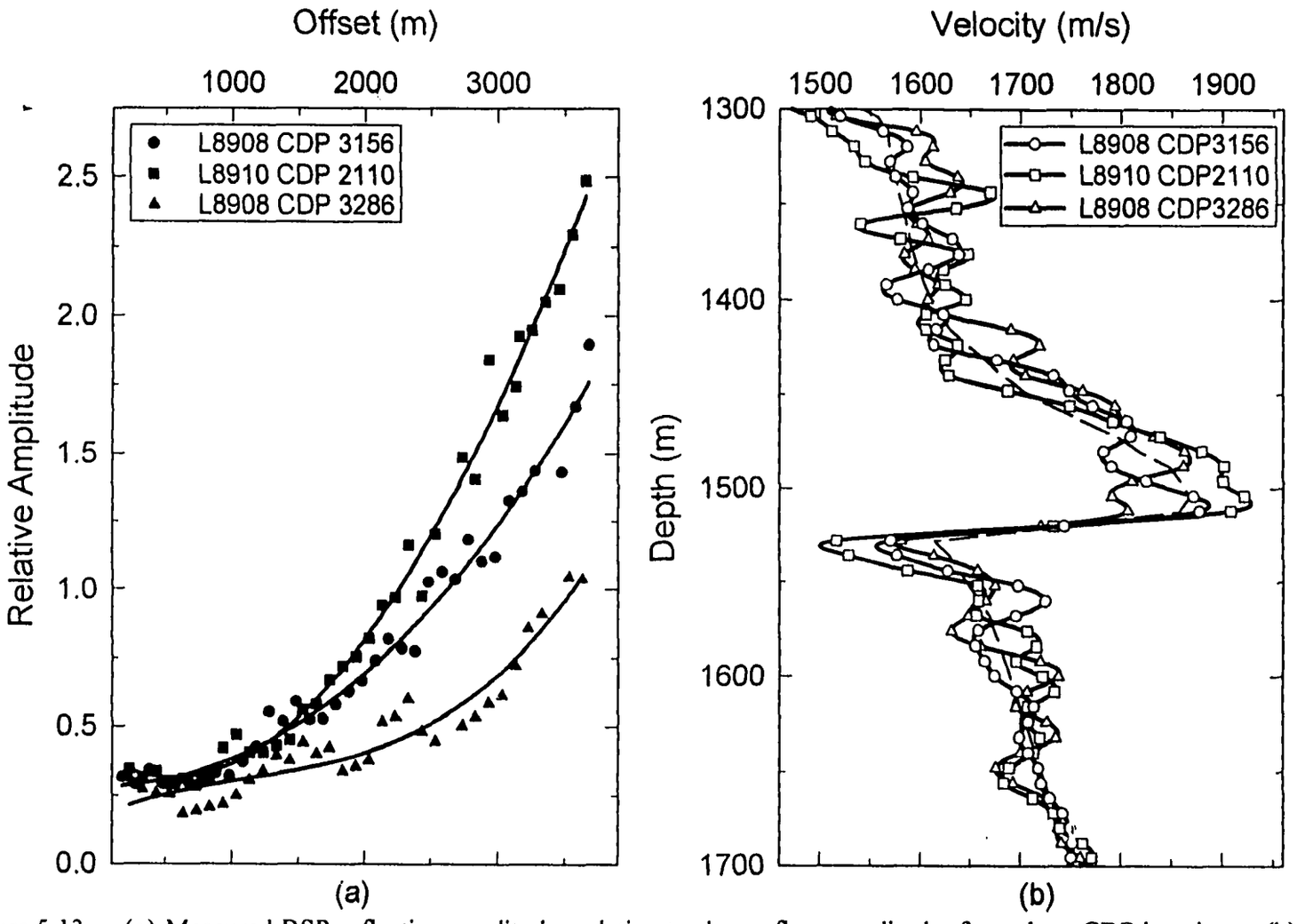

Figure 5.13 (a) Measured BSR reflection amplitudes relative to the seafloor amplitudes from three CDP locations. (b) Final inversion results from the three composite CDP gathers on L89-08 and L89-10. The starting model for the inversion is shown by thin dashed line.

tectonic folding and uplifting (Figure 3.4). Both the seafloor and the BSR reflections are sub-horizontal, but the reflectors forming the anticline dip steeply and cut through the BSR on the flanks of the structure. The BSR at this location is particularly strong and continuous on the migrated section (Figure 3.4), and the BSR relative amplitudes increase more rapidly with offset (Figure 5.13a). The significant AVO effect at this location suggests that free gas might have been trapped by the anticline or that the rapid uplift at this location has caused an unusual degree of hydrate dissociation. The reflection from the top of the anticline at ~1.85 s (see the CDP gather in Figure 5.11), intermediate between the seafloor and the BSR reflections, is strong and it probably represents a density change as the reflection amplitudes decrease with offset.

CDP 3286 lies near the seafloor topographic high on L89-08 (Figure 3.4), where the seafloor and BSR reflection amplitudes may have been affected by both the seafloor focussing effect and the interference from other arrivals. The BSR amplitudes at far-offsets are high as shown in Figure 4.6 and 4.7, but the amplitude ratio between the BSR and seafloor reflections are much lower compared with other two sites (Figure 5.13a).

Given the same initial model as shown in Figure 5.6, the waveform inversion was repeated on the gathers at CDP 2110 and 3286. Figure 5.13b compares the resultant final velocities from the three sites, and Figure 5.14 displays the waveform fit between the real data and the synthetics generated by the final models from CDP 2110 and 3286. At CDP 2110, velocities below the seafloor are higher than the regional values due to the strong reflections from the top of the anticline, but the average velocity in the 120 meter interval below the seafloor is similar to values at the other two sites. Overlying the BSR at this location,

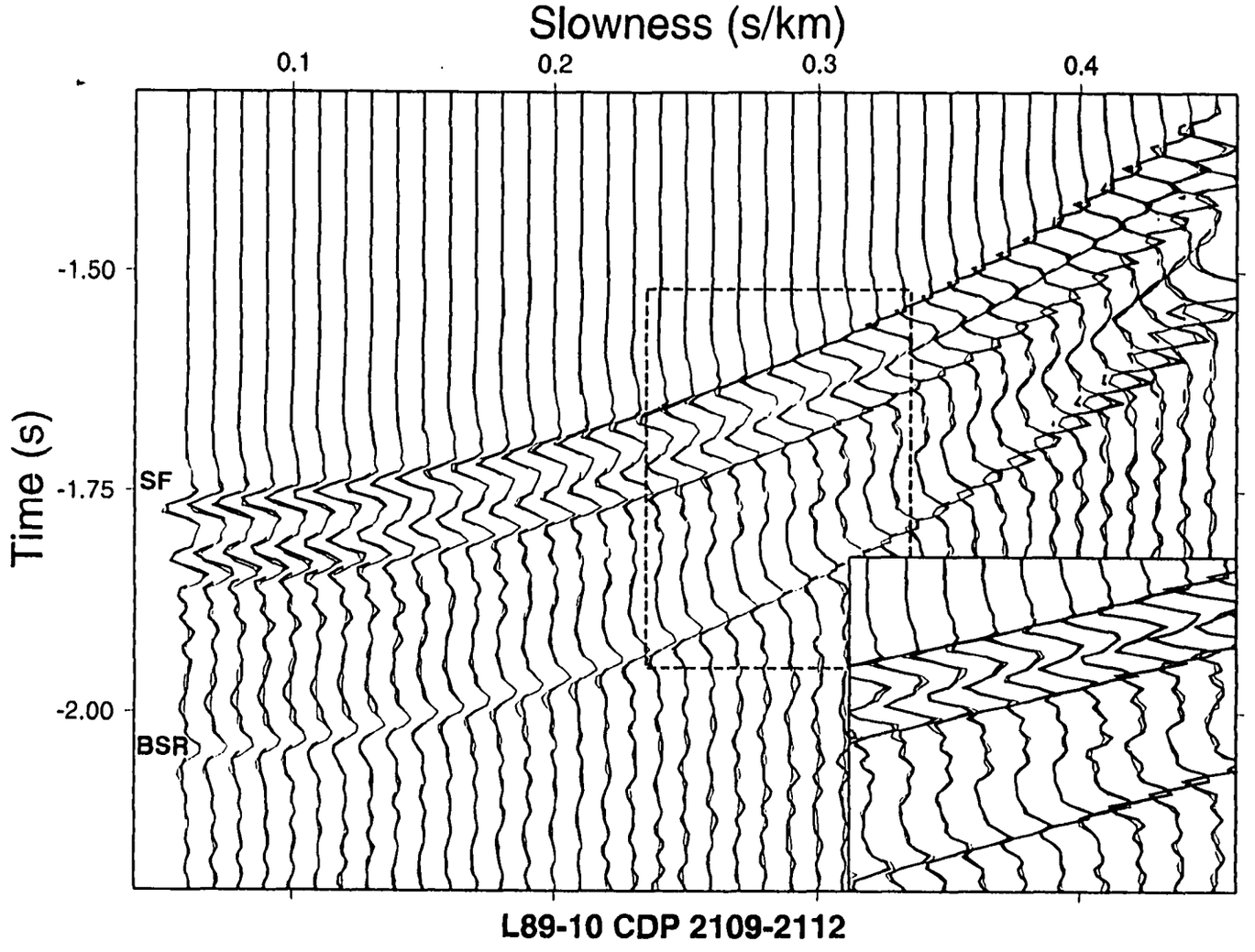

Figure 5.14 Waveform inversion results for CDP 2109-2112 from L89-10 and CDP 3286-3289 from L89-08. Synthetics from the final inversion model are shown with thin wiggle lines.

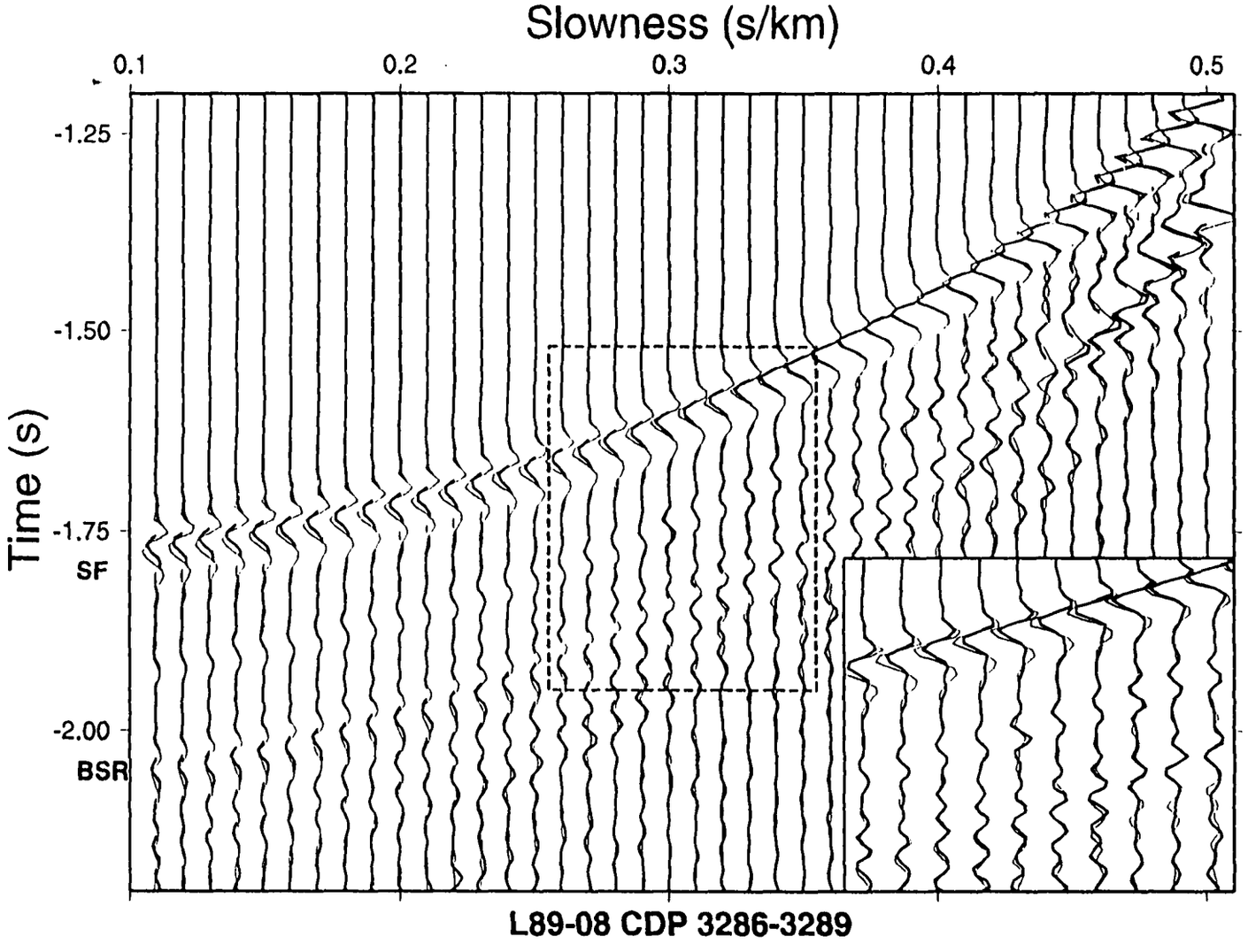

Figure 5.14 Continued.

significantly higher velocities are required for the entire ~100-m-thick section . A sharp velocity drop from 1920 m/s to a minimum of 1520 m/s has made this site distinctive as having the largest velocity contrast at the BSR. Velocities below the BSR stay low in the depth interval of about 40 meters. Although these velocities are not as tightly constrained as the velocities above the BSR, they probably represent a low velocity zone associated with gas trapped below the anticline.

The agreement between the real data and the synthetics at CDP 3286 (Figure 5.14) is not as good as from the other two sites, largely due to the interference at the seafloor and thus the inaccuracy of the source wavelet from the seafloor reflection. The resultant inversion velocity model includes a high velocity zone above the BSR, but not as high as from the other sites. At the BSR the data do not require as large a velocity change as the other sites. The velocity below the BSR is ~1580 m/s, similar to the value obtained at CDP 3156. The offset-dependant amplitudes displayed in Figure 4.6, 4.7, and 5.11 show noticeable AVO response at the BSR, but the detailed BSR velocity structure revealed by the quantitative inversion analysis indicates that the velocities above the BSR are less enhanced at CDP 3286 where the velocity immediately above the BSR is no more than 1800 m/s. The relatively small P-wave velocity contrast at the BSR resulting from the less substantial AVO response may therefore suggest a low hydrate concentration at this location.

5.7 Conclusions

Using the full waveform inversion, a high-resolution velocity model for the hydrate BSR has been derived at three sites. The best-fit model for the MCS data near the ODP Sites

889/890 consists of a high-velocity zone above the BSR and a thin low-velocity layer below. The high-velocity zone has a thickness of ~100 m and the velocities increase downward to a maximum of about 1900 m/s or more just above the BSR, indicating a downward increase in hydrate concentration to the base of the stability field. The low velocities beneath the BSR probably represent the presence of free gas in a thin layer of 25-50 m thick. The low velocities coincide well with very high headspace methane concentrations measured at Site 889 just below the BSR [*Whiticar et al.*, 1995; *Whiticar and Hovland*, 1995]. The disagreement between MCS semblance velocities and the VSP data below the BSR is probably due to the thickness of the gas layer which is too thin to be resolved by the MCS data. The maximum velocity contrast at the BSR has been detected at an anticlinal feature and the minimum velocity is only 1520 m/s. The inversion results determined by the substantial offset-dependent amplitude behaviour at this location may also suggest increased saturations of both hydrate and free gas possibly associated with the local structural feature.

An initial model well constrained by the MCS velocities, ODP logging data, VSP measurements, and long wavelength velocities from the Monte Carlo search, proved to be essential for accurately defining the velocity structure near the BSR. A priori information for the inversion from this initial model ensures that the nonlinear local search starts in the close vicinity of the best final solution. Inversions with alternative BSR velocity models have shown that a good fit between the data and the model synthetics can be achieved provided the initial model has an approximately correct P-wave velocity contrast at the BSR. The inversion is capable of deriving a velocity structure explaining some parts of the data not in the initial model, but a priori velocity information from the initial model is a necessary

prerequisite for the best inversion result.

The velocity profile, defined by the MCS velocity data from below the seafloor to depths of several kilometres and constrained by the ODP borehole data in the logged interval above the BSR, also provides an important reference in determining the cause of velocity changes at the BSR. The velocities in the ~100 m interval below the seafloor represent the unconsolidated slope sediment, but the velocities in the ~100 m section above the BSR have been raised substantially by the hydrate concentration. From the final inversion results, the BSR appears to come from both hydrate and free gas saturations above and below the BSR. Most of BSR impedance contrast in the MCS data results from the velocity enhancement by the hydrate saturation and the rest from the velocity decrease due to the thin layer with 1-2% free gas below the BSR.

CHAPTER 6 DISCUSSIONS AND CONCLUSIONS

An extensive seismic study on the northern Cascadia accretionary prism off Vancouver Island has included investigations of regional velocity variations and detailed analyses of the hydrate BSR velocity structure. The velocity structure and the inferred porosity variations across the frontal region of the accretionary prism have been quantitatively assessed by a detailed seismic velocity analysis. An estimate of fluid expulsion rate near the deformation front is thus made. In the lower slope region near the ODP Sites 889/890, a reference velocity profile has been established from the detailed semblance velocity analyses of the MCS data, combined with the previously published ODP sonic log and VSP data. Sediment velocities of the slope region increase downward more rapidly than the no-hydrate/no-gas reference profile from about 1500 m/s near the seafloor to a maximum of 1900 m/s or more just above the BSR. From the full waveform results, the velocities immediately below the BSR drop to ~1550 m/s, probably representing a thin layer containing free gas. The difference between the reference and observed velocities can be used to estimate hydrate concentration in the pore space above the BSR.

6.1 Summary of Conclusions

In this integrated study, the sediment consolidation processes and pore fluid expulsion patterns inferred from the regional velocity analysis has provided important insight in the understanding of a well developed hydrate BSR in the northern Cascadia accretionary prism.

Some important conclusions from this study are summarized below.

(1) Within the Cascadia basin sediments approaching the deformation front, and within the frontal thrust zone of the accretionary prism, sediment velocities are observed to increase and the inferred porosities decrease substantially landward. This velocity increase is due to an increase in tectonic stress that consolidates the sediments in the initial stage of sediment accretion. An important conclusion from results of the regional velocity analyses is that more than one third of the pore fluid content of the incoming sediment is lost by the time they are incorporated into the accretionary prism, i.e., low-to-mid continental slope.

(2) The rapid thickening of the accretionary prism landward of the deformation front results in an underconsolidated sediment section. Velocities of the slope sediments are significantly lower relative to those in the undeformed sequence of Cascadia Basin at comparable sub-bottom depths. The inferred porosities in the lower slope region suggest that there is no large amount of pore loss in the slope sediments.

(3) The fluid flow in the frontal region of the accretionary prism plays an important role in carrying methane upward into the hydrate stability zone. In the lower-to-mid slope region where the sediment section is thickened rapidly, migration of the hydrate stability field and the consequent hydrate recycling may be responsible for sharpening the base of the hydrate layer. This process concentrates the hydrate above the BSR and creates a low-velocity gas zone below the BSR to form a strong and continuous BSR over much of the slope region.

(4) The multichannel, downhole log, and VSP velocity-depth profiles are in excellent agreement where they overlap from the seafloor to the depth of BSR. At ODP Sites, the

clear velocity increase above the BSR is due to sediment containing hydrate with a maximum concentration of ~20%. A low-velocity layer associated with free gas of 1-2% concentration below the BSR is also suggested by the VSP data and velocity inversion result.

6.2 Mechanisms for Gas Hydrate Formation in the Accretionary Prism

A prominent BSR becomes visible immediately landward of the deformation front in the accreted sediment, and is evident over much of the low-to-mid continental slope in a zone of more than 30 km wide parallel to the margin. As discussed in Chapter 3, the upward pore fluid migration is believed to play an important role in the formation of a gas hydrate BSR. Direct evidence of such fluid migration is also provided by substantially elevated near-surface bacterial populations. At the ODP sites on Cascadia margin, bacterial populations and activity have indicated active fluid venting in the sediment section [*Cragg et al.*, 1995]. From the estimated fluid loss of 35% over the 3-km-thick Cascadia Basin sediments with an average initial sediment porosity of 30% (see conclusion in Chapter 2), the quantity of the expelled fluid reaches 315 m^3/m^2 over a distance of 12 km before the basin sediments are incorporated into the accretionary prism. Assuming that 100 mmol/L of methane is removed from the expelled fluid as it moves into the stability field, a 90-m-thick layer with hydrate in an average saturation of 10% of the pore space can be formed by the rising fluids.

Other important mechanisms in the accretionary prism contributing to the hydrate concentration above the BSR include temperature change over geological time and pressure change from sediment deposition and tectonic uplift. As the sediment section grows rapidly upward in the frontal region of the accretionary prism, the base of the stability field migrates

upward to follow the new pressure and temperature condition. One such example can be found on L89-08, where the first occurrence of the BSR is near the deformation front at CDP 4550 (Figure 3.3). The BSR at this location, where water depth is about 2300 m, is at ~400 m below the seafloor. Landward from this site to the lower slope region where water depth decreases to ~1200 m as the accretionary sediment section thickens, the BSR occurs at ~230 m below the seafloor, a 170 m upward migration in a lateral distance of ~12 km. Since some hydrates are already present near the deformation front, they will dissociate into free gas as the stability field phase boundary moves upward in the hydrate bearing sediment. The resultant free gas can migrate upward driven by advection and buoyancy and re-enter into the hydrate stability zone and reform hydrate. Some of the released methane gas might be retarded by "trapping" as bubbles beneath the new BSR, and free gas with concentration too low to readily migrate will become immobile below the BSR to form a low seismic velocity zone. For free-gas concentrations of only a few percent, gas permeability is at least three orders of magnitude less than the permeability of the formation water [*Honarpour et al.*, 1986]. Consequently, at low concentrations the gas will tend to move with the pore water rather than through it. Figure 6.1 schematically illustrates the hydrate formation mechanisms by both fluid expulsion and hydrate recycling due to stability field migration. The amount of hydrate formed in the accretionary sediments by the migration of the stability field can also be controlled by sedimentation and temperature changes. At least 50 to 100 m of the stability field migration due to tectonic uplift and sedimentation together with a ~70 m displacement caused by inter-glacial bottom-water warming, discussed in *Westbrook et al.* [1994] and *Whiticar et al.* [1995], indicates that an upward migration of the base of the stability field of

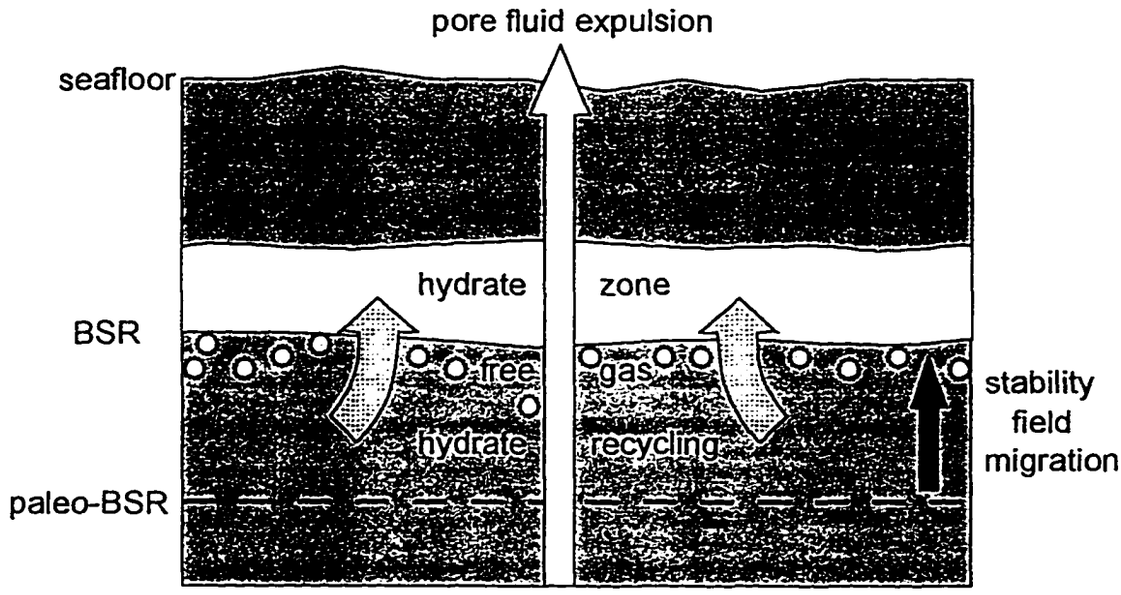

Figure 6.1 Schematic illustration for possible hydrate formation on the northern Cascadia convergent margin. Methane carried by upward fluid expulsion and dissociated hydrate re-entering into the stability field both contribute to the hydrate accumulation.

gas hydrate (and BSR) of >120 m probably has occurred over the past 10-15 Ma in the Cascadia margin.

The frontal region of the accretionary prism, where fluid expulsion reaches its maximum seaward of the deformation front, does not coincide with the areas where a strong BSR is developed over much of the lower-to-mid slope region. As discussed by *Hyndman and Davis* [1992], the fluid flow in the accretionary sediments plays an important role in carrying methane upward into the hydrate stability zone. The stability field migration and the hydrate recycling may consequently play an important, and possibly necessary, role in

sharpening the base of the hydrate layer to create a strong and continuous BSR over the rapid thickening sediment section in the slope region.

6.3 Significance of Reference Velocity Profile in Determining BSR Velocity Structure

In the lower slope region 15-20 km landward of the deformation front, where the thickness of the accretionary sediments is more than doubled compared to the incoming section in Cascadia Basin, a pronounced velocity decrease is evident from the seismic data. The velocities are much lower at any given depth than beneath the basin. This low velocity is explained by underconsolidation resulting from rapid horizontal shortening and vertical thickening of the sediment column. The shortening is accommodated by displacements along thrust faults or by distributed deformation. The thickening of the wedge results in sediment elements being moved to greater depths as they travel landward. There is little porosity loss and velocity change as the tectonic thickening occurs faster than the loading and pore fluid expulsion can reestablish a normal consolidation porosity-depth section. This low velocity was also supported by a numerical heat flow model in which the heat flow determined from the depth to the BSR was matched with a regional heat flow prediction considering sediment thickening and porosity variations in the lower slope region [*Hyndman et al.*, 1993a; *Wang et al.*, 1993].

A velocity versus depth function in the lower slope region, representing the no-hydrate/no-gas reference profile, has been established from the detailed semblance velocity analyses and the previously published ODP downhole log data at sites 889/890. This

reference profile is important in estimating concentrations of hydrate and gas above and below the BSR and in establishing an initial velocity model for the waveform inversion. The final model from the inversion is very dependent on the starting model, particularly the long-wavelength velocity features. The inversion requires that the starting model be as close as possible to a realistic model, and tests with alternative BSR velocity structures suggests that a reasonable hydrate model should include a velocity decrease at the BSR. Velocities above the BSR are independently constrained by the MCS data, ODP sonic logs, and VSP measurements. The velocities just below the seafloor and below the BSR has to be determined by the reference velocity profile. Based on this reference profile, the inversion results have shown that near ODP Sites 889/890 the velocity increase due to hydrate above the BSR accounts for ~2/3 of the impedance contrast required to produce the BSR reflection amplitudes. The remainder of the impedance contrast appears to come from the velocity decrease associated with the thin layer containing small concentrations, 1-2%, of free gas below the BSR.

6.4 Estimate of Gas Hydrate Distribution on Northern Cascadia Margin

The integrated analysis of the multichannel seismic and ODP downhole velocity data has allowed the velocity enhancement associated with the gas hydrate in the Cascadia accretionary prism sediments to be estimated. The increase in seismic velocity can be used to obtain a semiquantitative estimate of hydrate concentration. The simplest model is for the water in the sediment pore spaces to be partially replaced by evenly dispersed high-velocity gas hydrate "ice" that cements the sediment matrix. One approach discussed in Chapter 4

from the MCS velocities in the hydrate-enriched zone suggests that about 10-25% of the sediment pore space is occupied by hydrate (Figure 4.12).

The second approach assumes that the velocity anomaly above the BSR may be approximated by a simple reduction of porosity [*Hyndman and Spence*, 1992]. Hydrate forming in the sediment pore space effectively reduces the porosity by replacing pore fluids with high-velocity material. The amounts of hydrate required to produce the observed velocity increase can be estimated by simply calculating the difference in effective porosity between hydrate-bearing sediments and corresponding water-saturated sediments determined from the reference velocity-depth profile.

Results from ODP Legs 139 and 146 core plugs and downhole logging have suggested that the basin sediments, including those hydrothermally altered, do not show significant effects on the velocity-porosity relation from sediment cementation and diagenesis [*Davis and Fisher*, 1994; *Westbrook et al.*, 1994]. The assumption can thus be made that the velocity variation with depth primarily is due to porosity reduction. The velocity-porosity relation of *Hyndman et al.* [1993], which fits the measured drill core velocities and porosity well (Figure 2.11), is therefore used to calculate porosity reductions and to determine hydrate concentrations on three velocity-depth profiles in the region near and at ODP Site 889: (1) downhole logging sonic velocities, (2) VSP velocities, and (3) MCS velocity data (Figures 6.2a and 6.2b). The reference velocity-depth profile above 120 mbsf used for the calculation is that for the Cascadia Basin sediments and below 120 mbsf is that for the accretionary prism. The small-scale variability is probably a consequence of strongly layered grain size variations in these turbidite sediments, rather from variations in hydrate concentration. At Site 889,

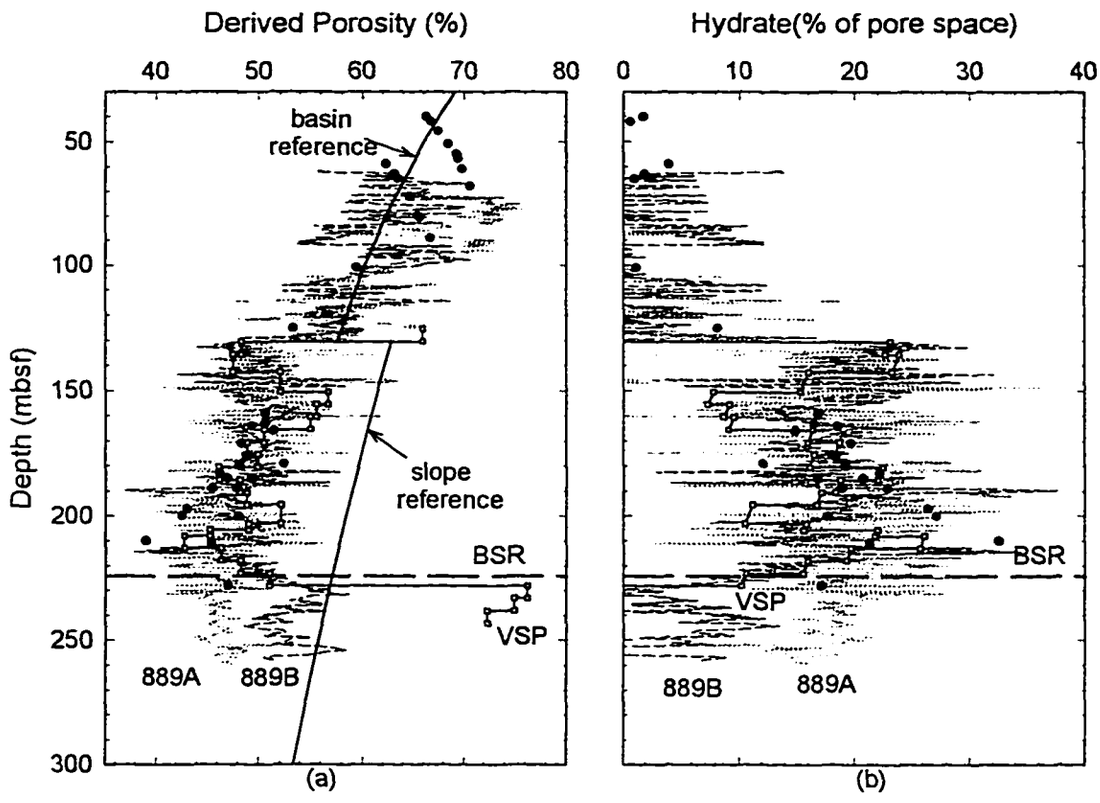

Figure 6.2 (a) Porosity-depth profile calculated from velocity data near and at ODP Site 889. Also shown in the figure is the change in porosity with depth for sediment containing no hydrate (from reference velocity function). (b) Hydrate concentration in the sediment pore space. The difference between the calculated porosity and reference porosity based on velocity is related to the amount of hydrate occupying pore space. Solid circles in the figures represent MCS velocities, light wiggle traces represent sonic logs, and open squares represent VSP velocities.

there is a general increase in the inferred amount of hydrate from near zero at the seafloor to an average of 20% of the pore space at the depth of BSR. The velocity of 3730 m/s for pure methane hydrate given by *Pearson et al.* [1983, 1986] is somewhat less than that of the sediment matrix (4300 to 5000 m/s), so the actual effect of porosity reduction by hydrate filling pore space may be less than that predicted by the velocity-porosity relation and the hydrate concentration lower. Alternatively, if the hydrate is preferentially concentrated at the

grain contacts rather than in main pores, its effect on velocity may be greater than that for simple porosity reduction.

The above two different velocity enhancement versus concentration models give hydrate concentration just above the BSR of 20-30% of pore space (10-15% of the sediment volume). This amount is in approximate agreement with the maximum of ~35% concentration in the pore space and the concentration profile with depth estimated from pore fluid chlorinity data of recovered cores at this site [*Yuan et al.*, 1996; *Desmons*, 1996; *Kastner et al.*, 1995]. On a seismic wavelength scale the velocity enhancement has a gradational top and increases smoothly with depth to the BSR, which explains why there is no seismic reflection from the top of the hydrate layer.

If the BSR is overlain by a 100 m zone of sediment with a mean porosity of 50% in which the hydrate saturation increases linearly from zero at the top of the zone to 20% at the BSR, the hydrate concentration-depth profiles in Figure 6.2b indicate a total hydrate of about 5 m^3/m^2 of ocean floor, or 820 m^3/m^2 of methane at STP. Throughout the Vancouver Island continental margin, where a clear BSR has been observed in an area of 30x200 km, the total methane gas estimated can amount to about 175 Tcf (trillion cubic feet) or 2.6 Gt of carbon. Hence, this methane presents a substantial amount of resource. This is a 100-year supply for Canada at the present rate of natural gas consumption.

BIBLIOGRAPHY

Aki, K., and Richards, P.G., 1980, Quantitative seismology: Theory and methods, W.H. Freeman and Co.

Al-Chalabi, M., 1974, An analysis of stacking, RMS, average, and interval velocities over a horizontal layered ground, Geophysical Prospecting, 22, 458-475.

Andreassen, K., P.E. Hart, and A. Grantz, 1995, Seismic studies of a bottom simulating reflection related to gas hydrate beneath the continental margin of the Beaufort Sea, Journal of Geophysical Research, 100, 12,659-12,673.

Appenzeller, T., 1991, Fire and ice under the deep-sea floor, Science, 252, 1790-1792.

Bangs, N.B., Westbrook, G.K., Ladd, J.W. and Buhl P., 1990, Seismic velocities from the Barbados ridge complex: indicators of high pore fluid pressures in an accretionary complex, Journal of Geophysical Research, 95, 8767-8782.

Biot, M.A., 1956a, Theory of propagation of elastic waves in a fluid-saturated porous solid. I. Low-frequency range, Journal of Acoustics Society of America, 28, 168-178.

Biot, M.A., 1956b, Theory of propagation of elastic waves in a fluid-saturated porous solid. II. Higher-frequency range, Journal of Acoustics Society of America, 28, 179-191.

Bortfeld, R., 1961, Approximation to the reflection and transmission coefficients of plane longitudinal and transverse waves, Geophysical Prospecting, 9, 485-503.

Bray, C.J. and Karig, D.E., 1985, Porosity of sediments in accretionary prisms and some implications for dewatering processes, Journal of Geophysical Research, 90, 768-778.

Carson, B., and Westbrook, G.K., 1995, Modern fluid flow in the Cascadia accretionary wedge: a synthesis, *in* Carson, B., Westbrook, G.K., Musgrave, R.J., and Suess, E., (Eds.), Proceedings of the Ocean Drilling Program, Scientific Results, 146 (Part 1), College Station, TX (Ocean Drilling Program), 413-421.

Carson, B., Westbrook, G.K., Musgrave, R.J., and Suess, E., (Eds.), 1995, Proceedings of the ODP, Scientific Results, 146 (Part 1), College Station, TX (Ocean Drilling Program).

Castagna, J.P., Batzle, M.L., and Eastwood, R.L., 1985, Relationships between compressional-wave and share-wave velocities in clastic silicate rocks, Geophysics, 50, 571-581.

Chapman, C.H., 1981, Generalised Radon transforms and slant stacks, Geophysical Journal of the Royal Astronomical Society, 66, 445-453.

Chiburis, E.F., 1984, Analysis of amplitude versus offset to detect gas/oil contacts in the Arabian Gulf, 54th Annual International Meeting, Society of Exploration Geophysics, Expanded Abstracts, 669-670.

Chiburis, E.F., 1993, AVO applications in Saudi Arabia, *in* Offset-dependent reflectivity - theory and practice of AVO analysis, Castagna, J.P., and Backus, M.M., Eds., Society of Exploration Geophysics, Investigations in Geophysics, Vol. 8.

Cochrane, G.R., Moore, J.C., MacKay, M.E. and Moore, G.F., 1994, Velocity and Inferred porosity model of the Oregon Accretionary Prism from multichannel seismic reflection data: implications on sediment dewatering and overpressure, Journal of Geophysical Research, 99, 7033-7043.

Coney, P.J., Jones, D.L., and Monger, J.W.H., 1980, Cordillera suspect terranes, Nature, 288, 329-333.

Clowes, R.M., Brandon, M.T., Green, A.G., Yorath, C.J., Sutherland Brown, A., Kanasewich, E.R., and Spencer, C., 1987a, LITHOPROBE - southern Vancouver Island: Cenozoic subduction complex imaged by deep seismic reflections, Canadian Journal of Earth Sciences, 24, 31-51.

Clowes, R.M., Yorath, C.J., and Hyndman, R.D., 1987b, Reflection mapping across the convergent margin of western Canada, Geophysical Journal of the Royal Astronomical Society, 89, 79-84.

Davis, D., Suppe, J., and Dahlem, F.A., 1983, Mechanics of fold-and-thrust belts and accretionary wedges, Journal of Geophysical Research, 88, 1153-1172.

Davis, E.E., Becker, K., Wang, K., and Carson, B., 1995, Long-term observations of pressure and temperature in Hole 892B, Cascadia accretionary prism, *in* Carson, B., Westbrook, G.K., Musgrave, R.J., and Suess, E., (Eds.), Proceedings of ODP Scientific Results, 146 (part 1). College Station, TX (Ocean Drilling Program), 299-311.

Davis, E.E., and Fisher, A.T., 1994, On the nature and consequences of hydrothermal circulation in the middle valley sedimented rift: Inferences from geophysical and geochemical observations, Leg 139, *in* Mottl, M.J., Davis, E.E., Fisher, A.T., and Slack, J.F. (Eds.), Proceedings of the Ocean Drilling Program, Scientific Results, 139, College Station, TX (Ocean Drilling Program), 695-717.

Davis, E.E., and Villinger, H., 1992, Tectonic and thermal structure of the middle valley sediment rift, northern Juan de Fuca Ridge, *in* Davis, E.E., Mottl, M.J., Fisher, A.T., et al., (Eds.), Proceedings of the ODP, Initial Reports, 139, College Station, TX (Ocean Drilling Program), 9-40.

Davis, E.E., et al., 1992, Site Reports, Site 858, *in* Proceedings of the ODP, Initial Reports, 139,

College Station, TX (Ocean Drilling Program), 431-543.

Davis, E.E., Hyndman, R.D., and Villinger, H., 1990, Rates of fluid expulsion across the northern Cascadia accretionary prism: constraints from new heat flow and multichannel seismic reflection data, Journal of Geophysical Research, 95, 8869-8889.

Davis, E.E., and Hyndman, R.D., 1989, Accretion and recent deformation of sediments along the northern Cascadia subduction zone, Geological Society of America Bulletin, 101, 1465-1480.

Davis, E.E., and Karsten, J.L., 1986, On the asymmetric distribution of seamounts about the Juan de Fuca ridge: Ridgecrest migration over a heterogeneous asthenosphere, Earth Planetary Science Letters, 79, 385-396.

Davis, E.E., and Riddihough, R.P., 1982, The Winona basin: Structure and tectonics, Canadian Journal of Earth Sciences, 19, 767-788.

Desmons, B., 1996, Integrated study of gas hydrates in marine sediments using geophysical and geochemical data, M.S. thesis, University of Victoria, Victoria, British Columbia.

Desmons, B., Hyndman, R.D., Spence, G.D., Whiticar, M.J., and Yuan, T., 1997, Integrated study of gas hydrates in marine sediments using geophysical and geochemical data, manuscript in preparation.

Dickens, G.R., and Quinby-Hunt, M.S., 1994, Methane hydrate stability in seawater, Geophysical Research Letters, 21, 2115-2118.

Dix, C.H., 1955, Seismic velocities from surface measurement, Geophysics, 20, 68-86.

Dillon, W.P., and C.K. Paull, 1983, Marine gas hydrates, II, Geophysical evidence, in *Natural Gas Hydrates: Properties, Occurrences and Recovery*, edited by J.L. Cox, pp. 73-90, Butterworth-Heinemann, Newton, Mass.

Dillon, W.P., Grow, J.A., and Paul, C.K., 1980, Unconventional gas hydrate seals may trap gas off southeast U.S., Oil and Gas Journal, 78, 124-126.

Domenico, S.N., 1977, Elastic properties of unconsolidated porous sand reservoirs, Geophysics, 42, 1339-1368.

Domenico, S.N., 1976, Effect of brine-gas mixture on velocity in an unconsolidated sand reservoir, Geophysics, 41, 882-894.

Dvorkin, J., G. Mavko, and Nur, A., 1991, The effect of cementation on the elastic properties of granular materia, Mechanics of Materials, 12, 207-217.

Ecker, C., Lumley, D., Dvorkin, J., Nur, A., 1996, Structure of hydrated sediment from seismic and rock physics, in *Proceedings of the 2nd International Conference on Natural Gas Hydrates*, Toulouse, France, 491-498.

Einsele, G.R., 1977, Velocity and material flux of compaction flow in growing sedimentary sequences, Sedimentology, 24, 639-655.

Ellis, R.M., et al., The Vancouver Island seismic project: a COCRUST onshore-offshore study of a convergent margin, Canadian Journal of Earth Sciences, 20, 719-741.

Englezos, P., and Bishnoi, P.R., 1988, Prediction of gas hydrate formation in aqueous solutions, American Institute of Chemical engineers, 34, 1718-1721.

Fowler, S.R., White, R.S. and Louden, K.E., 1985, Sediment dewatering in the Makran accretionary prism, Earth and Planetary Science Letters, 75, 427-438.

Gabrielse, H., and Yorath, C.J., (Editors). 1991, Geology of the Cordilleran Orogen in Canada, Geology Survey of Canada, Geology of Canada, No. 4 (also Geological Society of America, The Geology of North America, Vol. G-2).

Geertsma, J., 1961, Velocity-log interpretation: The effect of rock bulk compressibility, Society of Petroleum Engineering Journal, 1, 235-248.

Green, A.G., Clowes, R.M., Yorath, C.J., Spencer, C., Kanasewich, E.R., Brandon, M.T., and Sutherland Brown, A., 1986, Seismic reflection imaging of the subducting Juan de Fuca plate, Nature (London), 319, 210-213.

Gregory, A.R., 1976, Fluid saturation effects on dynamic elastic properties of sedimentary rocks, Geophysics, 41, 895-921.

Hajnal, Z., and Sereda, I.T., 1981, Maximum uncertainty of interval velocity estimates, Geophysics, 46, 1543-1547.

Hale, D., 1984, Dip-moveout by Fourier transform, Geophysics, 49, 741-757.

Han, D., Nur, A., and Morgan, D., 1986, Effects of porosity and clay content on wave velocities in sandstone, Geophysics, 51, 2093-2107.

Hamilton, E.L., 1979, V_p/V_s and Poisson's ratios in marine sediments and rocks, Journal of Acoustics Society of America, 66, 1093-1101.

Hannay, D.E., 1995, Analysis of geoacoustic shot run data from the Pacific Shelf experiment, DREP Contractor Report, JASCO Research Ltd., Sidney, B.C., Canada.

Honarpour, M., Koederitz, L., and Harvey, A.H., 1986, Relative permeability of petroleum reservoirs: Boca Raton, Florida, CRC Press, 143p.

Hyndman, R.D., 1995, The Lithoprobe corridor across the Vancouver Island continental margin: the structural and tectonic consequences of subduction, Canadian Journal of Earth Sciences, 32, 1777-1802,

Hyndman, R.D., Spence, G.D., Yuan, T., and Davis, E.E., 1994, Regional geophysical and structure

framework of the Vancouver Island margin accretionary prism, *in* Westbrook, G.K., Carson, B., Musgrave, R.J., et al., (Eds.), Proceedings of the ODP, Initial Reports, 146 (Part 1), College Station, TX (Ocean Drilling Program), 399-419.

Hyndman, R.D., Wang, K., Yuan, T., 1993a, Tectonic sediment thickening, fluid expulsion, and the thermal regime of subduction zone accretionary prisms: The Cascadia margin off Vancouver Island, Journal of Geophysical Research, 98, 21,865-21,876.

Hyndman, R.D., Moore, G.F. and Moran, K., 1993b, Velocity, porosity and pore-fluid loss from the Nankai subduction zone accretionary prism, edited by Hill, I.A., Taira, A., Firth, J.V., et al., Proceedings of the Ocean Drilling Program Scientific Results, Vol. 131, College Station, TX (Ocean Drilling Program), 211-220.

Hyndman, R.D., and E.E. Davis, 1992, A mechanism for the formation of methane hydrate and seafloor bottom simulation reflectors by vertical fluid expulsion, Journal of Geophysical Research, 97, 7025-7041.

Hyndman, R.D., and G.D. Spence, 1992, A seismic study of methane hydrate marine bottom simulating reflectors, Journal of Geophysical Research, 97, 6683-6698.

Hyndman, R.D., Yorath, C.J., Clowes, R.M., and Davis, E.E., 1990, The northern Cascadia subduction zone at Vancouver Island: seismic structure and tectonic history, Canadian Journal of Earth Sciences, 27, 313-329.

Hyndman R.D., 1988, Dipping reflectors, electrically conductive zones and free water beneath a subduction zone, Journal of Geophysical Research, 93, 13,391-13,405.

Hyndman, R.D., Riddihough, R.P., and Herzer, R., 1979, The Nootka fault zone - A new plate boundary off western Canada, Royal Astronomical Society Geophysical Journal, 58, 667-683.

Jarrard, R.D., M.E. MacKay, G.K. Westbrook, and E.J. Screaton, 1995, Log-based porosity of ODP Sites on the Cascadia accretionary prism, *in* Carson, B., Westbrook, G.K., Musgrave, R.J., and Suess, E., (Eds.), Proceedings of the ODP Scientific Results, 146 (Part 1), College Station, TX (Ocean Drilling Program), 313-335.

Jarrard, R.D., Dadey, K.A., and Busch, W.H., 1989, Velocity and density of sediments of Eirik Ridge, Labrador Sea: control by porosity and mineralogy, *in* Srivastava, S.P., Arthur, M.A., Clement, B., et al. (Eds.), Proceedings of Ocean Drilling Program Scientific Results, 105, College station, TX (Ocean Drilling Program), 811-835.

Johnson, S.Y., 1984, Evidence for a margin truncating transcurrent fault (pre-late Eocene) in western Washington, Geology, 12, 538-541.

Kastner, M., Kvenvolden, K.A., Whiticar, M.J., Camerlenghi, A., and Lorenson, T.D., 1995, Relation between pore fluid chemistry and gas hydrates associated with bottom-simulating reflectors at the Cascadia margin, Sites 889 and 892, *in* Carson, B., Westbrook, G.K., Musgrave, R.J., and Suess, E., (Eds.), Proceedings of the Ocean Drilling Program, Scientific Results, 146 (Part 1), College Station, TX (Ocean Drilling Program), 175-187.

Katzman, R., W.S. Holbrook, and C.K. Paull, 1994, A combined vertical-incidence and wide-angle seismic study of a gas hydrate zone, Blake Ridge, Journal of Geophysical Research, 99, 17,975-17,995.

Kennett, B.L.N., and Kerry, N.J., 1979, Seismic waves in a stratified half-space, Geophysical Journal of the Royal Astronomical Society, 57, 557-583.

Korenaga, J., Holbrook, W.S., Singh, S.C., and Minshull, T.A., 1996, Natural gas hydrates on the southeast US margin: Constraints from full waveform and traveltime inversions of wide-angle

seismic data, submitted to Journal of Geophysical Research.

Kurtz, R.D., Delaurier, J.M., and Gupta, J.C., 1986, A magnetotelluric sounding across Vancouver Island detects the subducting Juan de Fuca plate, Nature (London), 321, 596-599.

Kvenvolden, K.A., 1993, Gas hydrates - Geological perspective and global change, Review of Geophysics, 31, 173-187.

Kvenvolden, K.A., 1988a, Methane hydrate - A major reservoir of carbon in the shallow geosphere? Chemical Geology, 71, 41-51.

Kvenvolden, K.A., 1988b, Methane hydrate and global climate, Global Biogeochemical Cycles, 2, 221-229.

Kvenvolden, K.A., and T.J. McDonald, 1985, Gas hydrate of the Middle America trench - DSDP Leg 84, edited by R. von Huene, et al., in *Initial Reports Deep Sea Drilling Project, 84*, 667-682.

Kvenvolden, K.A., and Barnard, L.A., 1983, Hydrates of natural gas in continental margins, in *Studies in Continental Margin Geology*, edited by Walkins, J.S., and Drake, C.L., Memoir of American Association of Petroleum Geologists, 34, 631-640.

Langton, S., 1995, The seismic structure of the Tofino Basin and underlying accreted terranes, M.S. thesis, University of Victoria, Victoria, British Columbia.

Lee, M.W., D.R. Hutchinson, W.F. Agena, W.P. Dillon, J.J. Miller, and B.A. Swift, 1994, Seismic character of gas hydrates on the southeastern U.S. continental margin, Marine Geophysical Research, 16, 163-184.

Lee, M.W., D.R. Hutchinson, W.P. Dillon, J.J. Miller, W.F. Agena, and B.A. Swift, 1993, Method of estimating the amount of in situ gas hydrate in deep marine sediments, Marine Petroleum Geology, 10, 493-506.

Le Pichon, X., Foucher, J.P., Boulegue, J., Henry, P., Lallemant, S., et al., 1990, Mud volcano field seaward of the Barbados accretionary complex: a submersible study, Journal of Geophysical Research, 95, 8931-8945.

Lewis, B.T.R., 1992, Changes in P and S velocities caused by subduction related sediment accretion off Washington/Oregon, in *Shear Wave in Marine Sediments*, edited by J. Koven and R. Stoll, Kluwer Academic, pp. 379-386, Kluwer Academic, Norwell Mass.

Lewis, T.J., Bentkowski, W.H., Davis, E.E., Hyndman, R.D., Souther, J.G., and Wright, J.A., 1988, Subduction of the Juan de Fuca plate: thermal consequences, Journal of Geophysical Research, 93, 15,207-15,225.

Liner, C., 1990, General theory and comparative anatomy of dip moveout, Geophysics, 55, 595-607.

MacKay, M.E., R.D. Jarrard, G.K. Westbrook, R.D. Hyndman, 1994, and the Shipboard Scientific Party of ODP Leg 146, Origin of bottom simulating reflectors: Geophysical evidence from the Cascadia accretionary prism, Geology, 22, 459-462.

MacDonald, G.T., 1990a, The future of methane as an energy resource, Annual Reviews of Energy, 15, 53-83.

MacDonald, G.T., 1990b, The role of methane clathrates in past and future climates, Climate Change, 16, 247-281.

Massey, N.W.D., 1986, The Metchosin Igneous Complex, southern Vancouver Island: ophiolite stratigraphy developed in an emergent island setting, Geology, 14, 602-605.

Mathews, M.A., and von Huene, R., 1985, Site 570 methane hydrate zone, edited by von Huene, R., Aubouin, J., et al., *in* Initial Reports Deep Sea Drilling Project, 84, 773-790.

Matsumoto, R, 1996, Highlights of ODP Leg 164: Gas hydrate drilling, *in* Gas Hydrate Studies,

Proceedings of the Canada-Japan Joint Science and Technology Workshop, Victoria, BC, Canada.

Metropolis, N., Rosenbluth, M.N., Rosenbluth, A.W., Teller, A.H., and Teller, E., 1953, Equation of state calculation by fact computing, Journal of Chemical Physics, 1, 1087-1092.

Mclver, R.D., 1974, Hydrocarbon gas (methane) in canned Deep Sea Drilling Project core samples, in *Natural Gases in Marine Sediments*, edited by Kaplan, I.R., 63-69, Plenum, New York.

Miller, J.J., M.W. Lee, and R. von Huene, 1991, An analysis of a seismic reflection from the base of a gas hydrate zone, offshore Peru, American Association of Petroleum Geologists Bulletin, 75, 910-924.

Minshull, T.A., S.C. Singh, and G.K. Westbrook, 1994, Seismic velocity structure at a gas hydrate reflector, offshore western Colombia, from full waveform inversion, Journal of Geophysical Research, 99, 4715-4734.

Minshull, T. and White, R., 1989, Sediment compaction and fluid migration in the Makran accretionary prism, Journal of Geophysical Research, 94, 7387-7402.

Moore, J.C. and Vrolijk, P., 1992, Fluids in accretionary prisms, Reviews of Geophysics, 30, 113-135.

Moore, J.C., et al., 1988, Tectonics and hydrology of the Northern Barbados Ridge: results of Leg 110 ODP, Geological Association of America Bulletin, 100, 1578-1593.

Murphy, W.F., 1984, Acoustic measures of partial gas saturation in tight sandstones, Journal of Geophysical Research, 89, 11,549-11,559.

Nelder, J.A., and Mead, R., 1965, A simplex method for function minimization, Computer Journal, 7, 308-313.

Nisbet, E.G., 1990, The end of ice age, Canadian Journal of Earth Sciences, 27, 148-157.

Ostrander, W.J., 1984, Plan-wave reflection coefficients for gas sends at non-normal angel of incidence, Geophysics, 49, 1637-1648.

Pandit, B.I., and King, M.S., 1983, Elastic wave velocities of propane gas hydrates, in *Natural Gas Hydrate: Properties, Occurrence and Recovery,* edited by Cox, J.L., pp 49-61, Butterworth, Stoneham, M.A.

Paull, C.K., Ussler, W., and Borowski, W.S., 1994, Sources of biogenic methane to form marine gas hydrates: In situ production or upward migration? New York Academy of Science Annals, 715, 392-409.

Pearson, C.F., J. Murphy, and R. Hermes, 1986, Acoustic and resistivity measurements on rock samples containing hydrates: Laboratory analogues to natural gas hydrate deposits, Journal of Geophysical Research, 91, 14,132-14,138.

Pearson, C.F., P.M. Halleck, P.L. McGuire, R. Hermes, and M. Mathews, Natural gas hydrate: A review of in situ properties, Journal of Physical Chemistry, 87, 4180-4185, 1983.

Riddihough, R.P., 1985, Magnetic anomalies, Juan de Fuca plate map series, Department of Energy, Mines and Resources, Canada, Earth Physics Branch Open File Report 85-20, Map JFP11.

Riddihough, R.P., 1984, Recent movements of the Juan de Fuca plate system, Journal of Geophysical Research, 89, 6980-6994.

Rogers, G.C., 1985, seismicity beneath the LITHOPROBE corridor, Geological Association of Canada, Pacific Section, Symposium, April 19, 1985, Victoria, B.C., Program with abstract, p. 28.

Rohr, K.M.M., and Furlong, K.P., 1995, Ephemeral plate tectonics at the Queen Charlotte tripe

junction, Geology, 23, 1035-1038.

Rutherfold, S.R., and Williams, R.H., 1989, Amplitude-versus-offset variations in gas sand, Geophysics, 54, 680-688.

Shi, Y.L. and Wang, C.Y., 1988, Generation of high pore pressures in accretionary prisms: inferences from the Barbados subduction complex, Journal of Geophysical Research, 93, 8893-8910.

Sheriff, R.E., and Geldart, L.P., 1982, Exploration Seismology Vol. 1, History, theory, and data acquisition, Cambridge University Press, New York.

Shipley, T.H., and B.M. Didyk, 1981, Occurrences of methane hydrate offshore southern Mexico, *in* Initial Reports, Deep Sea Drilling Project, 66, 547-555.

Shipley, T.H., M.H. Huston, R.T. Buffler, F.J. Shaub, K.J. McMillen, J.W. Ladd, and J.L. Worzel, 1979, Seismic evidence for wide spread possible gas hydrate horizons on continental slopes and rises, American Association of Petroleum Geologists Bulletin, 63, 2204-2213.

Shouldice, D. H., 1971, Geology of the western Canadian continental shelf, Bulletin of Canadian Petroleum Geology, 19, 405-436.

Shuey, R.T., 1985, A simplification of the Zoeppritz equations, Geophysics, 50, 609-614.

Singh, S.C., and T.A. Minshull, 1994, Velocity structure of a gas hydrate reflector at Ocean Drilling Program site 889 from global seismic waveform inversion, Journal of Geophysical Research, 99, 24,221-24,233.

Singh, S.C., T.A. Minshull, and G.D. Spence, 1993, Velocity structure of a gas hydrate reflector, Science, 260, 204-207.

Singh, S.C., Dietrich, M., and Chapel, F., 1991, A complete waveform inversion and its application to ECORS data, in *Continental Lithosphere: Deep Seismic Reflections*, edited by R.

Meissner, et al., Geodynamics Series volume 22, pp. 391-400, AGU, Washington, D.C..

Sloan, E.D., 1990, Clathrate hydrates of natural gases, 641 pp., Marcel Dekker, New York.

Spence, G.D., Minshull, T.A., and Fink, C., 1995, Seismic structure of methane gas hydrate, offshore Vancouver Island, *in* Carson, B., Westbrook, G.K., Musgrave, R.J., and Suess, E., (Eds.), Proceedings of the Ocean Drilling Program, Scientific Results, 146 (Part 1), College Station, TX (Ocean Drilling Program), 163-174.

Spence, G.D., Hyndman, R.D., Davis, E.E., and Yorath, C.J., 1991a, Multichannel reflection profiles across the Vancouver Island continental shelf and slope, Geological Survey of Canada, Open File No. 2391.

Spence, G.D., Hyndman, R.D., Davis, E.E., and Yorath, C.J., 1991b, Seismic structure of the northern Cascadia accretionary prism: Evidence from new multichannel seismic reflection data, in *Continental Lithosphere, Deep Seismic Reflections*, edited by R. Meissner, et al., Geodynamics Series volume 22, pp. 257-263, American Geophysical Union, Washington, D.C..

Spence, G.D., Clowes, R.M., and Ellis, R.M., 1985, Seismic structure across the active subduction zone of western Canada, Journal of Geophysical Research, 90, 6754-6772.

Stoffa, P.L., Diebold, J.B. and Buhl, P., 1982, Velocity analysis for wide aperture seismic data, Geophysical Prospecting, 30, 25-57.

Stoll, R.D., 1974, Effects of gas hydrates in sediments, in *Natural Gases in Marine Sediments*, edited by Kaplan, I.R., 235-248, Plenum, New York.

Stoll, R.D., Ewing, J., and Bryan, G.M., 1971, Anomalous wave velocities in sediments containing gas hydrates, Journal of Geophysical Research, 76, 2090-2094.

Sutherland Brown, A., and Yorath, C.J., 1985, Lithoprobe profile across southern Vancouver Island: geology and tectonics, trip 8, in *Field guides to geology and mineral deposits in the southern Canadian Cordillera*, Geological Society of America, Cordilleran Section meeting, Vancouver, Vol. 8, pp. 1-23.

von Huene, R. and Lee, H., 1982, The possible significance of pore fluid pressure in subduction zone, American Association of Petroleum Geologists Memoir No.34, 201-242.

Waldron, D.A., Clowes, R.M. and White, D.J., 1990, Seismic structure of a subducting oceanic plate off western Canada, in *Studies of Laterally Heterogeneous Structures Using Seismic Refraction and Reflection Data*, edited by A.G. Green, Geological Survey of Canada, Paper 89-13, 105-113.

Waldron, D.A., 1982, Structure characteristics of a subducting oceanic plate, M.S. thesis, 121 pp., University of British Columbia, Vancouver.

Wang, K., 1994, Kinematic models of dewatering accretionary prisms, Journal of Geophysical Research, 99, 4429-4438.

Wang, K., Hyndman, R.D., and Davis, E.E., 1993, Thermal effects of sediment thickening and fluid expulsion in accretionary prisms: model and parameter analysis, Journal of Geophysical Research, 98, 9975-9984.

Wang, X, and Clowes, R.M., 1995, Seismic structure across the Cascadia subduction zone off Vancouver Island: New evidence from seismic refraction and wide-angle reflection data, in *Final program and Abstract*, Geological Association of Canada/Mineralogical Association of Canada annual meeting, Victoria, British Columbia, A109.

Watson, R.T., Rodher, H., Oeschger, H., and Siegenthaler, U., 1990, Greenhouse gases and aerosols,

in *Climate change, The IPCC Scientific Assessment*, Houghton, J.T., Jenkins, G.J., and Ephraums, J.J., eds, Cambridge University Press, new York, 1-40.

Wells, R.E., Engebretson, D.C., Snavely, P.D., Jr., and Coe, R.S., 1984, Cenozoic plate motions and the volcano-tectonic evolution of western Oregon and Washington, Tectonics, 3, 275-294.

Westbrook, G.K., Carson, B., Musgrave., R.J., et al., (Eds.) 1994, Proceedings of the ODP, Initial Reports, 146 (part 1), College Station, TX (Ocean Drilling Program).

Westbrook, G. K., 1991, Geophysical evidence for the role of fluids in accretionary wedge tectonics, Philos. Trans. R. Soc. London Series, A335, 228-242.

Whalley, E., 1980, Speed of longitudinal sound in clathrate hydrates, Journal of Geophysical Research, 85, 2539-2542.

Whiticar, M.J. and Hovland, M., 1995, Data report: molecular and stable isotope analyses of sorbed and free hydrocarbon gases of Leg 146, Cascadia and Oregon margins, *in* Carson, B., Westbrook, G.K., Musgrave, R.J., and Suess, E., (Eds.), Proceedings of the Ocean Drilling Program, Scientific Results, 146 (Part 1), College Station, TX (Ocean Drilling Program), 439-449.

Whiticar, M.J., Hovland, M., Kastner, M., and Sample, J.C., 1995, Organic geochemistry of gases, fluids, and hydrates at the Cascadia accretionary margin, *in* Carson, B., Westbrook, G.K., Musgrave, R.J., and Suess, E., (Eds.), Proceedings of the Ocean Drilling Program, Scientific Results, 146 (Part 1), College Station, TX (Ocean Drilling Program), 385-397.

Whiticar, M.J., 1990, A geochemical perspective of natural gas and atmospheric methane, Organic Geochemistry, 16, 531-547.

Wood, W.T., P.L. Stoffa, and T.H. Shipley, 1994, Quantitative detection of methane hydrate through

high-resolution seismic velocity analysis, Journal of Geophysical Research, 99, 9681-9695.

Wyllie, M.R.J., A.R. Gregory, and G.H.F. Gardner, 1958, An experimental investigation of factors affecting elastic wave velocities in porous media, Geophysics, 23, 459-493.

Yamano, M., Foucher, J.P., Kinoshita, M., Fisher, A., Hyndman, R.D., 1992, ODP Leg 131 Shipboard Scientific Party, Heat flow and fluid flow regime in the western Nankai accretionary prism, Earth and Planetary Sciences Letters, 109, 451-462.

Yefremova, A.G., and Zhizhchenko, B.P., 1975, Occurrence of crystal hydrates in sediments of modern marine basins, Dokl. Acad. Sci. U.S.S.R., Earth Sci. Sect., 214, 219-220.

Yilmaz, O., 1987, Seismic Data Processing, Society of Exploration Geophysics, Investigations in Geophysics, vol. 2.

Yorath, C.J., Brown, A.S., Campbell, R.B., and Dodds, C.J., 1995, Upper Jurassic to palaeogene assemblages: the Insular Belt, *in* Geology of the cordilleran Orogen in Canada (Gabrielse, H , editor, et al.), *in* the collection Geology of North America, Geological survey of Canada, p.354-360.

Yorath, C.J, Clowes, R.M., Green, A.G., Sutherland Brown, A., Brandon, M.T., Massey, N.W.D., Spencer, C., Kanasewich, E.R., and Hyndman, R.D., 1985a, LITHOPROBE, Phase I: southern Vancouver Island: preliminary analysis of reflection seismic profiles and surface geological studies, in *Current Research*, part A, Geological Survey of Canada, Paper 85-1A, pp. 543-554.

Yorath, C.J., Green, A.G., Clowes, R.M., Sutherland Brown, A., Brandon, M.T., Kanasewich, E.R , Hyndman, R.D., and Spencer, C., 1985b, LITHOPROBE, southern Vancouver Island: seismic reflection sees through Wrangellia to the Juan de Fuca plate, Geology, 13, 759-762.

Yorath, C.J., Clowes, R.M., MacDonald, R.D., Spencer, C., Davis, E.E., Hyndman, R.D., Rohr, K., Sweeney, J.F., Currie, R.G., Halpenny, J.F., and Seemann, D.A., 1987, marine multichannel seismic reflection, gravity and magnetic profiles - Vancouver Island continental margin and Juan de Fuca Ridge, Geological Survey of Canada, Open File 1661.

Yuan, T., Hyndman, R.D., Spence, G.D., and Desmons, B., 1996, Seismic velocity increase and deep-sea gas hydrate concentration above a bottom-simulating reflector on the northern Cascadia continental slope, Journal of Geophysical Research, 101, 13,655-13,671.

Yuan, T., Spence, G.D., Hyndman, R.D., 1994, Seismic velocities and inferred porosities in the accretionary wedge sediments at the Cascadia margin, Journal of Geophysical Research, 99, 4413-4427.